

# **DISSERTATION**

for obtaining the doctoral degree of the  
Combined Faculty of Mathematics, Engineering and Natural  
Sciences

of the

Ruprecht-Karls-University of Heidelberg

Presented by

**Dipl- Ing. M.Sc. Janathan Michael Juarez Altuzar**

Born in Tijuana, Baja California, Mexico

Oral examination:

25<sup>th</sup> May 2022

**Development, characterization and application  
of lysosome-targeted multi-functional  
sphingosine and cholesterol probes**

Referees:

Prof. Dr. Britta Brügger

Dr. Doris Höglinger

This work was carried under supervision of Dr. Doris Höglinger at the Biochemistry Centre of Heidelberg University (BZH) from October 2017 to March 2022 and parts of this work are described in the following pre-print: **doi: <https://doi.org/10.1101/2021.11.10.468010>**. Therefore, any title, text, figure and reference that shares similarities with the presented work, are originating from the same author.

# Abstract

---

Lysosomes are membrane-bound organelles that act as a central hub for the recycling of biomolecules derived from cellular processes such as autophagy, endocytosis, among others. Lysosomal dysfunction is often linked to severe pathologies such as lysosomal storage disorders (LSDs), which are characterized by the aberrant accumulation of substrates, such as lipids. While cholesterol efflux from lysosomes is well-understood, the transport of other biologically active lipids such as sphingosine remain unknown. This knowledge gap is attributed to a lack of functional tools to manipulate and investigate lipids within living cells and on a single organelle level. The recent development of organelle-targeted caging groups, photoaffinity labeling and in combination with biorthogonal reactions represents a valuable and non-invasive way to identify new protein interactors of single lipid species while acquiring an exquisite spatial-temporal control.

This work presents the development, characterization and application of a method to investigate the previously enigmatic export of sphingosine from lysosomes. To this end, We have synthesized **lysosome-targeted photoactivatable sphingosine** (Lyso-pacSph) and **lysosome-targeted photoactivatable cholesterol** (Lyso-pacChol) that combine existing technologies such as photoaffinity labeling and a lysosome-targeted photoremovable caging group. In this way, the lyso-probes allow their controlled release within the lysosome using a flash of light. Their remaining modifications enable the study of their trafficking and metabolism as well as the capture of their unique lysosomal interactome. Excitingly, known cholesterol transporters, such as the abundant lysosomal protein SCARB2/LIMP-2 and Niemann-Pick type C1 (NPC1) were also identified as sphingosine interactors. Additionally, I show that both proteins play similar roles in sphingosine transport from lysosomes. Absence of either protein resulted in delayed sphingosine metabolism as observed by thin-layer chromatography as well as prolonged lysosomal localization of the sphingosine probe as shown in fluorescence microscopy experiments. The latter method also allowed me

to analyze the impact of an approved drug for NPC, miglustat, on subcellular sphingosine and cholesterol trafficking. Additionally, artificial elevation of sphingosine levels in WT cells created a cholesterol export defect reminiscent of NPC disease, pointing towards a direct and causative role of sphingosine in the pathobiochemistry of this disease. Overall, the developed method presents a powerful tool to investigate the actions of biologically active lipid species with subcellular precision. This will likely inspire the generation of similar tools targeting different lipids and other organelles, thus contributing to a more detailed understanding of the intricacies of lipid-mediated signaling events.

# Zusammenfassung

---

Lysosomen sind membrangebundene Organellen, die als zentraler Punkt für das Recycling von Biomolekülen fungieren, die bei zellulären Prozessen wie Autophagie, Endozytose, unter anderem. Eine lysosomale Dysfunktion ist häufig mit schwerwiegenden Pathologien wie lysosomalen Speicherkrankheiten (LSD) verbunden, die durch eine abnorme Anhäufung von Substraten, wie z. B. Lipiden, gekennzeichnet sind. Während der Cholesterin-Efflux aus Lysosomen gut verstanden ist, ist der Transport anderer biologisch aktiver Lipide wie Sphingosin noch unbekannt. Diese Wissenslücke ist auf einen Mangel an funktionellen Werkzeugen zur Manipulation und Untersuchung von Lipiden in lebenden Zellen und auf der Ebene einzelner Organellen zurückzuführen. Die aktuelle Entwicklung von Organelle-targeted Caging-Gruppen, Photoaffinitäts-Markierung und in Kombination mit biorthogonalen Reaktionen stellt einen wertvollen und nicht-invasiven Weg dar, um neue Protein-Interaktoren einzelner Lipidspezies zu identifizieren und gleichzeitig eine präzise räumlich-zeitliche Kontrolle zu erlangen.

Diese Arbeit stellt die Entwicklung, Charakterisierung und Anwendung einer Methode zur Untersuchung des bisher rätselhaften Exports von Sphingosin aus Lysosomen vor. Zu diesem Zweck haben wir lysosomenzielgerichtetes, photoaktivierbares Sphingosin (Lyso-pacSph) und lysosomenzielgerichtetes, photoaktivierbares Cholesterin (Lyso-pacChol) synthetisiert, die bestehenden Technologien wie die Photoaffinitätsmarkierung und eine lysosomenzielgerichtetes, photoremovable Caging-Gruppe kombinieren. Auf diese Weise ermöglichen die Lyso-Sonden ihre kontrollierte Freisetzung innerhalb des Lysosoms durch einen Lichtblitz. Die verbleibenden Modifikationen ermöglichen die Untersuchung ihres Transportes und Stoffwechsels sowie die Erfassung ihres einzigartigen lysosomalen Interaktoms. Spannenderweise wurden bekannte Cholesterintransporter wie das reichlich vorhandene lysosomale Protein SCARB2/LIMP-2 und Niemann-Pick Typ C1 (NPC1) ebenfalls als Sphingosin-Interaktoren identifiziert. Darüber hinaus konnte ich zeigen,

dass beide Proteine eine ähnliche Rolle beim Sphingosintransport aus den Lysosomen spielen. Das Fehlen eines der beiden Proteine führte zu einem verzögerten Sphingosin-Stoffwechsel, wie durch Dünnschichtchromatographie beobachtet wurde, sowie zu einer verlängerten lysosomalen Lokalisierung der Sphingosin-Sonde, wie in Fluoreszenzmikroskopie-Experimenten gezeigt wurde. Mit der letztgenannten Methode konnte ich auch die Auswirkungen eines für NPC zugelassenen Medikaments, Miglustat, auf den subzellulären Sphingosin- und Cholesterinverkehr analysieren. Darüber hinaus führte die künstliche Erhöhung des Sphingosinspiegels in WT-Zellen zu einem Cholesterinexportdefekt, der an die NPC-Krankheit erinnert, was auf eine direkte und ursächliche Rolle von Sphingosin in der Pathobiochemie dieser Krankheit hindeutet. Insgesamt stellt die entwickelte Methode ein leistungsfähiges Instrument dar, um die Wirkung biologisch aktiver Lipidspezies mit subzellulärer Präzision zu untersuchen. Dies wird wahrscheinlich die Entwicklung ähnlicher Instrumente für andere Lipide und andere Organellen anregen und so zu einem genaueren Verständnis der Feinheiten der durch Lipide vermittelten Signalvorgänge beitragen.

# Table of contents

---

<b>ABSTRACT</b> .....	<b>I</b>
<b>ZUSAMMENFASSUNG</b> .....	<b>III</b>
<b>TABLE OF CONTENTS</b> .....	<b>V</b>
<b>LIST OF FIGURES</b> .....	<b>VII</b>
<b>CHAPTER 1 – INTRODUCTION</b> .....	<b>1</b>
1.1. CELLULAR LIPID DIVERSITY .....	1
1.2 LIPID BREAKDOWN OCCURS IN LYSOSOMES .....	4
1.3 SUBCELLULAR TRANSPORT OF LIPIDS .....	6
1.3.1 <i>Lysosomal efflux of (sphingo)-lipids</i> .....	7
1.4 CHEMICAL BIOLOGY TOOLS TO STUDY (SPHINGO)-LIPID BIOLOGY .....	11
1.4.1 <i>Radiolabeled lipids</i> .....	11
1.4.2 <i>Fluorescent lipids</i> .....	12
1.4.3 <i>Bioorthogonal chemistry: Probing for targets with chemically modified biomolecules</i> .....	13
1.4.3.1 <i>Click chemistry</i> .....	13
1.4.3.2 <i>Photoaffinity labeling</i> .....	14
1.4.3.3 <i>Caged, bi-, tri-functional and organelle-targeted lipids: release of lipids with spatial-temporal resolution</i> .....	15
<b>OBJECTIVES OF THIS THESIS</b> .....	<b>21</b>
<b>CHAPTER 2 – RESULTS AND DISCUSSION</b> .....	<b>23</b>
2.1. TARGETING CHOLESTEROL AND SPHINGOSINE TO LYSOSOMES – A NEW APPROACH FOR STUDYING THEIR SUBCELLULAR ACTIONS .....	23
2.1.1 <i>Targeting the lysosome with a coumarin-cage approach</i> .....	23
2.1.2 <i>Synthesis and characterization of a lysosome-targeted sphingosine via an epoxysuccinic group</i> .....	24
2.1.3 <i>Synthesis via a tertiary amine-modified coumarin cage</i> .....	27
2.1.4 <i>Troubleshooting and synthesis of lysosome-targeted sphingosine, cholesterol, pacSph and pacChol</i> .....	28
2.2 CHARACTERIZATION OF LYSO-PACSPH AND LYSO-PACCHOL .....	31
2.3 LYSOSOME-TARGETED SPHINGOSINE AND CHOLESTEROL ARE NOVEL TOOLS TO STUDY LIPID TRANSPORT AND METABOLISM IN CELLULAR DISEASE MODELS.....	37
2.3.1 <i>Miglustat as a drug for the treatment of Niemann-Pick Type C1</i> .....	44
2.4 DESIGN, OUTCOME AND BIOCHEMICAL VALIDATION OF CHEMOPROTEOMIC PROFILING OF LYSO-PACSPH AND LYSO-PACCHOL .....	48

2.4.1 Metabolism and subcellular localization of Sph and Chol in NPC1 and LIMP2 null cells.....	51
2.4.2 Lysosomal impaired efflux of sphingosine is a direct effect of NPC1 disfunction.....	56
2.4.3 Conclusion and outlook.....	62
<b>CHAPTER 3 – EXPERIMENTAL METHODS.....</b>	<b>65</b>
3.1 REAGENTS.....	65
3.2 CHEMICAL SYNTHESIS .....	65
3.2.1 General synthetic procedures .....	65
3.3 BUFFERS AND SOLUTIONS .....	74
3.4 CELL CULTURE .....	75
3.5 LIPID ANALYSES BY THIN-LAYER CHROMATOGRAPHY.....	76
3.5.1 TLC analysis of Lyso-pacSph .....	76
3.5.2 TLC analysis of Lyso-pacChol .....	77
3.6 CONFOCAL MICROSCOPY .....	78
3.6.1 Live cell microscopy of lysosome-targeted compounds.....	78
3.6.2 Visualisation of time-resolved subcellular localisation of lysosome-targeted compounds .....	79
3.6.2.1 Visualization of Lyso-pacSph .....	79
3.6.2.2 Visualization of Lyso-pacChol .....	80
3.6.2.3 Immunofluorescence of fixed cells .....	80
3.6.3 Starvation assay .....	81
3.6.4 NPC1-like induced assay.....	81
3.7 STREPTAVIDIN PULL DOWN ASSAY.....	82
3.7.1 Cell Labelling and Crosslinking.....	82
3.7.2 Protein determination using Amido Black .....	83
3.7.3 Biotinylation and protein precipitation .....	84
3.7.4 Streptavidin Pull Down.....	84
3.7.5 SDS PAGE and Western Blot analysis off pull-down probes.....	85
3.8 DATA PROCESSING .....	85
<b>REFERENCES.....</b>	<b>87</b>
<b>APPENDIX.....</b>	<b>101</b>
<b>LIST OF ABBREVIATIONS.....</b>	<b>109</b>
<b>ACKNOWLEDGEMENTS.....</b>	<b>113</b>

# List of figures

---

<b>Figure 1.1</b>	Structural commonalities of mammalian lipids by color code.....	1
<b>Figure 1.2</b>	Overview of sphingolipid metabolism network.....	3
<b>Figure 1.3</b>	Overview of lysosomal lipid breakdown.....	4
<b>Figure 1.4</b>	Overview of lysosomal cholesterol breakdown and transport.....	5
<b>Figure 1.5</b>	Domain structure of human Niemann-Pick type C1 (NPC1).....	8
<b>Figure 1.6</b>	Protein model of human LIMP-2/SCARB2 and its putative tunneling domain.....	10
<b>Figure 1.7</b>	Lysosomal transport of cholesterol and breakdown of sphingolipids.....	13
<b>Figure 1.8</b>	Chemical structures of most common fluorescent dyes.....	14
<b>Figure 1.9</b>	Schematic representation of CuAAC click reaction.....	15
<b>Figure 1.10</b>	Schematic representation of photoaffinity labelling groups and mode of action.....	16
<b>Figure 1.11</b>	Application of bi-functional lipids in cell biology.....	17
<b>Figure 1.12</b>	Schematic diagram illustrating photolabeling and photolysis of caged compounds.....	17
<b>Figure 1.13</b>	Schematic diagram illustrating the 'click cage'.....	19
<b>Figure 1.14</b>	Schematic representation of common organelle targeting groups employed in biology.....	19
<b>Figure 2.1</b>	Chemical structure of E-64. ....	24
<b>Figure 2.2</b>	Chemical structures and synthetic procedure for a lysosome-targeted sphingosine probe.....	26
<b>Figure 2.3</b>	Subcellular localization of compound JA-052.....	26
<b>Figure 2.4</b>	Time-chase localization of compound JA-052.....	27
<b>Figure 2.5</b>	Synthesis of a lysosome-targeted coumarin cage.....	28
<b>Figure 2.6</b>	Chemical structure and synthesis procedure for Lyso-Sph.....	30
<b>Figure 2.7</b>	Synthetic route for caged cholesterol.....	30
<b>Figure 2.8</b>	Chemical structure and synthesis of Lyso-pacSph and Lyso-pacChol.....	31
<b>Figure 2.9</b>	Confocal microscopy of Lyso-pacSph and Lyso-pacChol.....	32
<b>Figure 2.10</b>	Uncaging efficiency of Lyso-pacChol.....	33
<b>Figure 2.11</b>	Time-dependent stability of lyso-pacChol and lyso-pacSph in cells.....	34
<b>Figure 2.12</b>	Stability and metabolic availability of lyso-pacChol and Lyso-pacSph in cells.....	35
<b>Figure 2.13</b>	Example of quantification of pacChol cellular uptake by TLC.....	36
<b>Figure 2.14</b>	Lysosomal uncaging of lyso-probes and their effect in intracellular Ca <sup>2+</sup> . ....	36
<b>Figure 2.15</b>	Optimization of a fixation method for Lyso-pacChol.....	39
<b>Figure 2.16</b>	Visualization of time-dependent subcellular localization of Lyso-pacChol in WT cells.....	40
<b>Figure 2.17</b>	Time-dependent visualization of lysosomal export of cholesterol in cellular disease models.....	41

<b>Figure 2.18</b>	Visualization of time-dependent subcellular localization of Lyso-pacSph in WT cells.....	43
<b>Figure 2.19</b>	Time-dependent visualization of lysosomal export of sphingosine in cellular disease models.....	44
<b>Figure 2.20</b>	Visualization of lysosomal export of cholesterol in NPC1 cells in treated and non-treated with miglustat.....	46
<b>Figure 2.21</b>	Visualization of lysosomal export of sphingosine in NPC1 cells in treated and non-treated with miglustat.....	47
<b>Figure 2.22</b>	Workflow for streptavidin pull-down of Lyso-pacSph and Lyso-pacChol probes as performed by Judith Notbohm.....	49
<b>Figure 2.23</b>	Validation of SCARB1 as a potential Sph interactor.....	51
<b>Figure 2.24</b>	Thin-layer chromatography of lysosomal export of cholesterol in cellular disease models.....	52
<b>Figure 2.25</b>	Thin-layer chromatography of lysosomal export of sphingosine in cellular disease models.....	53
<b>Figure 2.26</b>	Visualization of lysosomal export of sphingosine in WT and NPC1 KO and LIMP2 KO cells.....	54
<b>Figure 2.27</b>	Visualization of lysosomal export of cholesterol in WT and NPC1 KO and LIMP2 KO cells.....	55
<b>Figure 2.28</b>	Sphingosine accumulation is a direct effect from loss of NPC1.....	57
<b>Figure 2.29</b>	Sphingosine accumulation is a direct effect from loss of NPC1.....	58
<b>Figure 2.30</b>	Sphingosine accumulation is a direct effect from loss of NPC1 and can re-create an NPC1-like phenotype.....	60
<b>Figure 2.31</b>	In-lysate competition experiments of NPC1 with Sph and Chol.....	62

“This is one more piece of advice I have for you: don't get impatient. Even if things are so tangled up you can't do anything, don't get desperate or blow a fuse and start yanking on one particular thread before it's ready to come undone. You have to realize it's going to be a long process and that you'll work on things slowly, one at a time.”

- Haruki Murakami, *Norwegian Wood*

# Chapter 1 – Introduction

## 1.1. Cellular lipid diversity

Lipids are essential biomolecules of the cell; their diversity is fundamentally important for a wide range of cellular processes. On a physiological level, lipids serve as energy reservoirs in adipose tissue, mostly in their triglyceride form<sup>1</sup>. On a cellular level, lipids are involved in signaling events, e.g., promoting cellular proliferation upon binding to a set of distinct G protein-coupled receptors<sup>2</sup> (GPCRs) and triggering calcium release from internal stores<sup>3</sup>. Moreover, they are the main components of the plasma membrane (PM) and other subcellular organelles. Their localization and unique signature can vary from tissue, cell type and from organelle to organelle. Overall, this results in a great lipid diversity, with a thousand of different lipid species per cell<sup>4</sup>, determining properties such as membrane fluidity and permeabilisation<sup>5</sup>. Therefore, understanding the catabolic cascade, transport of lipids and inter-organelle communication is of great importance since dysregulation on any of these steps results in severe pathologies such as cardiovascular<sup>6</sup> and metabolic disorders<sup>7</sup>, which are often associated with abnormal lipid levels.

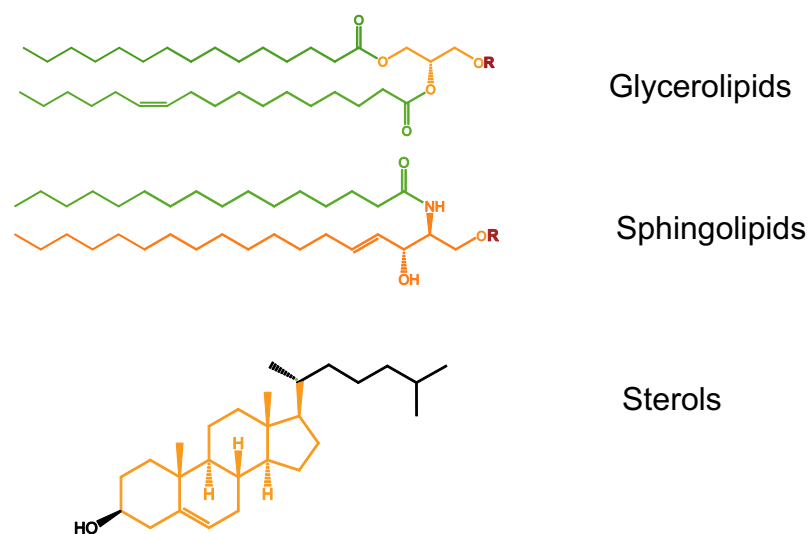


**Figure 1.1** Structural commonalities of mammalian lipids by color code. Common backbone: Orange, fatty acid: Green and R which represents a phosphate, choline, ethanolamine or sugars as head group: Red.

Due to their structural commonalities, (see figure 1.1) eukaryotic lipids can be classified into 3 major groups: glycerolipids, sphingolipids and sterols, accounting for more than 1000 lipid species<sup>8</sup>. Glycerolipids (GLs) share a common mono-, di- or tri-substituted glycerol backbone. In mammalian cell membranes, phosphatidylcholine (PC) and phosphatidylethanolamine (PE) are the most abundant phospholipids, accounting for 50-80% of total cellular phospholipids<sup>9</sup>. Sphingolipids (see figure 1.2) are a class of bioactive lipids that share a common sphingoid (long chain base) backbone (depicted in orange). This backbone in mammalian cells is sphingosine (Sph), which is the precursor to many other sphingolipid species. Moreover, sphingosine has been attributed to participate actively in events such as apoptosis<sup>10-12</sup>, regulation of calcium release from intracellular stores<sup>13,14</sup> and degradation of double-stranded genomic DNA<sup>15-17</sup>. Its backbone can be N-acylated with fatty acids (depicted in green) of variable length generating an assorted library of ceramide (Cer) species. Cer can differ in their long-chain fatty acid; this variation stems from the responsible ceramide synthase. mammalian cells have six ceramides' synthases (CerS1-6)<sup>18</sup>, each displaying a different fatty acid chain length preference, resulting in a wide array of ceramides with unique biological activities<sup>19</sup>. Cer can have a biological impact by its pro-apoptotic actions and by regulating the activities of protein kinase C  $\zeta$  (PKC)<sup>20</sup> and Cathepsin D, a ceramide-binding protein. Additionally, modifications to their headgroup (depicted in red/turquoise) define other sphingolipids such as sphingomyelin (SM) and glucosylceramide (GlcCer). Besides being structural components of the cell, lipid species such as highly glycosylated lipids reside on the outside of the PM and are important for cell recognition, immunity, among other processes<sup>21-23</sup>. On the other hand, lipid species such as sphingosine (Sph), sphingosine-1-phosphate (S1P), ceramide, ceramide-1-phosphate (C1P) and glucosylceramide (GlcCer) have been described as powerful bioactive lipids, which act as second messengers, regulating diverse cellular processes such as signal transduction pathways<sup>24</sup>.

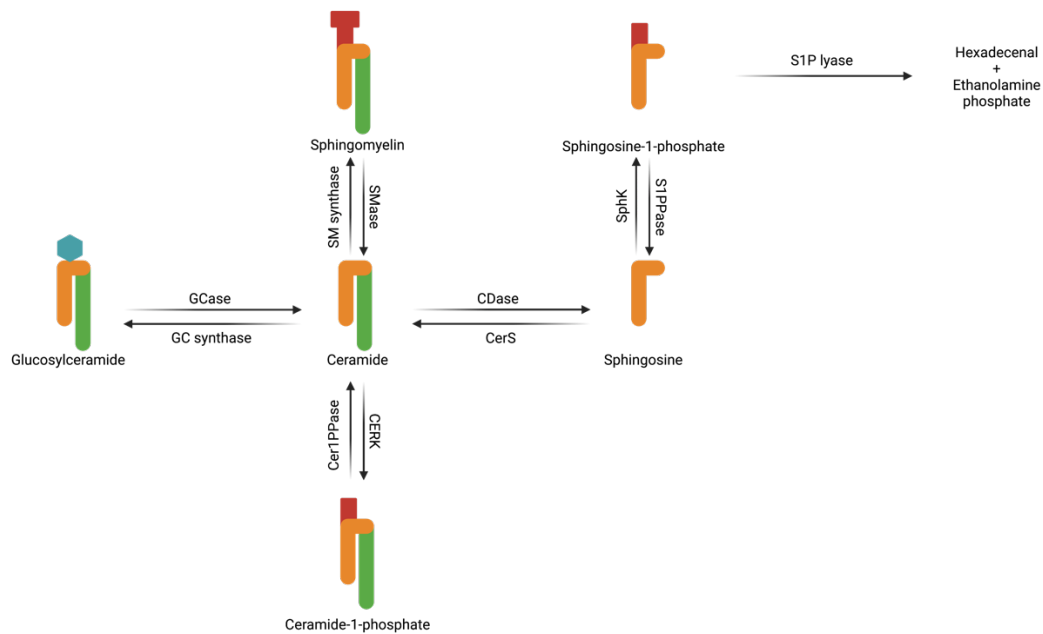


**Figure 1.2** Overview of sphingolipid metabolism network. Ceramide serves as central hub for the formation of other sphingolipid species such as higher (glyco)-sphingolipids or to the Sphingosine backbone. Created with BioRender.com

Sterols are another major lipid group, which characteristically contain a polar head, a rigid steroid backbone comprised of a fused four-ring system and a short aliphatic tail. These molecules are essential for standard cellular functions as they regulate the fluidity of membranes and have an impact on the functionality of membrane-associated proteins<sup>25</sup>. One of the most important members of this family is cholesterol – an essential component of mammalian cell membranes, which upon association with sphingolipids creates microdomains referred to as “liquid ordered domains” or “lipid rafts”<sup>26</sup>. Upon formation, they are key players in supporting biological processes such as asymmetric growth, signal transduction, cellular sorting and are crucial in infectious and metabolic diseases<sup>27</sup>.

Cholesterol and sphingolipids can be produced by cells via *de novo* by the synthesis of new substrates (which will not be discussed in this thesis), acquired from diet or obtained through the recycling and internalization of membranes and subcellular organelles derived from endo/phagocytosis. In this thesis, we will focus on the latter pathway and discuss sphingolipid catabolism inside of lysosomes and its downstream consequences.

## 1.2 Lipid breakdown occurs in lysosomes

For many years, the lysosome has been regarded as the trash can of the cell. This follows the characterization of this membrane-bound organelle containing more than 60 different enzymes, including lipases, proteases and nucleases<sup>28</sup>, which serve as host for the degradation of biomolecules derived from autophagy and other cellular trafficking pathways. Nowadays, the lysosome has gained renewed awareness among the scientific community, since it has been implicated in other processes such as nutrient sensing, where amino acids, glucose and lipids promote mTORC1 translocation to the lysosomal surface<sup>29,30</sup>. This, in turn, suppresses lysosomal catabolism through the inhibition of autophagy and lysosomal degradation<sup>31</sup>. Additionally, lysosomal malfunction can lead to a specific group of inherited metabolic disorders, known as lysosomal storage diseases (LSDs). Here, biomolecules such as lipids cannot be exported or breakdown into their respective metabolites<sup>32</sup>.

Within the endo/lysosomal (LE/LY) degradation pathway, lipids are one class of molecules being degraded (see figure 1.3). In the first step of sphingolipid catabolism, species such as SM and GSLs reach the lysosomal compartment through internalization of the plasma membrane and recycling of subcellular organelles through the autophagic pathway. Inside the lumen of LE/Lys, these complex lipids are degraded by sphingomyelases and glucosidases to form Cer. The activity of these hydrolases therefore regulates levels of lysosomal ceramide<sup>33</sup>.

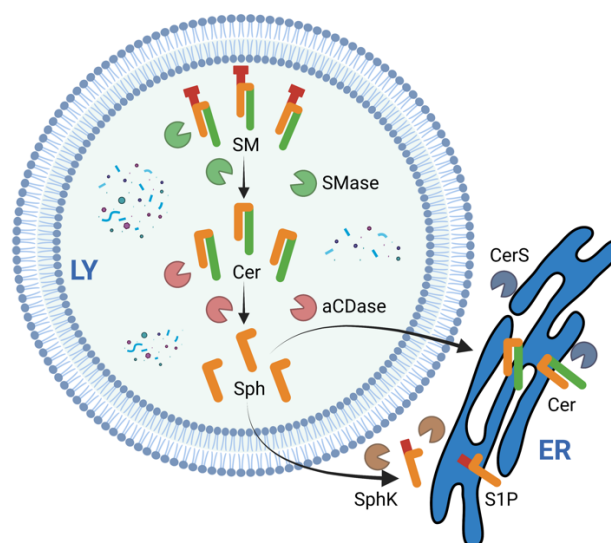


**Figure 1.3** Overview of lysosomal lipid breakdown. Lipid breakdown occurs at the lysosome via enzymatic reactions. Created with BioRender.com

In the next step of sphingolipid catabolism, ceramides are hydrolyzed by acid ceramidase (aCDase) to form Sph, which is the backbone and precursor of many other lipid species. Of note, Sph can only be generated by actions of aCDase and neutral CDase (nCDase). So far, a *de novo* synthesis pathway for Sph has been ruled out<sup>34,35</sup>. One fate of Sph is to be „salvaged” i.e., recycled back into the sphingolipid pathway, resulting in the generation of ceramides and derivatives. This pathway utilizes 50-90% of the lysosomally-derived sphingoid base pool<sup>36,37</sup>. Alternatively, Sph can be phosphorylated either by sphingosine kinase 1 or 2 (SK1/SK2), cleaved by sphingosine-1-phosphate lyase (SGPL1), converted into hexadecanoic acid and further incorporated into glycerolipids.

Alongside sphingolipids, other lipids are also degraded in the lysosome. Here, the biologically active class of sterols, with cholesterol being particularly well studied, are of interest. Dietary cholesterol reaches cells in plasma-low-density lipoprotein form (LDL), which binds to LDL receptors (LDLR) at the PM of target cells and is internalized via clathrin-mediated endocytosis<sup>38</sup>. Once taken up, LDL particles dissociate from LDLR due to a decrease of pH in late endosomes from where LDLR is recycled back to the PM<sup>39</sup>. Next, LDL is hydrolyzed by the actions of lysosomal acid lipase, triggering the release of cholesterol and triglycerides<sup>40</sup>.

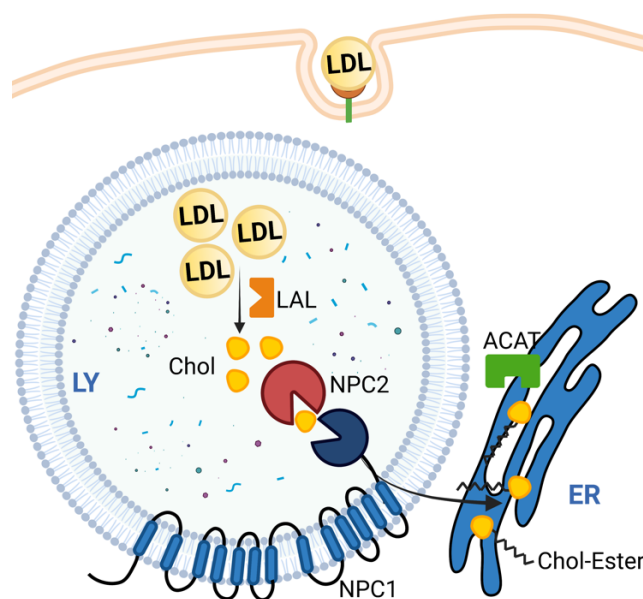


**Figure 1.4** Overview of lysosomal cholesterol breakdown and transport. Cholesterol reaches lysosomes on its LDL form and hydrolyzed to release cholesterol and triglycerides. Created with BioRender.com

### 1.3 Subcellular transport of lipids

Lipid *de novo* synthesis starts at the ER<sup>41</sup>, where many lipid enzymes are located<sup>42</sup>. Here, the cell synthesizes structural phospholipids, sphingolipids, sterols and as well significant levels of triacylglycerol and cholesteryl esters. The ER distributes lipids towards organelles, which are unable to synthesize or are limited by their capacities. Therefore, transport of lipids between organelles requires dedicated and specialized carrier proteins or lipid transfer proteins (LTPs), tethering complexes acting at membrane contact sites (MCS) or vesicular flux of lipids. All of these are fundamental processes to ensure cell survival and membrane formation.

Although the ER is key player in cholesterol and sphingolipids biosynthesis, these species are promptly transported to other subcellular organelles<sup>43</sup>. Here, the Golgi apparatus plays an important role, as chief organelle of the secretory pathway, where lipids such as Cer are transported via ER-Golgi MCS. Here, ceramide-transfer protein<sup>44</sup> (CERT) interacts with vesicle-associated proteins<sup>45,46</sup> (VAPs) at the ER to tether Golgi to ER in order to facilitate Cer transfer to the Golgi for further metabolism to complex sphingolipids. SM for instance, can leave the Golgi via vesicular transport<sup>47</sup>. Here, p24, a type I membrane protein that is involved in vesicular transport at the early secretory pathway, contains a specific sphingolipid-binding motif, sorting a single molecular species of sphingomyelin, SM 18:0 into vesicles<sup>48,49</sup> on a retrograde transport from the Golgi to the ER. Other lipids are trafficked in a non-vesicular fashion. GlcCer uses the four-phosphate adaptor protein 2 (FAPP2) to travel from the cis-Golgi to the trans-Golgi network<sup>50,51</sup>, where it is exclusively incorporated into globosides, such as globotriaosylceramide (Gb3). The levels of ceramide-1-phosphate at the trans-Golgi network are governed by a dedicated ceramide-1-phosphate transfer protein (CPTP)<sup>52</sup>, which shuttles C1P to the trans-Golgi or the PM. Additionally to sphingolipids, cholesterol is another component that can move through the secretory pathway. Cholesterol levels are increased in a gradient manner, from 5% mol at the ER to 20-30% mol at the *trans* Golgi<sup>53</sup>. The mechanism of transport of cholesterol from ER-Golgi is governed by an oxysterol binding protein (OSBP) at MCS. OSBP exhibits a similar domain organization as CERT, which includes a PH domain and a central FFAT motif. Here, PH binds to PtdIns(4)P at the Golgi and its FFAT motif interacts

with ER-resident VAPs. Then the OSB-related domain (or ORD domain) can bind and transfer cholesterol from ER to the Golgi membrane while shuttling PtdIns(4)P in the opposite direction<sup>43,54</sup>.

Post-Golgi transport shuttles the sorted (sphingo)-lipids to the PM, where they are sensed, maintained and recycled via the LE/LY compartment.

### **1.3.1 Lysosomal efflux of (sphingo)-lipids**

The catabolites resulting from lysosomal hydrolysis of lipids need to be exported from the endo/lysosomal pathway to several acceptor compartments to be re-used in cellular metabolism, these compartments include the ER, Golgi, PM, peroxisomes and mitochondria. However, one unsolved question is: Does the transport of each lipid species use a separate route, or do they share a common export pathway?

Cholesterol is an exemplary lipid, as its transport out of the lysosome to other compartments has been extensively studied<sup>55–57</sup>. The endo/lysosomal pathway obtains cholesterol from LDL particles and employs the concerted action of two proteins, membrane-bound NPC1 and soluble NPC2 for its efflux from the lysosome<sup>58–61</sup>. In order for cholesterol to exit lysosomes, NPC2 an intra-lysosomal soluble protein picks up de-esterified cholesterol from intraluminal vesicles in an equimolar ratio. NPC2 shields the aliphatic tail of cholesterol from the aqueous environment by burying it deep in its hydrophobic pocket<sup>58,61–64</sup>. Then NPC2-bound cholesterol (with its 3- $\beta$  hydroxyl group exposed) is transferred to the N-terminal domain of NPC1 from where it can exit the endo/lysosomal pathway. NPC1 is a ubiquitous, 13 transmembrane domain protein that is located to the limiting membrane of endo/lysosomes (see figure 1.5). Its cellular functions are not yet fully clarified, but on the physiological level, NPC1 has been implicated in Ebola and Marburg virus infection<sup>65,66</sup> and the neurodegenerative Niemann-Pick disease type C disease<sup>32,67–69</sup> a known autosomal, recessive, LSD which it is caused by mutations in the genes encoding for NPC1 (95% cases) and NPC2 (5% cases) leading to atypical storage of lipids such as Chol, Sph, SM and glycosphingolipids inside lysosomes<sup>70–73</sup>. Additionally, NPC1 disease causes a perturbation in the function of Rab7 and Rab4 proteins<sup>74</sup>. On the molecular scale,

NPC1 comprises a sterol-sensing domain (SSD) which in collaboration with the N-terminal domain (NTD) has been demonstrated to bind to cholesterol and facilitate its transport through its SSD, which forms a cavity ('tunnel') accessible from both luminal bilayer leaflet and endosomal lumen<sup>59,75,76</sup>. This cavity has been shown to accommodate and facilitate cholesterol transport. Besides cholesterol, this tunnel can also lodge other molecules such as U18666A an amphiphilic drug that impairs cholesterol transport, and causing it to accumulate in endo/lysosomes resembling an NPC1-like defect<sup>77</sup>. Moreover, other triazole antifungal drugs have been also demonstrated to have an inhibitory effect on NPC1 and impaired cholesterol transport by accessing and binding to this cavity<sup>78,79</sup>.

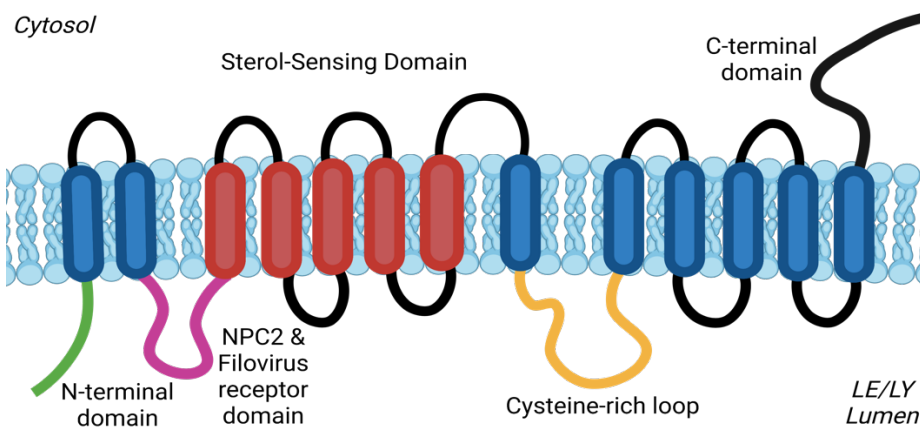


**Figure 1.5** Domain structure of human Niemann-Pick type C1 (NPC1) adapted from<sup>80</sup> Created with BioRender.com

In *in vitro* studies, NPC2 could deliver cholesterol directly to acceptor liposomes in the absence of NPC1<sup>81,82</sup>. This traffic is facilitated by lysobisphosphatidic acid (LBPA). However, the lack of NPC2 in experiments employing only the N-terminal domain of NPC1 failed to deliver cholesterol to synthetic vesicles and could only be transported in the presence of NPC2<sup>58,61</sup>. *In vivo* experiments, as seen from our lab and published by others, showed that lack of functional NPC1 or NPC2 resulted in accumulation of cholesterol in LE/LYs as seen by filipin staining. It is tempting to speculate that NPC1 deficiency causes a 'storage' as seen from lipidomic studies<sup>83</sup> and from studies where NPC1 interacts with resident proteins to form tethering functions to transport cholesterol out of the lysosomes. Whereas lack of NPC2 causes delayed transport i.e., bottleneck traffic. Moreover, NPC1 has been further shown to interact at MCS with ER-resident proteins such as the oxysterol-binding related protein 5 (ORP5)<sup>84</sup> and

GRAM domain containing 1b (Gramd1b)<sup>85</sup>. This tethering function is potentially implicated in maintaining functional cholesterol transport to the ER. Interestingly, 30% of LDL-derived cholesterol moves from the endo/lysosomal pathway directly to the ER, without passing first through the PM. At the ER, sterol levels are sensed, and cholesterol biosynthesis is regulated accordingly. Cholesterol can then move between organelles, to the PM to play structural roles and/or to the ER, turning off a transcriptional driver for cholesterol synthesis and uptake by blockage of sterol regulatory element-binding proteins (SREBPs)<sup>86</sup> and last, excess of cholesterol is converted into cholesteryl esters for storage in lipid droplets<sup>87</sup>. Given the importance of the direct route, other sterol transport proteins (STPs) such as oxysterol-binding related protein 1L ORP1L and StAR related lipid transfer domain containing 3 (STARD3) are found/enriched at endo/lyso-ER contact sites and facilitate the delivery of lipoprotein-derived cholesterol to the ER<sup>88–90</sup>.

Parallel to NPC1, recently, other lysosomal abundant membrane proteins such as LAMP1/2<sup>91</sup> and the lysosomal-integral membrane protein LIMP-2/SCARB2 have been shown to play a role in lysosomal cholesterol export<sup>92</sup>. LIMP-2/SCARB2 was proposed to be an essential requirement for lysosomal maintenance and biogenesis<sup>93,94</sup>. This endo/lysosomal protein has been previously shown to deliver the acid hydrolase  $\beta$ -glucocerebrosidase (GC) to lysosomes<sup>95,96</sup> and its mutation/deletion is associated with another LSD: Gaucher disease<sup>97,98</sup>. Moreover, LIMP-2 serves as a receptor for enterovirus 71 and coxsackieviruses<sup>99</sup>, which cause hand, foot and mouth disease. On a molecular level, the LIMP-2/SCARB2 crystal structure revealed a large cavity ('tunnel') through its luminal domain<sup>100</sup> (see figure 1.6).

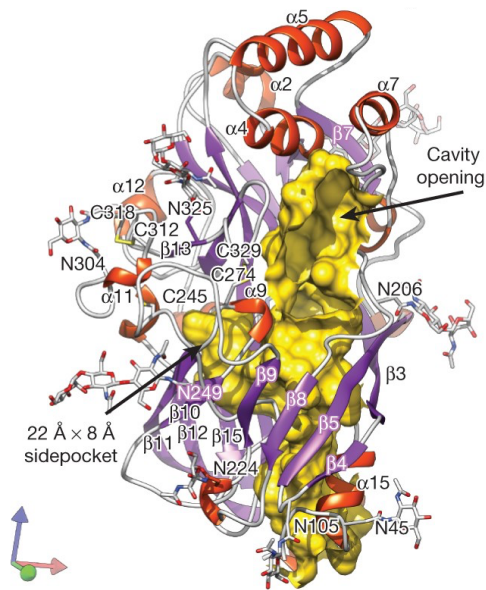


**Figure 1.6** Protein model of human LIMP-2/SCARB2 and its putative tunnelling domain. Taken from: <https://doi.org/10.1038/nature12684> under license number 5239261484788

This cavity it is similar to its family members CD36 and SR-B1, the latter being able to deliver cholesterol from lipoproteins to the PM<sup>101–104</sup>. Therefore, it is not surprising that deletion of LIMP-2 has an impact on the delivery of cholesterol to the lysosomal membrane, resulting in the alteration of SREBP-2 mediated cholesterol regulation and formation of LD<sup>92</sup>. However, it is important to address that loss of LIMP-2 does not cause an NPC1 phenotype as experimentally seen by us and the Saftig lab, potentially implicating LIMP-2/SCARB2 in an alternate, slower scenario for cholesterol export.

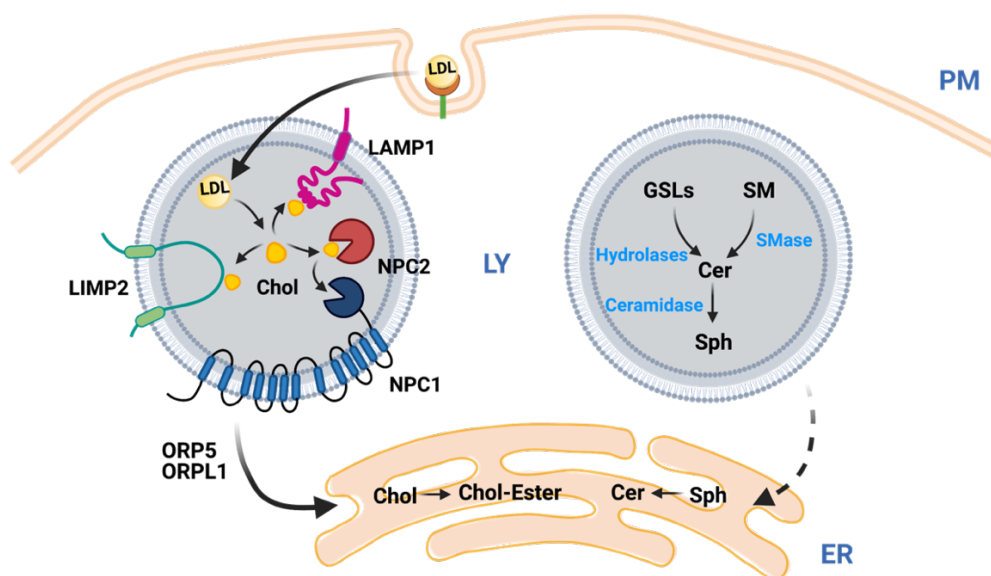


**Figure 1.7** Lysosomal transport of cholesterol and breakdown of sphingolipids. Created with BioRender.com

While several of the transport proteins of cholesterol have been identified, other lipid degradation products such as fatty acids or sphingosine also need to be exported from the lysosome in a similar manner (see figure 1.7). Their transport pathways, however, are not yet elucidated. Interestingly, sphingosine is among the lipids accumulated in Niemann-Pick disease type C disease, hinting at a potentially shared export pathway. The reason so little is known about sphingosine exit from lysosomes is a lack of tools to manipulate and investigate such lipid species. Next, we will discuss tools for investigating (sphingo)-lipid biology

## **1.4 Chemical biology tools to study (sphingo)-lipid biology**

Studying and manipulating lipids, especially sphingolipids, in a cellular context, has always been a challenging task. Their synthesis and breakdown are results of specific enzymatic reactions (see chapter 1.2) in which gives rise to a framework in which lipids in cells are well-organized in a highly and tightly regulated signaling network<sup>105</sup>. Lipid research is hindered by the lack of tools to study lipids in their natural environment while minimizing the modifications needed to track or detect certain lipid species. Chemically modified lipids have been attractive and still to date useful tools. Still, due to the relatively small size of a lipid, use and position of chemical modifications are crucial for the selection of the probes, since masking or changing specific parts of the lipid (e.g., head group) could dramatically affect the biophysical properties and signaling outcomes of the lipid<sup>106</sup>. Here, we will discuss the past and present of chemical biology probes in lipid cell biology.

### **1.4.1 Radiolabeled lipids**

For many years, radioactive studies have been gold standard in revealing key enzymatic reactions involved in lipid biosynthesis and transport. Methods have been reported for labeling cholesterol and sphingolipids, either incorporating <sup>3</sup>H or <sup>14</sup>C isotopes to their native structure or using isotope-labeled precursors such as fatty acids, choline, L-serine or acetate<sup>107–109</sup> to reveal kinetics of sphingolipid and sterol synthesis and transport across organelles. This way, fundamental questions were answered, shedding light on the initial steps of sphingolipid biosynthesis, revealing in

which step of the sphingolipid biosynthesis a double bond is inserted<sup>110,111</sup>, or which enzymes are required in catalyzing the conversion from dihydrosphingosine (dhSph) to dihydroceramide (dhCer) and subsequently to ceramide<sup>112</sup>. Furthermore, radiolabelling methods shed light on cholesterol biosynthesis, transport from the ER to other organelles such as mitochondria and/or PM<sup>113,114</sup> and elucidated that cholesterol transport *in vitro* is dependent on the orchestrated actions of NPC1 and NPC2 proteins<sup>115,116</sup>.

Despite all these findings, radiolabeled experiments are not well suited to answer complex questions on the (sphingo)-lipid field, where a detailed picture of their subcellular localization and potentially protein interaction(s) are needed. Radiolabeled lipids can rarely be detected by real-time methods, such as microscope-based techniques. Additionally, labeling biosynthetic precursors also gives rise to a large number of radiolabeled species, often complicating the readout.

### **1.4.2 Fluorescent lipids**

An important breakthrough was achieved by the chemical labeling of lipids with fluorescent tags. These lipid analogues are covalently linked to fluorescent dyes (see figure 1.8) such as fluorescein, rhodamine, nitrobenzoxadiazole (NBD), coumarin and BODIPY-like structures, among others<sup>117</sup>. The fluorescent moieties are attached to their acyl chain or head group of the lipid. Using these probes, first insights were obtained about sphingolipid metabolism<sup>118</sup>, staining of vital organelles such as the Golgi apparatus<sup>119</sup>, diffusion of phospholipids<sup>120</sup>, redistribution and capping of gangliosides at the PM<sup>121</sup> and more recently visualization of sterol trafficking on a cellular and living organism context<sup>122</sup>.

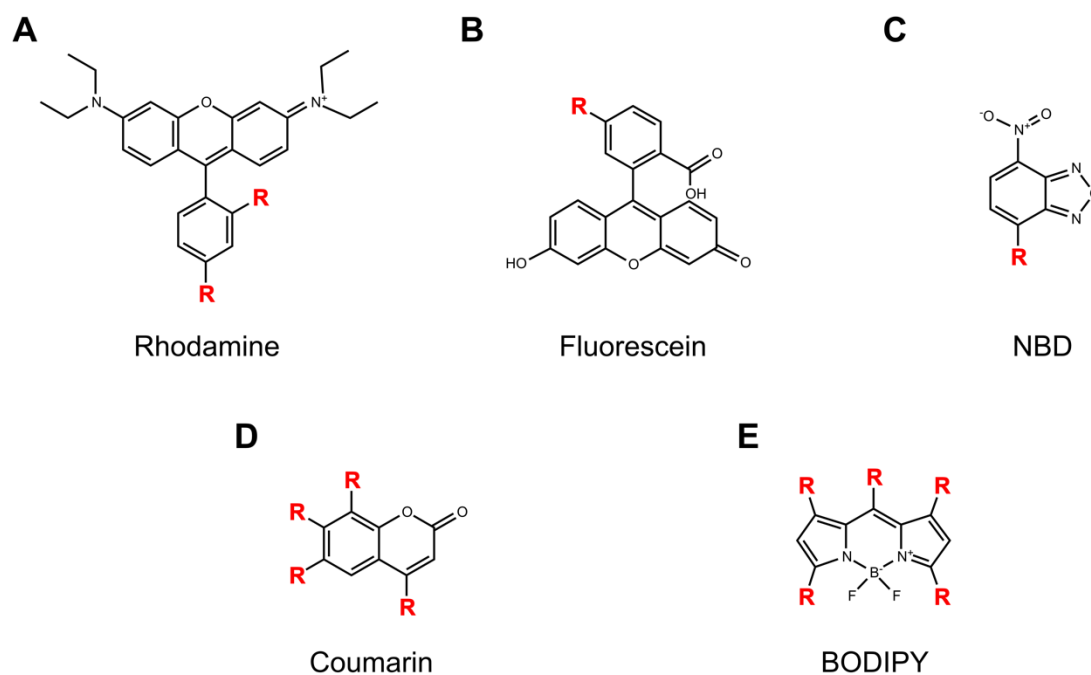


**Figure 1.8** Chemical structures of most common fluorescent dyes. R (depicted in red) represents further chemical modifications, such as functional groups or lipid attached molecules.

However, many of these lipid analogues contain head group modifications which can cause a loss in the biological activity of the lipid e.g., affecting lipid transbilayer movement, lipid missorting<sup>123</sup> and delayed or prematurely stopped metabolism<sup>124–126</sup>. Additionally, many of these lipid analogues contain fluorescent dyes on the visible-light region which often confer increased hydrophilicity to the lipid probe. Therefore, many of these constructs might exhibit additional drawbacks such as aberrant lipid integration into synthetic membranes, causing abnormal structures<sup>127,128</sup> and increased kinetics, leading to a fast undesirable lipid exchange between donor-acceptor membranes<sup>129</sup>.

### 1.4.3 Bioorthogonal chemistry: Probing for targets with chemically modified biomolecules

#### 1.4.3.1 Click chemistry

Biorthogonal chemistry is a modern approach for overcoming the limitations of fluorescent lipids. Here, small chemical reporters such as an azide, alkyne, aldehyde, tetrazine, alkene, among others are chemically introduced or pre-tagged to the

biomolecule of interest<sup>130</sup>. Then, a bioorthogonal chemical reaction is performed *in situ*. In order to perform a chemical reaction on a living system, it is important that this reaction proceeds under physiological conditions with respect to pH, temperature and aqueous environment and additionally must be non-toxic and non-invasive *per se*. Reactions conforming to these criteria were grouped to “click chemistry” reactions<sup>131</sup>, by Sharpless and co-workers about two decades ago. The most famous and most often applied click reaction is a highly regioselective reaction involving azides with terminal alkynes to form a 1,4-disubstituted-1,2,3-triazole (see figure 1.9).

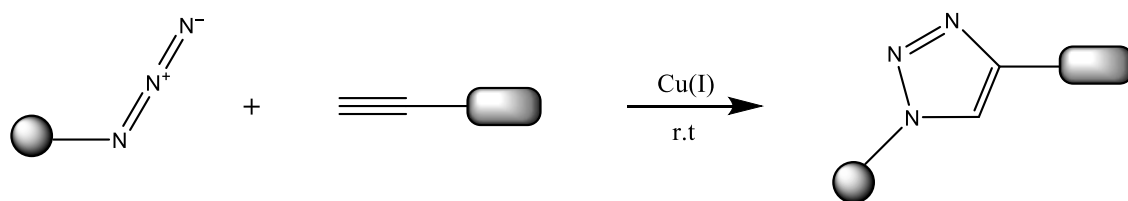


**Figure 1.9** Schematic representation of CuAAC click reaction

This approach has been applied to diverse biomolecules e.g., lipids<sup>132–135</sup>, glycans<sup>136–138</sup> or nucleic acids<sup>139</sup> to map protein-lipid interactions, metabolism and direct visualization of lipid-protein complexes.

### 1.4.3.2 Photoaffinity labeling

Bioorthogonality is not restrictive to one reaction by biomolecule of interest. Photoaffinity labeling (PL) is an elegant approach for screening protein-protein or protein-lipid interactions. In PL experiments, small chemical moieties such as a diazirine, phenyl azide or benzophenone (see figure 1.10) are introduced to the biomolecule of interest. Upon UV irradiation a highly reactive species, such as a radical, carbene or nitrene is formed, reacting with any molecule in proximity, resulting in a direct covalent bond between the probe and the target (see figure 1.10).

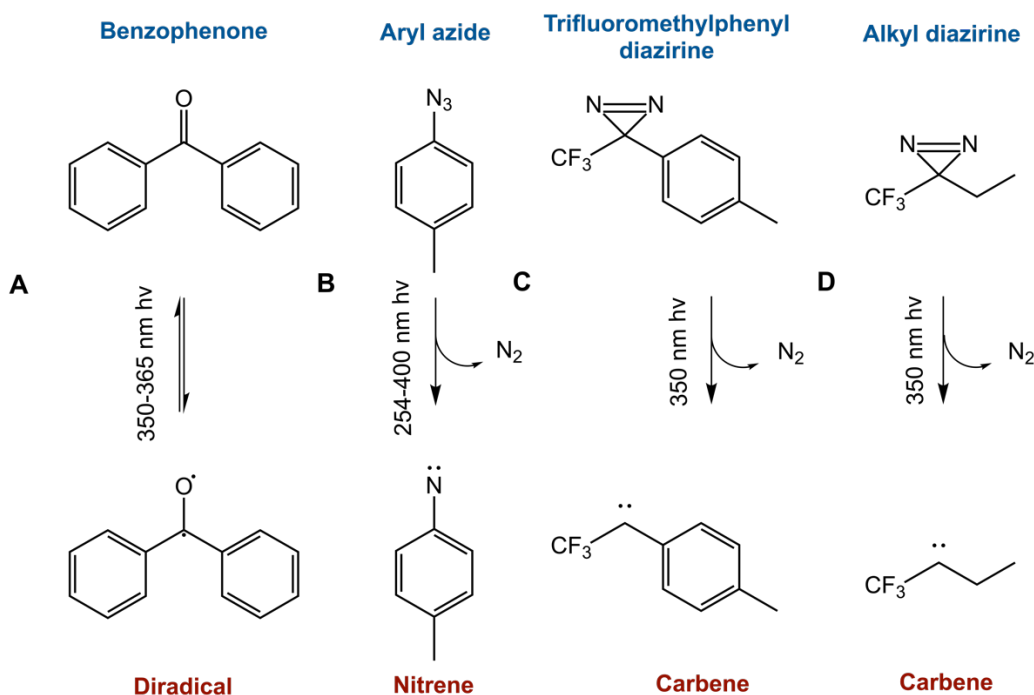


**Figure 1.10** Schematic representation of photoaffinity labelling groups and mode of action

PLs have been extensively used since their discovery<sup>140</sup>, they have been applied to map ligand-binding sites in GPCRs<sup>141–143</sup>, drug binding sites<sup>144,145</sup> and such elegant approach has been extended to other small molecules such as lipids<sup>146</sup>.

### 1.4.3.3 Caged, bi-, tri-functional and organelle-targeted lipids: release of lipids with spatial-temporal resolution

Following this concept, bi-functional lipids were created. An exquisite combination of both, an alkyne and diazirine which are introduced to the acyl chain and/or backbone of a lipid, confer minimal structural modifications. In this way, these powerful tools mimic their counterparts closely. By feeding cells with a bi-functional lipid, UV illumination at 365 nm and click reaction to either a fluorophore or a biotin-tag, their subcellular localization and downstream metabolites can easily be traced (see figure 1.11).

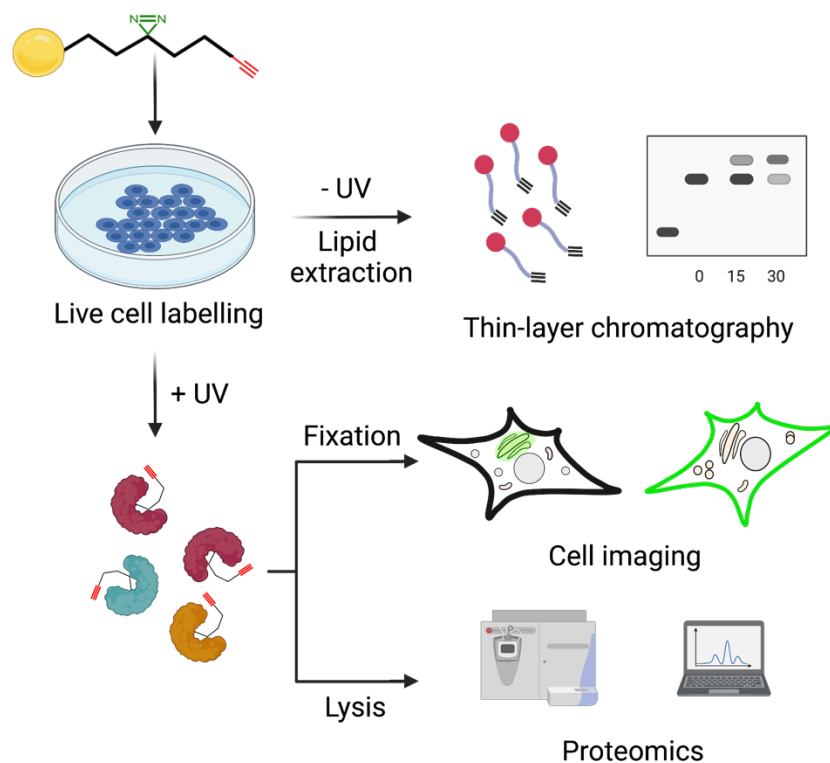


**Figure 1.11** Application of bi-functional lipids in cell biology. Due to their chemical modifications such as an alkyne-bearing group, bifunctional lipids can be employed on metabolism studies by TLC or more sophisticated methods such as lipidomics. Due to their additional photocrosslinkable moiety 'diazine ring' lipids can be crosslinked and form protein-lipid complexes which can be visualized via an azide-containing fluorophore or map for protein-lipid interactions via a pull-down biotin-streptavidin. Created with BioRender.com

Following this principle, diverse lipid analogues have been synthesized, expanding the chemical biology toolbox of lipids. The respective bifunctional cholesterol was the first lipid reported to include an alkyne and diazine ring on its design<sup>147</sup>. These chemical modifications to the fused four-ring and isooctyl chain of cholesterol, allowed proteome wide-mapping of cholesterol interacting partners, yielding over 265 cholesterol interacting partners, confirming proteins such as NPC1 as *bona fide* sterol transport protein. Besides cholesterol, other exemplary lipids have been synthesized and employed successfully in the past, such as sphingosine<sup>148</sup>, fatty acids<sup>149</sup> and ceramides<sup>150</sup>. Using these bi-functional analogues, several proteomic studies have been performed, in cells<sup>85,147–149,151–155</sup>, yeast<sup>156</sup> or whole organisms<sup>149</sup> confirming known interactors as well presenting high confidence candidate binding proteins. Together, these bifunctional, or sometimes referred to as photoactivatable and clickable (pac) lipids, are suitable and versatile tools to investigate lipid biology in mechanistic depths. However, one major disadvantage of this approach is the rapid

incorporation of pac-lipid precursors into a host of downstream metabolites, which makes the determination of the precise interacting lipid a major challenge. One could design experiments in such a way as the Brügger lab achieved by generating a CRISPR knockout cell line of the SGPL1 gene<sup>157</sup>, therefore avoiding cleavage of Sph and further incorporation of the labeled precursor into the glycerolipid pathway, limiting experimental readouts to species containing the Sph backbone. Other approaches could be using known lipid enzyme inhibitors e.g. Fumonisin B1, Avasimibe, D609 among others, or employing siRNAs. The latter offers a window of time for cells to adapt and compensate by regulating other signaling pathways.

---

An alternate chemical biology approach to overcome premature metabolism employs photolabile protecting groups (PPGs), sometimes called caging groups<sup>158</sup>. The most common PPGs are ortho-nitrobenzyl (NB), BODIPY and coumarin-based caging groups<sup>159</sup>. This strategy has been widely used to circumvent premature actions of biomolecules of interest with a high temporal resolution (see figure 1.12). and has been applied to molecules such as ATP<sup>160</sup>, Ca<sup>2+</sup><sup>161</sup>, glutamate<sup>162</sup>, diazepam<sup>163</sup>, and lately to lipids, such as cholesterol<sup>164</sup>, sphingosine<sup>153,165</sup>, arachidonic acid (AA)<sup>153–155</sup>, phosphoinositides<sup>166</sup> and fatty acids<sup>149</sup>.

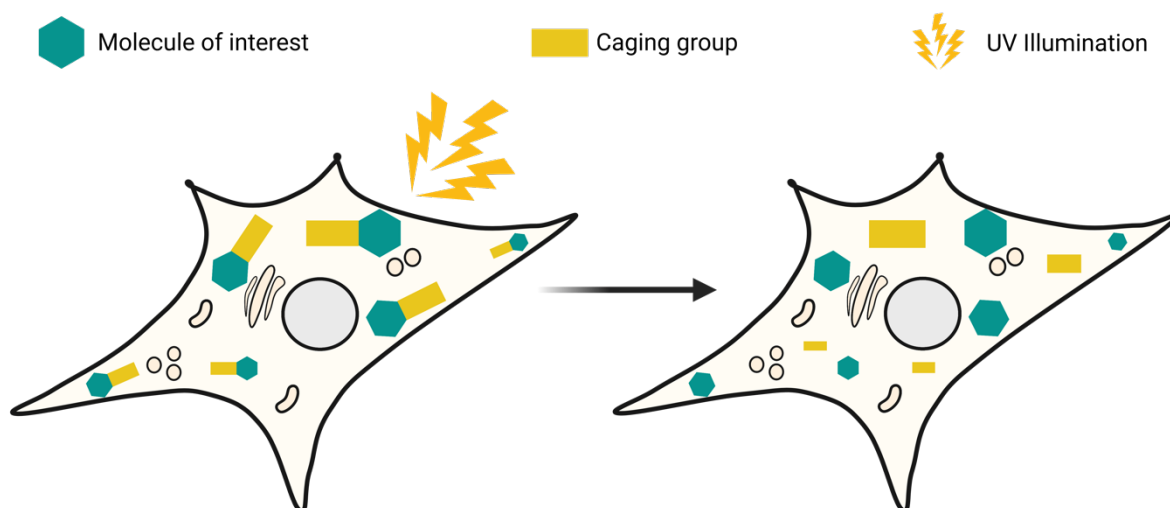


**Figure 1.12** Schematic diagram illustrating photolabeling and photolysis of caged compounds. Caging groups serve as masks for biomolecules of interest, which can later be cleaved with a flash of light to release the active molecule and study its intrinsic actions. Created with BioRender.com

Among PPGs, coumarin-based groups have been predominantly used to cage lipids due to relative ease of synthesis and rapid light-release control over the substrate<sup>167–</sup>

<sup>169</sup>. Moreover, the hydrophilic headgroup of lipids is usually composed of easily modifiable chemical groups such as amines, phosphate or alcohol. These can be straightforwardly connected to the coumarin cage via a carbamate, carbonate or phosphate bond, giving rise to favorable kinetics of the cleaving reaction due to the requirement of low pKa of the leaving group<sup>170</sup>. Overall, the caging strategy can circumvent the pitfalls of the direct addition of lipid substrates to the medium, i.e., fast metabolism and multiple downstream metabolites.

Combining the caging and bifunctional lipid concepts Höglinger *et al.* synthesized tri-functional caged, sphingosine (TFS), diacylglycerol (TF-DAG) and C15 fatty acid (TF-FA) probes<sup>153</sup>. These lipids probes feature superior temporal resolution since the liberated pac-lipid species are only incorporated into their respective metabolic pathways after photo-liberation (uncaging). An additional, photocrosslinking reaction can reveal their subcellular localization over time. Moreover, chemoproteomic profiling yielded over 73 sphingosine binding proteins, from which 65 proteins were identified as high-confidence proteins meaning they were not identified when using control lipids TF-FA or TF-DAG<sup>153</sup>. Interestingly, a possible and exciting new role for proteins such as STARD3, a cholesterol transporter from the ER to the LE/LY<sup>90,171</sup> as a possible sphingosine carrier was revealed in this study. Although caging groups are an elegant method to mask lipids and offer a delicate and high temporal resolution due to their optic properties, this technique is hindered by its spatial resolution, since the cage by itself accumulates strongly on internal cellular membranes such as the ER and the Golgi<sup>153,165,172</sup>.

Conventional laboratory microscopes do not offer or have a poor distribution of light on a specific subcellular area, making it difficult to specifically liberate caged lipids in certain organelles but the actions of lipids among other molecules show a clear dependence on subcellular localization. Therefore, the latest efforts for understanding lipid metabolism and trafficking have resulted in successful pre-localization of natural lipids into diverse organelles and the creation of new tools such as the 'click cage'<sup>152</sup>. This coumarin-based approach is integrated with an alkyne moiety which can later be combined with azide-modified organelle-targeting moieties by a bioorthogonal click chemistry reaction (see figure 1.13).

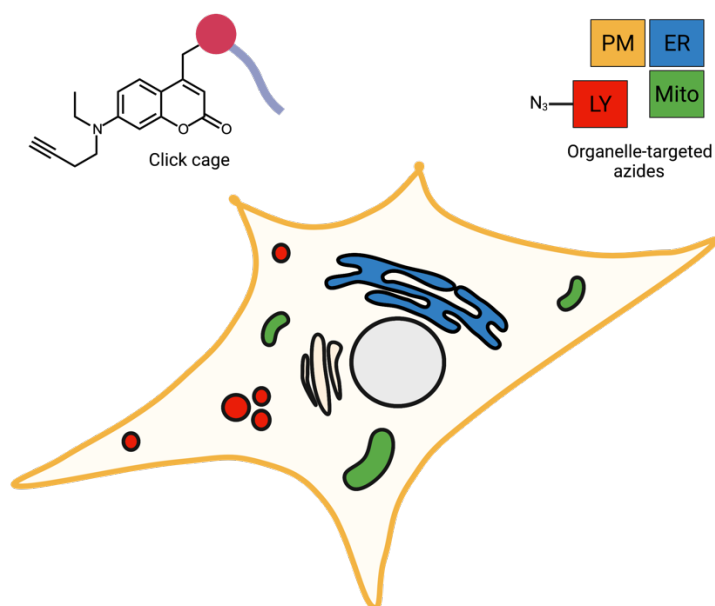


**Figure 1.13** Schematic diagram illustrating the 'click cage'. Adapted from<sup>152</sup> Created with BioRender.com

Organelle-targeting is not a novel concept in chemistry or biology, in fact, several commercially available dyes employed in fluorescent microscopy bear covalently attached moieties, which accomplish subcellular discrimination. Such an elegant concept has been widespread in a variety of fields such as chemical biology and drug discovery. But how is selectivity over other cell structures achieved? Many (bio)chemical reactions employing enzymes, ions/anions and reactive oxygen species (ROS)<sup>173,174</sup> occur actively within the cell, several of these reactions appear to be concentration-dependent and additionally have been demonstrated to take place in specific organelles. This way, the differences in chemistry between organelles have been revealed and small chemical groups<sup>175</sup> (see figure 1.14) were identified, which drive selective accumulation inside targeted organelles such as mitochondria, ER, LY and PM.

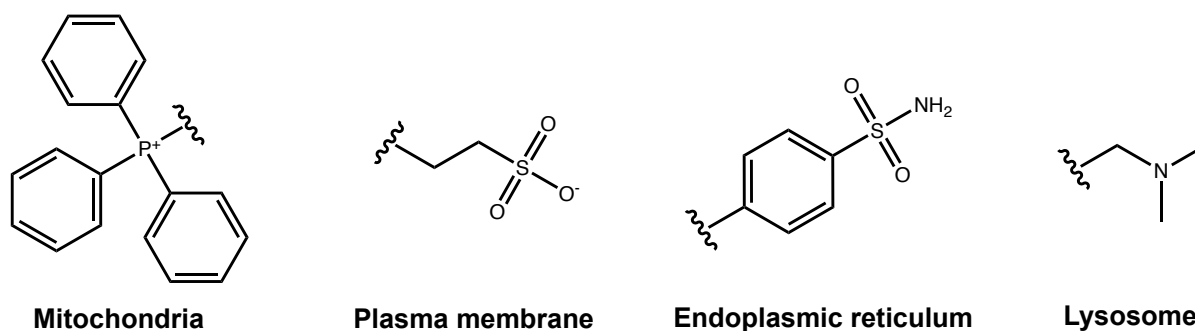


**Figure 1.14** Schematic representation of common organelle targeting groups employed in biology.

For example, a reported chemical targeting group for mitochondria is a triphenylphosphonium (TPP) cation. Due to the membrane potential of 200 mV of the mitochondria<sup>176</sup>, lipophilic cations such as TPPs can penetrate and accumulate within its matrix<sup>177,178</sup>. Similarly, PM-targeted probes are retained at the outer leaflet due to their heavily negatively charged groups such as sulfonates and carboxylic acids<sup>154,179,180</sup>. The exact mechanism of ER-targeting remains unclear, however, moieties such as a *p*-toluenesulfonamide group<sup>181,182</sup>, allow binding to cyclooxygenases (COX) which are abundant at the ER. Additional small amphiphilic or lipophilic groups such as a perfluorinated aryl group have been recently described<sup>152,180</sup>. LE/LY features a uniquely low pH value of 4 to 5, acquired through actions of V-type ATPases<sup>183</sup>. As a result, many LE/LY fluorescent probes are based on the lysosomotropic properties of these endocytic organelles, where small lipophilic basic moieties, especially lipophilic amines selectively accumulate in acidic stores<sup>184</sup>. Specifically, weakly basic amines such as a morpholine<sup>185</sup> or N,N-dimethylethylenediamine<sup>186</sup> groups can readily cross the lysosomal membrane, become protonated and retained because of their newfound membrane impermeability due to their acquired positive charge. Therefore, combining these properties, the 'click cage' method enabled the successful pre-localization of mitochondria-, lysosome-, PM- and ER-targeted caged sphingosine and arachidonic acid derivatives<sup>152</sup>. Other, almost simultaneously reported approaches used direct incorporation of the targeting moiety to the core of the coumarin cage, giving rise to PM-targeted AA, lysosome (Lyso-So), and mitochondria-targeted sphingosine (Mito-So) and cholesterol derivatives<sup>154,187,188</sup>. This way, Feng *et al.* found that Mito-So could rapidly be phosphorylated and converted into S1P, by actions of SK1/SK2 as shown by inhibition studies<sup>187</sup>. Whereas Lyso-So showed almost no conversion into S1P, demonstrating the importance of lipid localization in metabolism. Moreover, studies with Mito-So failed to trigger calcium release<sup>188</sup>, which also implies that the signaling actions of lipids, such as sphingosine are governed by their subcellular localization.

In sum, these methods offer a high-spatiotemporal resolution. Yet, the pre-localization concept has not been applied to studying questions related to which proteins are involved in intracellular transport. We anticipate that the creation of such tools will allow us to answer biological questions on a subcellular level.

# Objectives of this thesis

---

Studying and manipulating lipids in a subcellular context is a great challenge. To date, many experimental approaches rely on whole-cell level methods to perturb lipid levels and trigger cell-wide responses. Many of these methods rely on molecular biology techniques such as using siRNAs for gene silencing and require long time incubations, which gives a window of time for cells to adapt and compensate by regulating other signaling pathways. Other conventional methods such as feeding cells with lipid precursors to artificially increase lipids levels are subject to cellular metabolism and give rise to a host of metabolites. While state-of-the-art chemical biology tools have been created to overcome those drawbacks, methods that combine the high temporal resolution of caging groups and the subcellular specificity of organelle-targeting chemistry with bifunctional lipid modifications to track lipid metabolism, intracellular transport, and binding partners are still missing.

Considering these challenges, the aim of this thesis is to manipulate cholesterol and sphingosine levels on a subcellular level, particularly at the lysosome, in order to answer remaining questions about the mechanism of sphingosine exit from lysosomes. By combining the above-mentioned chemical biology concepts, we created lysosome-targeted caged compounds Lyso-pacSph and Lyso-pacChol (Lyso = **L**ysosome, pac= **p**hotoactivatable and **c**lickable). Due to their features, these probes allow us to achieve exquisite control over lipid concentration and localization with high temporal and spatial precision. These probes will be applied in a cellular context to characterize their stability and subcellular localization. Additionally, the lyso-probes will be employed in studying post-lysosomal metabolism and localization after pulse-chase experiments as well as in mass spectrometric screening experiments to identify novel lysosomal sphingosine and cholesterol binding proteins. Altogether, these varied applications will allow for thorough characterization of their effects on lipid metabolism and transport.

Given that lysosomal egress of sphingosine is still enigmatic and of particular relevance in lysosomal storage disorders such as NPC, we anticipate that the results of our screening will allow us to further investigate the pathobiochemistry of this storage disorder. Specifically, we hypothesize that the molecular mechanisms of cholesterol exit (which is affected in NPC) are shared with sphingolipid export, specifically with sphingosine. To investigate this hypothesis, we will perform competition experiments with sphingosine and cholesterol in living cells, allowing us to follow the export kinetics of one lipid in the presence of an excess of the other lipid. Such sophisticated experiments will contribute to unraveling the mechanisms contributing to the lipid accumulations characteristic of these storage disorders.

# Chapter 2 – Results and discussion

---

## **2.1. Targeting cholesterol and sphingosine to lysosomes – A new approach for studying their subcellular actions**

Studying the specific actions of (sphingo)-lipids is a challenging task. Therefore, in order to understand their subcellular actions and how bioactive lipids such as sphingosine and well-studied cholesterol are transported and metabolized throughout the cell; I combined the coumarin caging technology with a lysosome-targeting group that confers superior spatial-temporal control. Additionally, I employed the commercially available pacSph and pacChol, which due to their chemical modifications, allow the visualization of protein-lipid complexes and mapping of their interacting partners. We anticipate that this technology will lead to the achievement of higher sensitivity, especially for minimal occurrence interactions due to the lysosomal pre-localization of the probes.

### **2.1.1 Targeting the lysosome with a coumarin-cage approach**

In this work, I chose to use a coumarin-based approach as a cage for sphingosine and cholesterol. This group offers improvements over other caging groups such as nitrobenzyl-based systems, resulting in lower phototoxicity due to the use of longer wavelengths and avoiding the formation of aci-nitro intermediates<sup>189,190</sup>. Additionally, coumarin-caged molecules can also be detected under conventional fluorescent microscopes by the virtue of the cage which allows identifying labeled cells. Moreover, we decided to target the lysosome by known approaches, such as attaching activity-based probes, for instance, a known derivative of E-64, an epoxide protease inhibitor that can penetrate cells and allows pre-localization of molecules to the lysosomes<sup>191–195</sup>. This concept has been applied for tracking lysosome-dependent apoptosis, analysis of cathepsin cysteine proteases and therapeutic targets<sup>192,196,197</sup>. In addition, we envision a more simple, sophisticated linker, covalently attached to the coumarin-

cage core. This linker would consist of a N,N-dimethylamino group (commonly referred as a tertiary amine) which due to lysosomotropism, can be trapped selectively inside lysosomes by actions of its acidic environment. This concept has also been employed in commercially available dyes, such as LysoTracker and recently, used by Wagner et al., to synthesize the lysosome-targeting moiety of the 'click cage'<sup>152</sup>.

### 2.1.2 Synthesis and characterization of a lysosome-targeted sphingosine via an epoxysuccinic group

Firstly, we chose to target lysosomes by attaching an epoxysuccinyl scaffold, which has been extensively studied and reported as a natural inhibitor of cysteine proteases, which are to be found at the lysosome<sup>191,192,194,196</sup>. This small molecule is composed of three major groups: an electrophilic warhead that serves as a recognition group, and two cap groups (see figure 2.1). Modifications to the latter are used for tuning the specificity of these cysteine proteases inhibitors<sup>197</sup>.

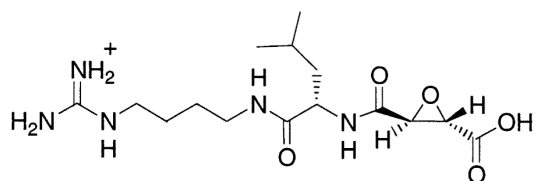


Fig. 2.1 Chemical structure of E-64. E-64 protease inhibitor via cysteine active sites.

Moreover, this technique has been previously reported as a system for cell-permeable organic fluorescent probes for lysosomes with excellent specificity<sup>198</sup>. This approach relies on the design and synthesis of a lysosome probe containing a cell-penetrating peptide, a recognition unit such as an epoxysuccinyl scaffold and a fluorescent dye.

Therefore, our design includes sphingosine and cholesterol as lipids of interest, a 'click cage'<sup>152</sup>, synthesized by the Nadler group in Dresden, as a caging group. An epoxysuccinyl scaffold, which will be employed as a lysosome-targeting group, an additional small amino-azido linker, and when combining the functionalities of these compounds by means of click chemistry will result in our lysosome-targeting probes.

I began with the synthesis of the epoxide-containing lysosome targeting group by using diethyl L-tartrate as starting material, according to Morit *et al.* In the first step of synthesis<sup>199</sup> (see figure 2.2), strong acids such as HBr convert the respective alcohol to its conjugated acid, being a good leaving group, which enables bromine substitution. After treatment with acetyl chloride, I obtained the desired halohydrin **1** with a 78% yield. Then, halohydrins can be converted easily into epoxides in a base reaction. In this case, the base deprotonates the alcohol to give an alkoxide intermediate which is nucleophilic, leading to the displacement of the halogen on the adjacent carbon, leading to compound **2** with a 74% yield. Next, carboxylic esters are hydrolyzed to the parent carboxylic acid and an alcohol, using minimal amounts of base via saponification leading to compound **3** with 89% yield. Next, I synthesized an azido-containing linker to enable conjugation to the epoxysuccinyl scaffold by an amide bond and later to the alkyne-cage ('click' cage) by the virtue of a click chemistry reaction. Replacement of  $\alpha$ -amino acid functionalities to give azides has been described widely<sup>200</sup>. Therefore, I used a commercially available N-Boc-ethylene bromide, by reacting with  $\text{NaN}_3$  which under mild conditions over long reaction times afforded compound **4** with a 53% yield. Lastly, deprotection under strongly acidic conditions, such as TFA, leads to the cleaving of the Boc group, to give rise to a free  $\text{NH}_2$  group. On the next step of the synthesis, peptide bonds were formed using the mixed carbonic anhydride method<sup>201</sup>. After activation, I added the amine, to form our peptide bond of interest. Obtaining compound **5** with an 83% yield.

The alkyne-bearing click-cage compound **6** was synthesized by the Nadler's group at the Max Planck Institute in Dresden following a well-established procedure by Cürten *et al.*<sup>202</sup> and was used without further purification. Then, I reacted the click cage with an excess of phosgene, leading to the formation of a chloroformate. This compound was used without further purification, since chloroformates under flash chromatography reactions can react into carboxylic acids. Efficient synthesis of carbamates has been extensively described, through the reaction of amines with chloroformates<sup>153,165,203,204</sup>. Here, I used the commercially available D-erythro-sphingosine to give rise to compound **7** with a 60% yield (see figure 2.2).

Next, I combined the functionalities of compounds **5** and **7** to give rise to **8** which was further purified by HPLC with a yield of 82% (see figure 2.2).

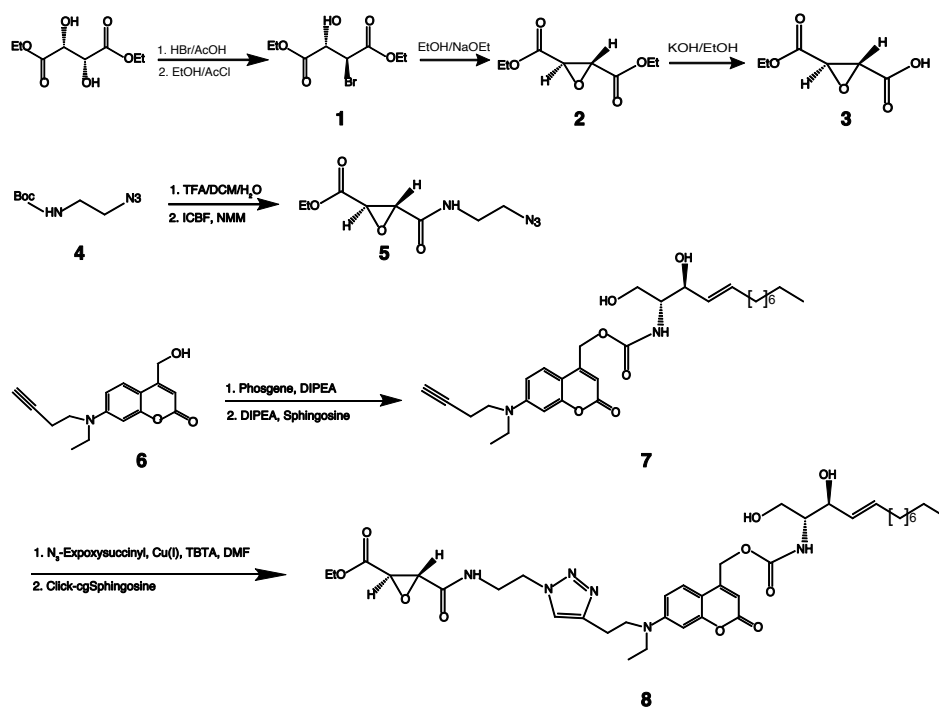


**Fig. 2.2** Chemical structures and synthetic procedure for a lysosome-targeted sphingosine probe.

After synthesis and confirmation by NMR of lysosome-targeted sphingosine, I sought to investigate the subcellular localization of this newly synthesized compound. Therefore, I incubated HeLa WT cells with concentrations of the probe ranging from 1 – 10  $\mu$ M and incubation times from 15 – 60 min (see figure 2.3).

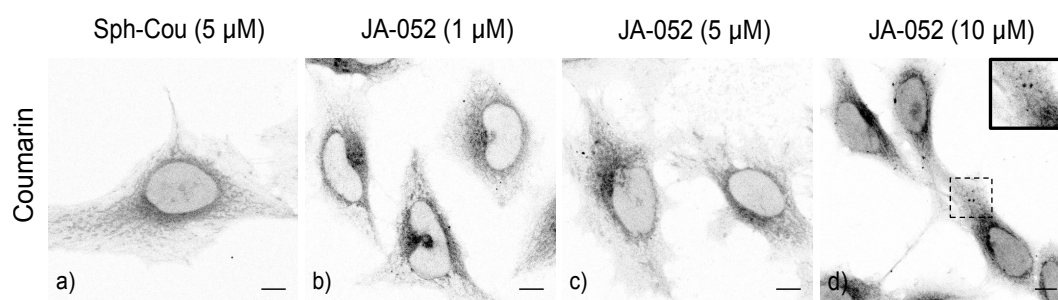


**Fig. 2.3** Subcellular localization of compound JA-052. Live HeLa cells were incubated with Sph-Cou and JA-052 for 30 min and imaged by confocal microscopy. **a)** Sph-Cou 5 $\mu$ M which has been reported as a globally distributed caged sphingosine **b)** JA-052 1 $\mu$ M **c)** JA-052 5 $\mu$ M **d)** JA-052 10  $\mu$ M. Scale bars represent 10  $\mu$ m.

As seen from Figure 2.3, after 30 min incubation the subcellular localization of JA-052 was found all over the cell, mostly at the ER and some small vesicles when increasing

the concentration of the probe. Next, I investigated if longer chasing times would result in lysosomal accumulation.

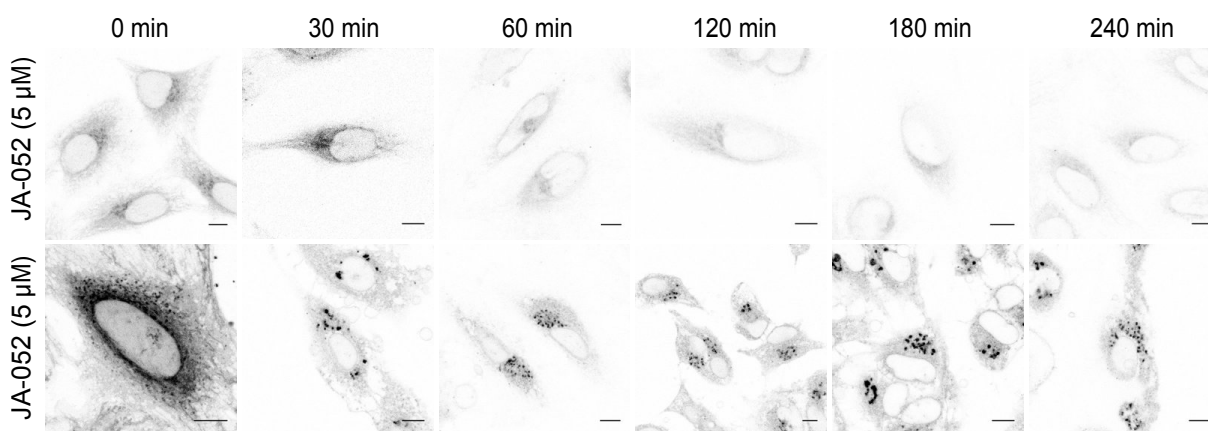


**Fig. 2.4** Time-chase localization of compound JA-052. Live HeLa cells were incubated with JA-052 1  $\mu$ M or 5  $\mu$ M and chased up to 240 minutes. Scale bars represent 10  $\mu$ m.

Unfortunately, longer incubation times of up to 4 h did not result in lysosomal co-localization as assessed by confocal microscopy (see figure 2.4). One could hypothesize that this lack of co-localization could be attributed to the large size of the final compound, where the epoxysuccinyl scaffold does not have enough driving potential to selectively accumulate inside lysosomes. In addition, the long chain of Sph, whose hydrophobic nature could drive interaction with internal membranes, as it has been reported for other caged lipids, which accumulate more in ER and Golgi compartments<sup>151,153,205</sup>. However, the exact mechanism of this effect remains unknown.

### 2.1.3 Synthesis via a tertiary amine-modified coumarin cage

To circumvent the mislocalization problems, I proposed the design and synthesis of a new lysosome targeting coumarin cage, which contains a tertiary amine as a lysosomal targeting group, covalently attached to the coumarin cage core. This basic moiety can be selectively concentrated in acidic organelles upon protonation due to their low luminal pH (4.5-5.0). The localization mechanism is similar to the way that commercially available tracking compounds enter the lysosome, e.g., LysoTracker<sup>®</sup>. The synthetic route of the lysosome-targeted cage coumarin (Lyso-Cou) was adapted from a previously reported caging group reported by Feng *et al.*<sup>187</sup> However, our design differs on the synthetic route and the targeting group, replacing a morpholino

group for a N,N-dimethylaminoethylene linker. Figure 2.5 shows the synthetic procedure used for obtaining Lyso-Cou. First, I started by synthesizing 7-ethylamino-4-hydroxymethylene coumarin acetate **9** according to literature<sup>152,202</sup>. Next, I obtained **10** by sequential S<sub>N</sub>2 alkylation using an excess of *tert*-Butyl bromoacetate. Sequential deprotection under acidic conditions removes the Boc protecting group from **10** to uncover a carboxylic group. Peptide bond formation of **11** was achieved by the mixed-anhydride method. Lastly, under basic conditions, I deacetylated **11** to yield our desired “Lysosome-Targeted Coumarin” (Lyso-Cou) **12** with 85% yield.

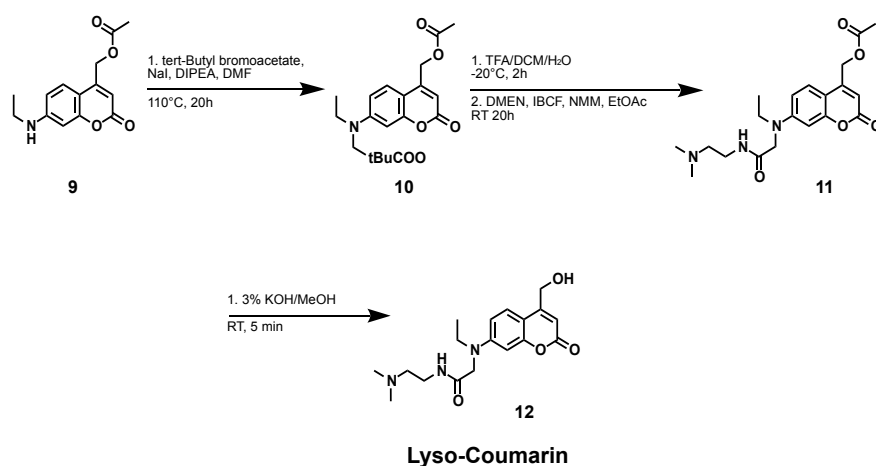


**Fig. 2.5** Synthesis of a lysosome-targeted coumarin cage. Synthetic route for obtaining Lyso-Cou cage.

After obtaining the Lyso-Cou cage, next I investigated coupling reactions to cage sphingosine and cholesterol.

### 2.1.4 Troubleshooting and synthesis of lysosome-targeted sphingosine, cholesterol, pacSph and pacChol

I chose to link pacSph and pacChol to the Lyso-Cou cage group by a carbamate and carbonate linker, respectively. The synthetic procedures for achieving the caging of Sph and Chol analogues have been previously described<sup>151,153,164,206</sup>. The sphingosine headgroup presents three functional groups, which serve as recognition sites for the machinery of the cell. Cholesterol, on the other hand, contains one hydroxyl group which serves as an esterification site for conversion into cholesteryl esters. Therefore, these sites are crucial to protect these lipids from any intracellular activity. From a synthetic point of view, caging of Sph and Chol should be straightforward. Lyso-Cou

contains a free hydroxyl group which could potentially be converted into a chloroformate, as previously reported<sup>153</sup>. Due to the difficulty of synthesis of pacSph and pacChol, first synthesis trials were done with endogenous Sph and Chol.

In order to activate the coumarin cage, the use of compounds such as phosgene, di- or tri-phosgene should allow rapid conversion to its chloroformate form. However, several attempts to activate the coumarin cage yielded byproducts due to a nucleophilic attack of the Cl<sup>-</sup> as a byproduct from the reaction, therefore subsequent halide alkylation can occur<sup>207</sup> (summarized in Table 2.1).

Activation reagent	Byproduct	Success of Cou	Sph	Chol
Phosgene	Alkyl chloride	Yes, very low yield	No	No
Diphosgene	Alkyl chloride	No	No	Yes
Triphosgene	Alkyl chloride	No	No	No
Bis-4-nitrophenyl carbonate	No	Yes	Yes	No
p-nitrophenyl carbonate	No	Yes	Yes	No
Bis-hydroxysuccinimidyl carbonate	No	Yes	Yes	No

**Table 2.1** Compounds used in this study for caging of cholesterol and sphingosine. Sphingosine can be caged by activating Lyso-Cou using carbonate intermediate compounds, while cage cholesterol can be obtained from the activation of cholesterol and then reacted with Lyso-Cou

It is important to highlight that these intermediate compounds could not be purified due to cleavage of the carbonate bond. After optimizing the intermediate compound for caging, I proceeded to synthesize a lysosome-targeted sphingosine on a one-pot reaction. Leading to compound **13** with a 73% yield (see figure 2.6).

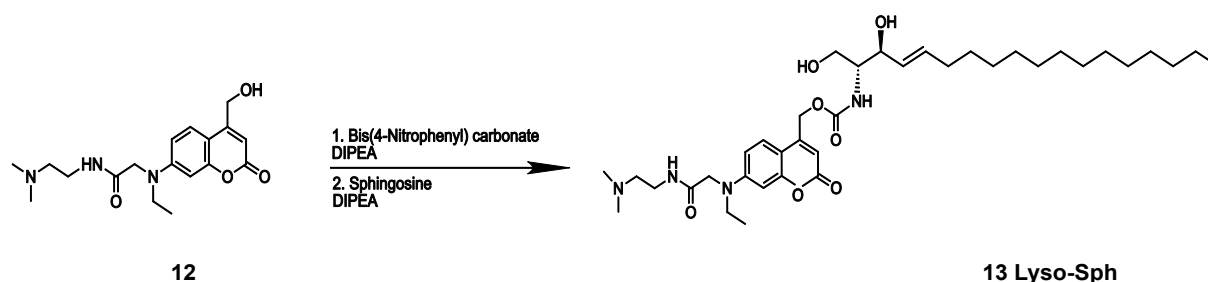


**Fig. 2.6** Chemical structure and synthesis procedure for Lyso-Sph. Synthesis of Lyso-Sph can be achieved by formation of a carbamate bond between a Lyso-caged protected with 4-NPC and the free amine group of Sph.

Of note, silica purification of such compounds, particularly bearing multiple amine groups can be time and solvent-consuming. It is well known that weakly amines can interact with the acidity of the silica gel, where solvent systems up to 60% MeOH yielded impure fractions. Therefore, the use of additives such as H<sub>2</sub>O and NH<sub>3</sub>(*aqueous*) are advantageous and lead to the successful purification of such compounds. After the synthesis of compound **13 (Lyso-Sph)**, I sought to synthesize a lysosome-targeted cholesterol probe. However, here the previously used strategy (activation using Bis-4-NPC) did not yield a caged cholesterol probe. The presence of an -OH group provides a good site for ionization. However, due to the high pK<sub>a</sub> of cholesterol = 18<sup>208</sup>, a nucleophilic attack cannot take place under these conditions, turning the cleavage site into a bad leaving group. Therefore, I investigated conditions in which cholesterol could be activated. Therefore, I used phosgene, di-phosgene, and tri-phosgene. Where di-phosgene yielded the best result. (see figure 2.7, A)

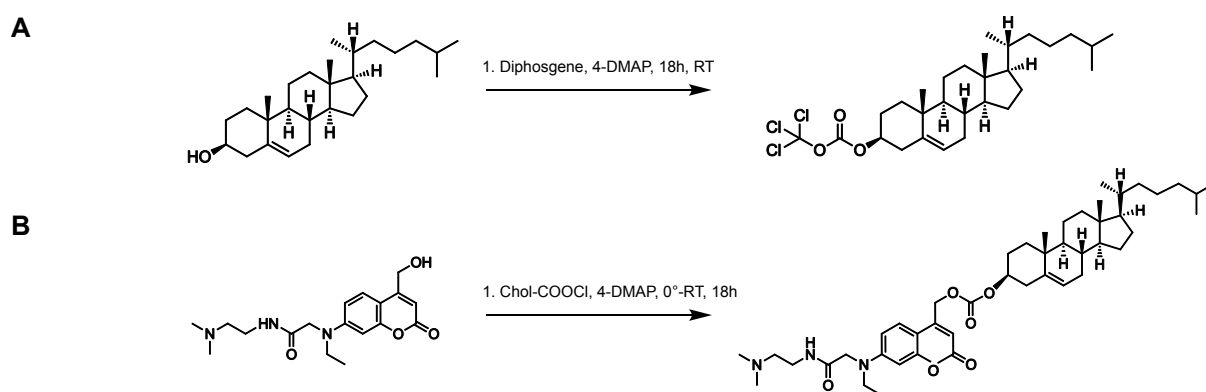


**Fig. 2.7** Synthetic route for caged cholesterol. Phosgenation of cholesterol allows the formation of a carbonate bond between cholesterol and the coumarin cage

Next, I synthesized a lysosome-targeted cholesterol probe, through the reaction of the chloroformate and alcohol group under basic conditions to afford compound **14** with an 83% yield (see figure 2.7, B)

Synthesis of pacSph and pacChol requires long synthetic procedures, which often require specialized techniques and consequential low yields. To date, pacSph and pacChol are commercially available. Therefore, I obtained these lipids from a commercially available source, which were used without further purification for the next reactions. Next, I synthesized lysosome-targeted pacChol (Lyso-pacChol). Synthesis of such probe was achieved by activating pacChol with di-phosgene, after obtaining

the corresponding chloroformate, I reacted the crude product with Lyso-Cou, under basic conditions, which allowed the formation of the corresponding carbonate bond. Yielding Lyso-pacChol with a 96% yield (see figure 2.8).

Synthesis of Lyso-pacSph was performed by Judith Notbohm (a master student in our lab). The synthetic route for obtaining this probe is as follows; first, activation of the coumarin cage with 4-NPC, this forms a carbonate intermediate compound, which then on a one-pot reaction with an excess of a base such as DIPEA, allows displacement of the nitrophenyl group, via a nucleophilic attack from the amine group from pacSph. This coupling step led to Lyso-pacSph with a 99% yield.

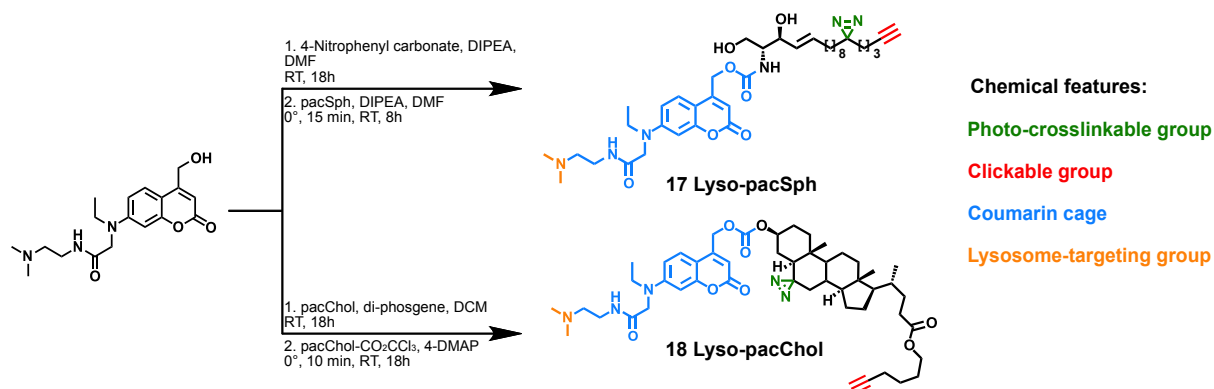


**Fig. 2.8** Chemical structure and synthesis of Lyso-pacSph and Lyso-pacChol

## 2.2 Characterization of Lyso-pacSph and Lyso-pacChol

After synthesis, I investigated the localization of the newly synthesized probes via live-cell confocal microscopy by virtue of the coumarin cage fluorescence. Firstly, I incubated HeLa WT cells with Lyso-pacSph and Lyso-pacChol in concentrations ranging from 750 nM to 10  $\mu$ M for 1 hour (pulse) and an initial chase of 60 minutes (see figure 2.9, A). Initial experiments revealed that the probe is taken up by the cells rapidly even at low concentrations and without the need for detergent or complex incubation techniques. Interestingly, Lyso-pacChol uptake resulted in immediate vesicular staining, whereas Lyso-pacSph showed more diffuse intracellular staining. To overcome this issue, I varied chasing times from 0 min – 18h (see figure. 2.9, B) and found that Lyso-pacSph requires more than 4 hours for optimal colocalization.

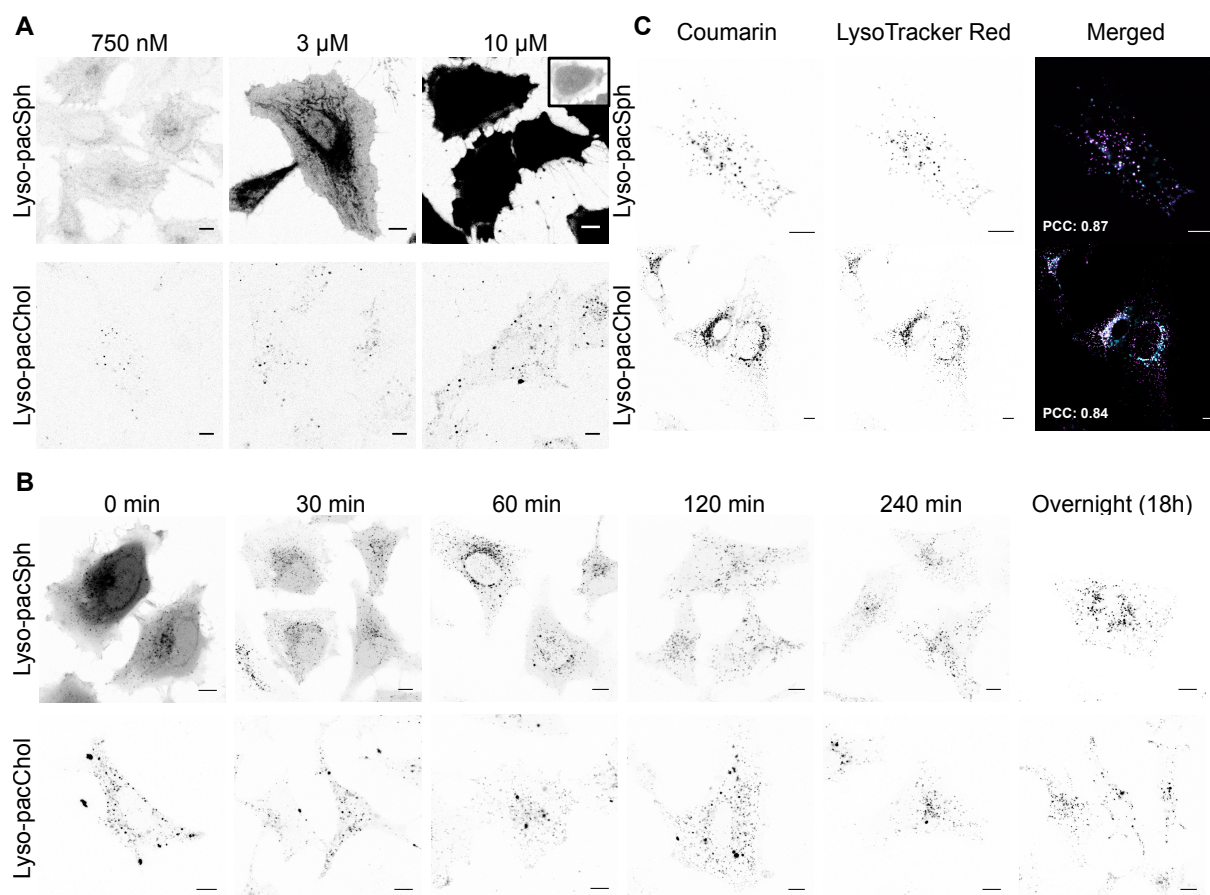


**Fig. 2.9** Confocal microscopy of Lyso-pacSph and Lyso-pacChol. A) Concentration-dependent internalization of the probe. B) Time-course of Lyso-pacSph and Lyso-pacChol. Cells were treated with 10 μM of Lyso-pacSph or Lyso-pacChol and images were acquired at indicated timepoints. C) Colocalization of the lyso-probes with LysoTracker with optimized conditions. Scale bars represent 10 μm.

Based on these results, I treated HeLa cells with 10 μM lyso-pacSph or lyso-pacChol for 60 and 45 minutes, respectively and chased overnight. The fluorescent pattern of the lyso-probes overlaps completely with the LysoTracker signal as confirmed using Pearson's correlation coefficient (PCC) with values of 0.84 or higher (Fig 2.9, C) demonstrating that Lyso-pacSph and Lyso-pacChol are indeed pre-localized to lysosomes. This wide window of suitable conditions allowed us to use different labelling conditions for microscopy, mass spectrometry (MS) and thin-layer chromatography (TLC) experiments.

Next, I evaluated the photo-cleavage ('uncaging') efficiency of the lyso-probes. Therefore, I performed uncaging experiments in an aqueous solution with increasing times of UV irradiation (405 nm), subsequent lipid extraction according to an established protocol from Höglinger et al.<sup>153</sup>, click with a commercially available 3-

azido-7-hydroxycoumarin, and visualization by TLC (see figure 2.10, A and B). After quantification, all experiments showed that 60s irradiation at 405 nm are sufficient to uncage lyso-pacChol. However, experiments in a cellular context (not shown here) indicate the need for longer exposure UV times. This could be attributed to the interference of cellular surroundings and light penetration. Therefore, I carried out all further experiments with 90s UV irradiation. Interestingly, another observation was the decrease in the efficiency of the click reaction when exposing the lipid more than 90-100s to UV light (see pink curve in figure 2.10, C). A possibility is that the triple bond is hydrogenated in the aqueous solution after prolonged UV irradiation<sup>209,210</sup>. However, this effect was not further investigated.

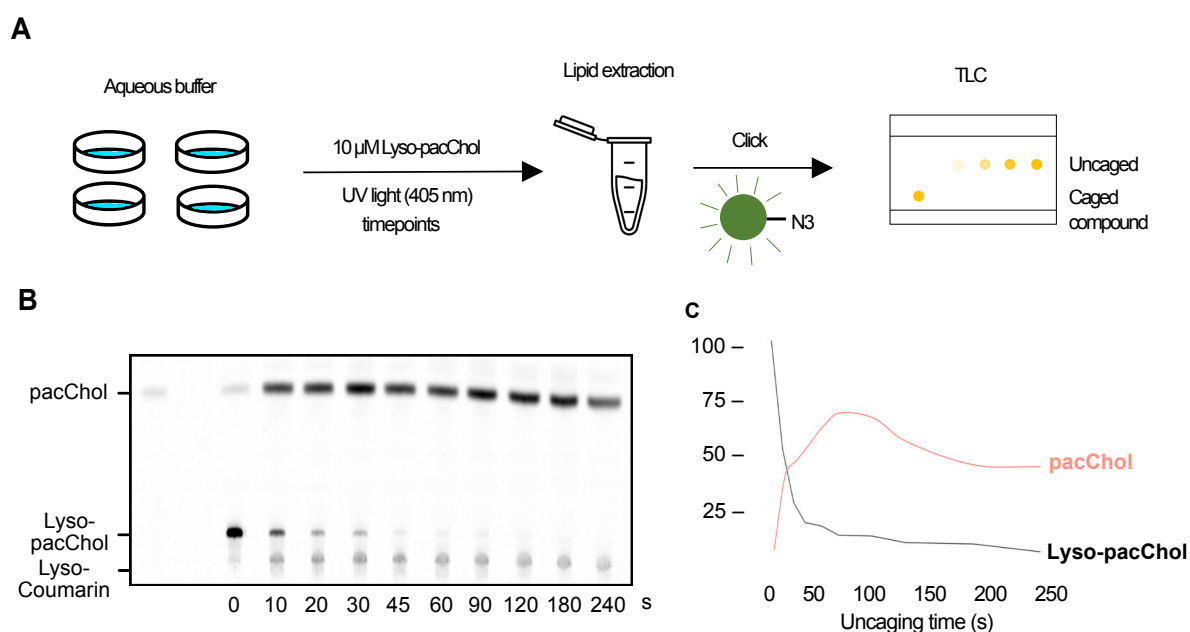


**Fig. 2.10** Uncaging efficiency of Lyso-pacChol A) Schematic representation of uncaging. B) TLC of caged/uncaged probes at different timepoints. C) Uncaging efficiency of Lyso-pacChol and quantification of the Copper Alkyne-Azide cycloaddition (CuAAC) reaction. The background was subtracted using Fiji software.

Lysosomes are organelles enriched with a variety of lipases, esterases among other degradation enzymes; therefore, it was crucial to assess the probe stability. To this end, I pulsed HeLa WT cells with 10  $\mu$ M Lyso-pacSph or Lyso-pacChol and chased them up to 24 hours. Next, I collected the cells at indicated time points, and visualized the probes by TLC. Figure 2.11 shows no additional bands even up to a 24-hour incubation time. This indicates that both probes are stable in their caged form under

the acidic conditions of the lysosome and that remaining functional groups from pacChol and pacSph did not undergo any further modification.

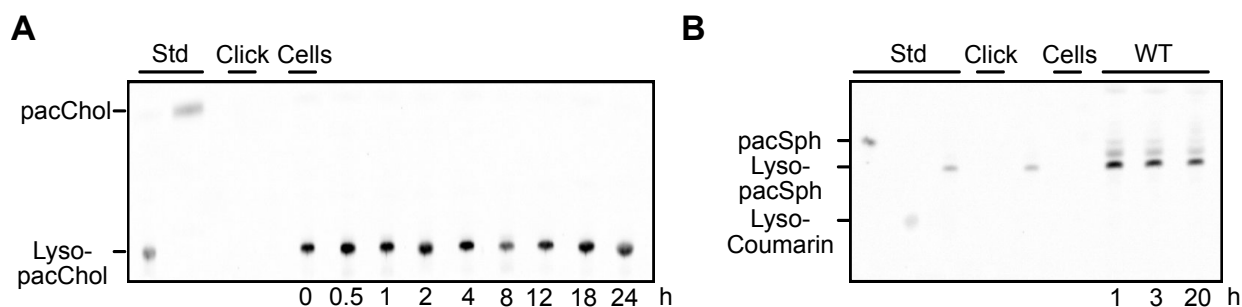


**Fig. 2.11** Time dependent stability of lyso-pacChol and lyso-pacSph in cells. TLC analysis of lipid extracts of HeLa cells incubated with 10  $\mu$ M Lyso-pacChol and Lyso-pacSph and chased up to 24 hours (- UV treatment). The background was subtracted using Fiji software.

In a second step, I UV-irradiated cells, chased for 24-hours as determined in the previous experiment and allowed a second incubation time ('chase'), before subjecting them to TLC analysis. In this way, I could visualize free sphingosine, cholesterol, and their incorporation into their respective metabolic pathways (see figure 2.12, A and B) as indicated by the appearance of Cer, PC, SM and Chol-Ester metabolites. This is in accordance with previous studies using tri-functional sphingosine<sup>153</sup> and bi-functional cholesterol<sup>57,85</sup>. (see Appendix for metabolite identification)

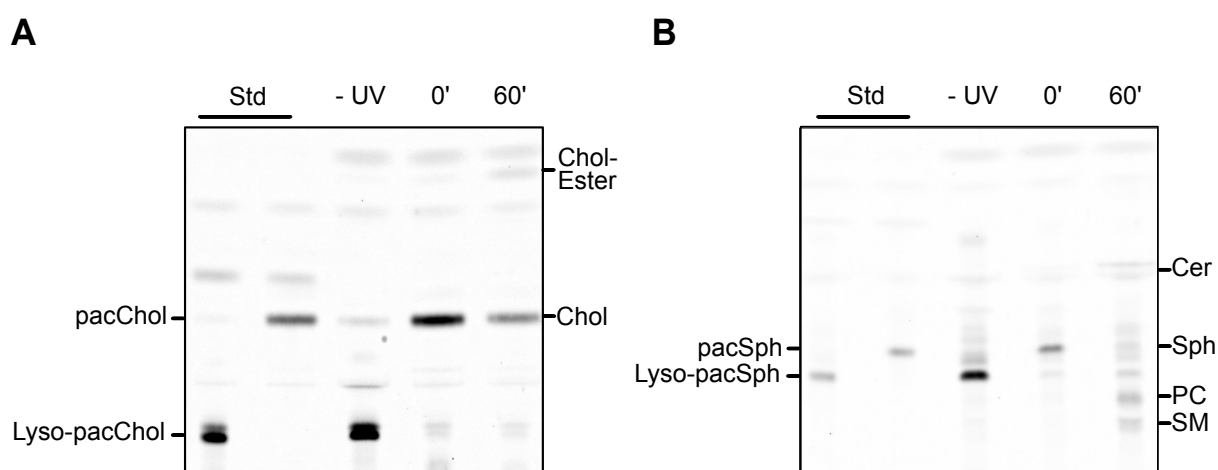


**Fig. 2.12** Stability and metabolic availability of lyso-pacChol and Lyso-pacSph in cells. TLC analysis of lipid extracts of HeLa cells incubated with 10  $\mu$ M Lyso-pacChol and Lyso-pacSph, uncaged, collected immediately, or chased for additional 60 minutes. The migration behaviour of pac-modified ceramide (Cer), sphingomyelin (SM) and phosphatidylcholine (PC) was determined by comparison with available standards. The background was subtracted using Fiji software.

Next, I sought to investigate the uptake of Lyso-pacChol and Lyso-pacSph compared to the non-caged pacChol and pacSph. Therefore, I pulsed HeLa WT cells with the conditions determined above (see figure 2.13). Next, I extracted the lipids, clicked them (samples with pacChol and pacSph only), and investigated them by TLC plate. The concentration of the pacChol and pacSph was determined by extracting and sum of the raw intensity density of all coumarin-labeled metabolites in Fiji. Then, these values were compared to a standard curve ranging from 10 to 100 pmol. This way, the intracellular concentration of Lyso-pacChol was estimated to be 0,92 fmol/cell compared to 1,92 fmol/ cell of pacChol and 0,36 fmol/cell for Lyso-pacSph compared to 0.54 fmol/ cell for pacSph in HeLa WT by Thin-layer chromatography (TLC). These differences in concentration could be allocated to the spatial distribution and how are the probes internalized by the cell. First, pacChol and pacSph are distributed in a whole-cell manner, whereas the lyso-probes only accumulate in the small volume of lysosomes. Additionally, some chemical groups, such as the coumarin cage, could potentially diminish cellular uptake due to an increase in the molecular weight of the molecule<sup>211–213</sup>.

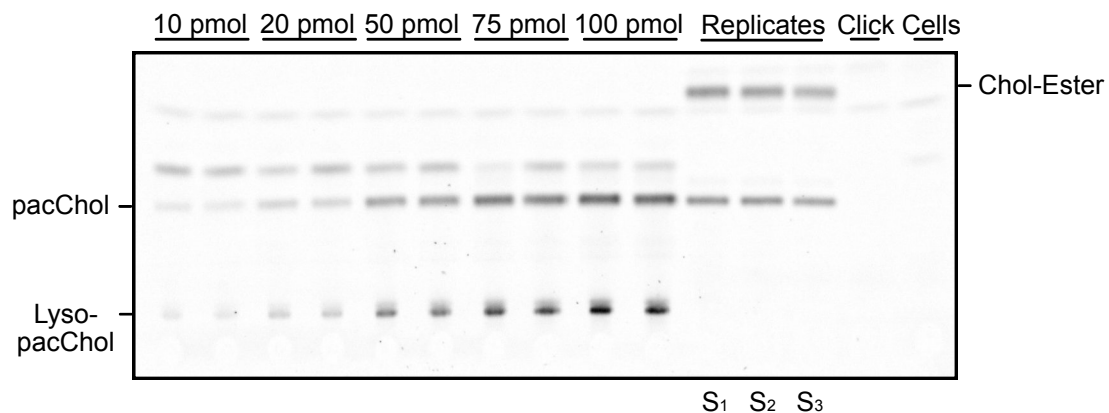


**Fig. 2.13** Example of quantification of pacChol cellular uptake by TLC. HeLa cells were pulsed with 5 $\mu$ M pacChol for 30 minutes, collected, lipids extracted, clicked, and spotted on a TLC plate. Curve standard was done by diluting 10 mM stock of pacChol and Lyso-pacChol to the desired concentration. Raw intensity densities were extracted using Fiji software.

A previously described caged form of Sph (Sph-Cou) was employed in calcium-related studies. Höglinger et al. found that a sudden release of Sph triggers calcium release from acidic stores through the action of the two-pore channel 1 (TPC1), leading to the translocation of the autophagy-relevant transcription factor EB (TFEB) to the nucleus after calcium release<sup>165</sup>. In order to check whether the diazirine and alkyne

modification impacted signaling outcomes of Sph, I investigated if I could visualize an increase of intracellular calcium after uncaging of Lyso-pacSph. As a control, I used Lyso-pacChol, where no such effect is expected.

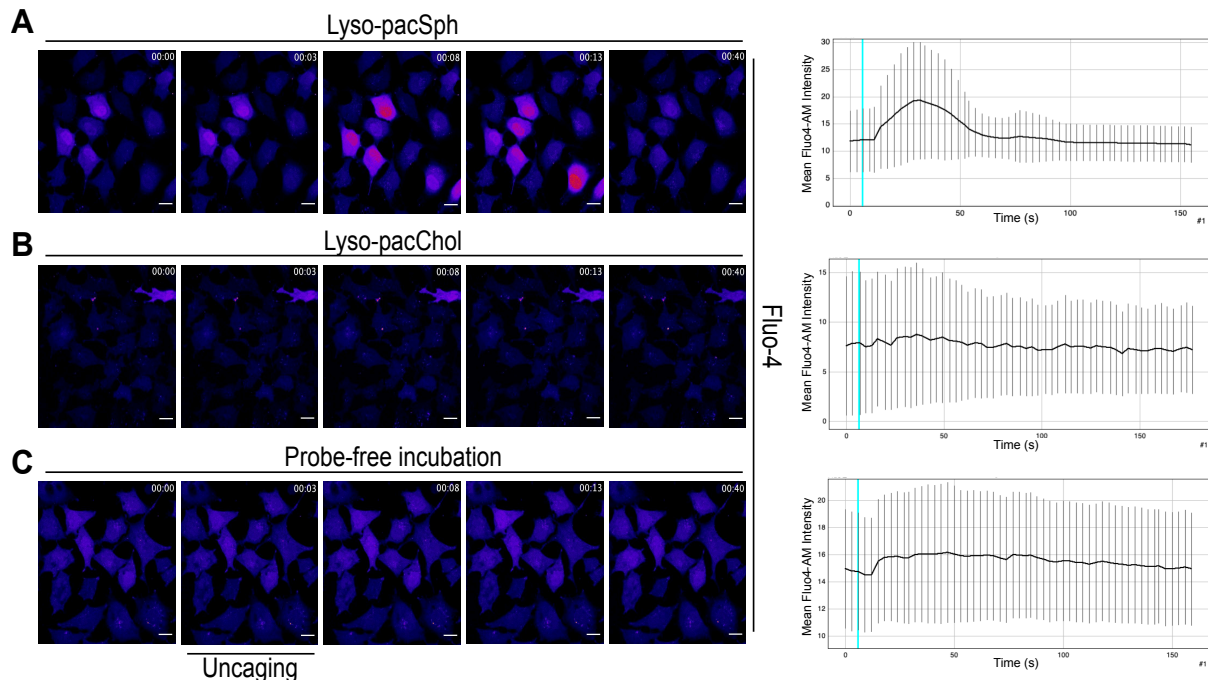


**Fig. 2.14** Lysosomal uncaging of lyso-probes and their effect in intracellular  $\text{Ca}^{2+}$  A, B and C) Time-lapse microscopy images and mean of Fluo-4 AM fluorescence of HeLa cells treated with 10  $\mu\text{M}$  Lyso-pacSph (A)  $n=13$ , 10  $\mu\text{M}$  Lyso-pacChol  $n=12$  (B) and untreated (probe-free) cells  $n=18$ . Scale bars represent 10  $\mu\text{m}$ .

To this end, I incubated HeLa cells with Lyso-pacSph or Lyso-pacChol, labeled cells with the calcium indicator Fluo-4 AM and acquired time-lapse images before and after the uncaging event (using a 385 nm LED for 5s). Reassuringly, cells with lyso-pacSph responded immediately (2 – 6 s) and released  $\text{Ca}^{2+}$  from lysosomes into the cytoplasm as seen from an increase in fluorescence (see figure 2.14, A). On the other hand, confocal microscopy experiments with lyso-pacChol failed to enhance the fluorescence of Fluo-4 AM, as in cells without probe treatment (see quantification in figure 2.14, B and C)

Together, these data show the versatility of the lyso-probes. I demonstrate that they are powerful tools, which are cell-permeable, stable in the intracellular environment, ready to be incorporated into their metabolic pathways upon uncaging, and that their remaining modifications do not impact their biological properties as demonstrated with respect to  $\text{Ca}^{2+}$  signaling.

## **2.3 Lysosome-targeted sphingosine and cholesterol are novel tools to study lipid transport and metabolism in cellular disease models**

Previous studies employing bi-functional lipids or fluorescent analogs have shed light on sterol/sphingolipid metabolism and trafficking in health and disease<sup>122,126,148–150,156,214–217</sup>. However, a more detailed snapshot of transport across organelles has not been possible until yet. Therefore, the lysosomal trafficking of these lipid species has been poorly described and which organelle membrane serves as the initial acceptor has not been fully determined. Due to the versatility of the clickable group, I envisioned that one application of the lyso-probes is to study their trafficking via cell fixation and subsequent staining by click reaction with an azide-bearing fluorophore for visualization by confocal microscopy. In a first step, I aimed to optimize the protocol, especially with regards to fixation conditions. Previous protocols for visualization of crosslinked lipids included harsh conditions (MeOH fixation, chloroform washes) which did not allow for the visualization of plasma membrane or lipid droplets as these organelles were mostly washed away. However, a faithful visualization of lipid droplets is especially important when investigating cholesterol trafficking. Therefore, I sought to investigate new fixation conditions which will allow us to visualize such organelles, while retaining the specificity by not staining non-crosslinked lipids. As seen from Figure 2.15 (A), fixation protocol with MeOH/CHCl<sub>3</sub> gave rise to a strong staining in the lipid channel. However, structures such as LD were washed away. This effect can be attributed to the hydrophobic nature of such organelles, surrounded by a phospholipid monolayer with few accessory proteins, which causes such organelles to not be retained using such harsh conditions. A protocol including fixation with 4% PFA (see figure 2.15, B and C) yielded better results when staining for LD. However, washing steps with glycine reduced the signal intensity of the clicked lipid. Whereas an overnight wash with 2% BSA retained all LD (see figure 2.15, B). As control, to corroborate that our cholesterol probe is being cross-linked efficiently and that the method is suitable and not creating artifacts, I performed a negative control in the absence of UV irradiation, where we can observe that LD are still conserved without any traces of lyso-pacChol staining. (see figure 2.15, D)

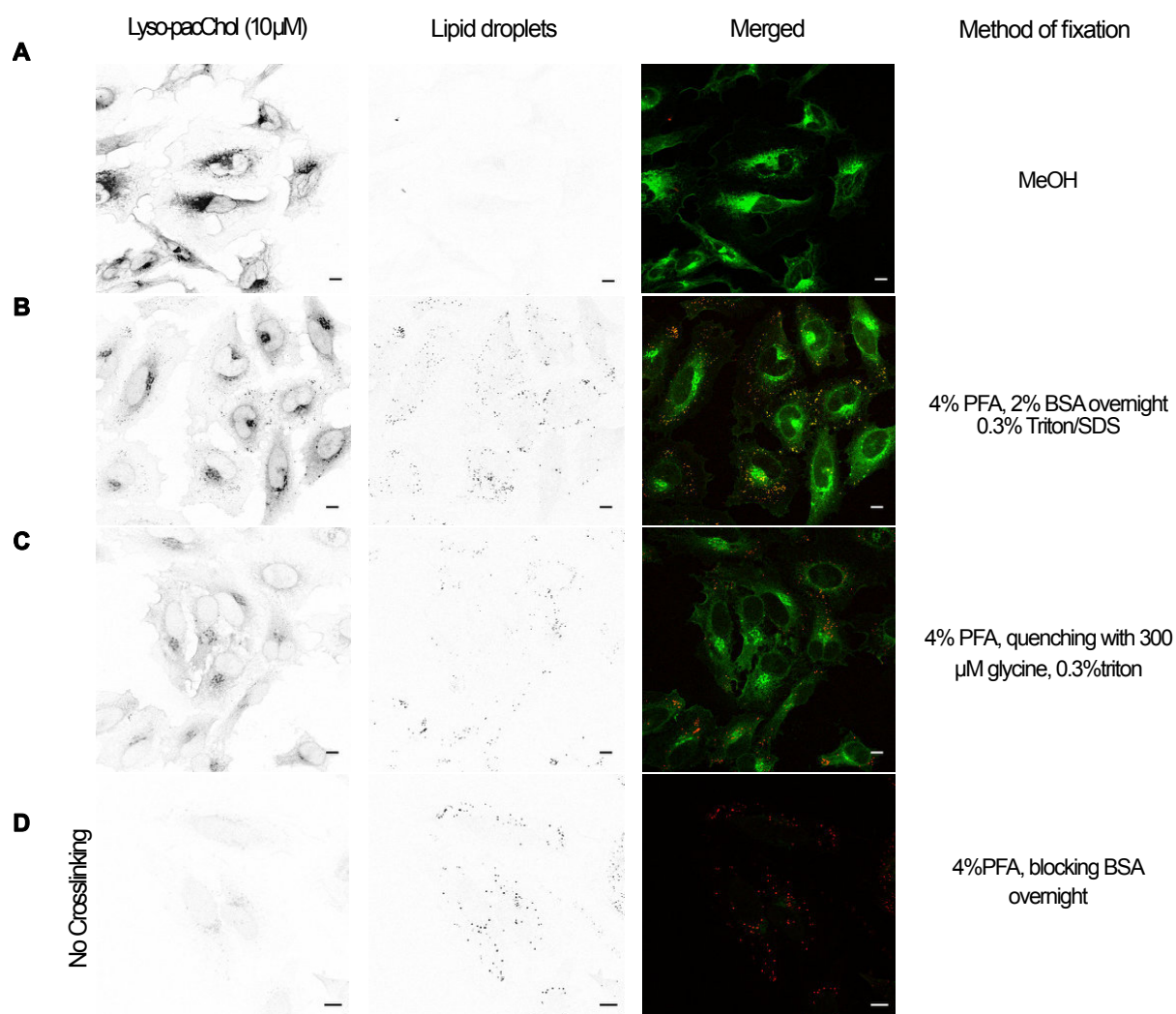


**Fig. 2.15** Optimization of a fixation method for Lyso-pacChol. Confocal images of N3-Alexa488-labelled Lyso-pacChol cells. HeLa cells were treated with 10  $\mu$ M of Lyso-pacChol and subjected to distinct fixation methods. A) MeOH/ $\text{CHCl}_3$  B) 4% PFA fixation, solubilization with 0.3% SDS/Triton and blocking with 2% BSA overnight C) 4% PFA fixation and quenching with 300  $\mu$ M glycine and 0.3% Triton. D) No crosslinking (protein-lipid complexes shouldn't be visualized). Scale bars represent 10  $\mu$ m.

Therefore, I concluded that our new method still allows the sensitive detection of cross-linked lipids, while at the same time preserving cellular organelles with high lipid content such as lipid droplets. Unfortunately, the chosen fixation method (PFA fixation with 0.3% SDS/Triton solubilization) could not be applied as well for experiments using Lyso-pacSph, which resulted in the absence of lipid signal from the click lipids. Therefore, all experiments for Sph were performed with MeOH/ $\text{CHCl}_3$  fixation.

After optimization of our fixation method, I went into investigating the subcellular transport route of lyso-pacChol and lyso-pacSph in WT cells and models of lysosomal storage diseases available in our lab. (see table 2.1).

Cell line	Gene	Source	Reference
HeLa WT	-	Annaert lab	Tharkeshwar <i>et al.</i> <sup>83</sup>
HeLa NPC1 <sup>-/-</sup>	Niemann-Pick type C	Annaert lab	Tharkeshwar <i>et al.</i> <sup>83</sup>
HeLa SGPL1 <sup>-/-</sup>	Sphingosine-1-phosphate lyase	Brügger lab	Gerl <i>et al.</i> <sup>83</sup>
HeLa SK1 <sup>-/-</sup> / SK2 <sup>-/-</sup>	Sphingosine kinase 1 and 2	Spiegel lab	This study (not published)

**Table 2.2** Cell lines employed in this thesis chapter.

Initially, I identified the time-dependent export of cholesterol from lysosomes in WT cells. Pulse-chase experiments, as seen from Figure 2.18 revealed complete clearance of lysosomal cholesterol after 30 minutes, trafficking to organelles such as the ER, Golgi and PM as soon as 15 minutes and staining of other organelles, such as LD after 60 minutes chase (see figure 2.16, A). To quantify the kinetics of lysosomal cholesterol exit, I performed co-localization analysis of the lyso-pacChol signal and the LAMP1 channel (see figure 2.16 B).

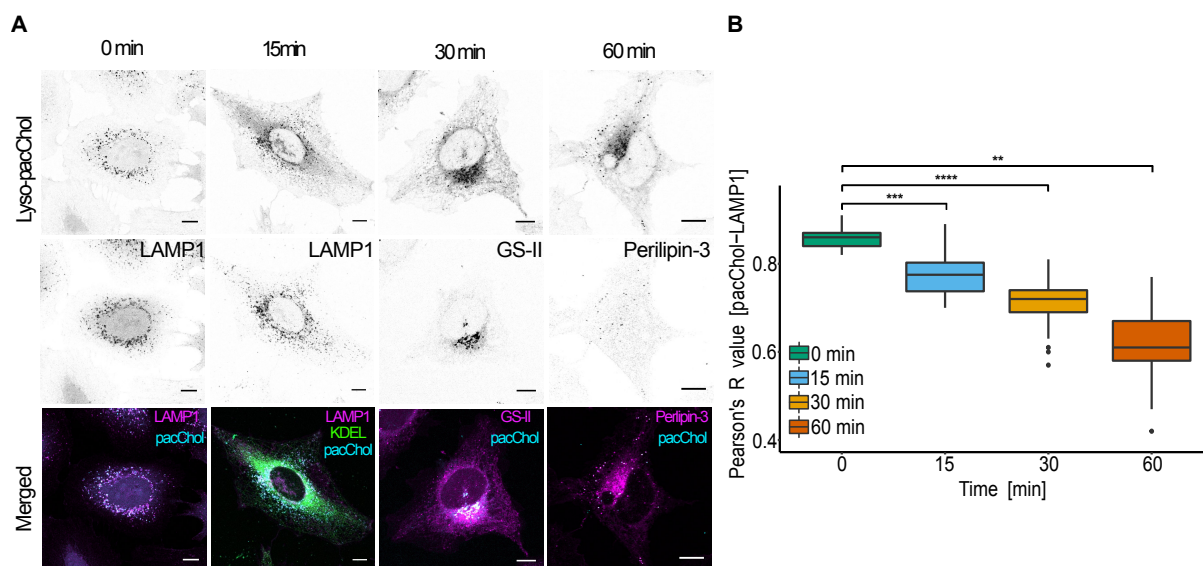


**Fig. 2.16** Visualization of time-dependent subcellular localization of Lyso-pacChol in WT cells. A) Confocal microscopy of N3-Alexa488-labelled Lyso-pacChol fixed cells. HeLa cells were pulsed with 10  $\mu$ M of Lyso-pacChol for 45 minutes and chased overnight. Next, uncaged (UV-irradiated) and crosslinked immediately or left to a second chase for indicated times. After cell fixation, cells were subjected to click reaction and IF. B) Quantification of lysosomal lipid egress. Pearson's R value of non-thresholded images from lipid channel vs. LAMP1

immunofluorescence, calculated for each time point ( $n \geq 48$ ) using the Coloc 2 feature from Fiji. (ns P-value  $> 0.5$  \* $P \leq 0.05$  \*\* $P$ -value  $\leq 0.01$  \*\*\* $P$ -value  $\leq 0.001$  \*\*\*\* $P$ -value  $\leq 0.0001$ ). Scale bars represent  $10 \mu\text{m}$ .

Here, a significant decrease in the Pearson's correlation coefficient from 0.83 to 0.62 over the time-course confirmed the redistribution of the cholesterol signal towards other organelles. Overall, this new setup has allowed us to visualize cholesterol at a subcellular level, re-assuring that the actions of lyso-pacChol upon uncaging mimic their natural counterparts.

Next, I went into visualizing the export of cholesterol in cellular disease models. For this, NPC1, SGPL1 and SK1/SK2  $-/-$  cells were used. These cell lines have been reported to have a lipid malfunction, either on transport (NPC1) or defective enzymatic reaction (SGPL1, SK1/SK2). After pulse-chase experiments, I could visualize that loss of NPC1, indeed leads to an accumulation of cholesterol as assessed by quantifying the amount of lipid signal to LAMP1 positive compartments. Moreover, SGPL1 or SK1/SK2 did not show hints of cholesterol accumulation with this method.

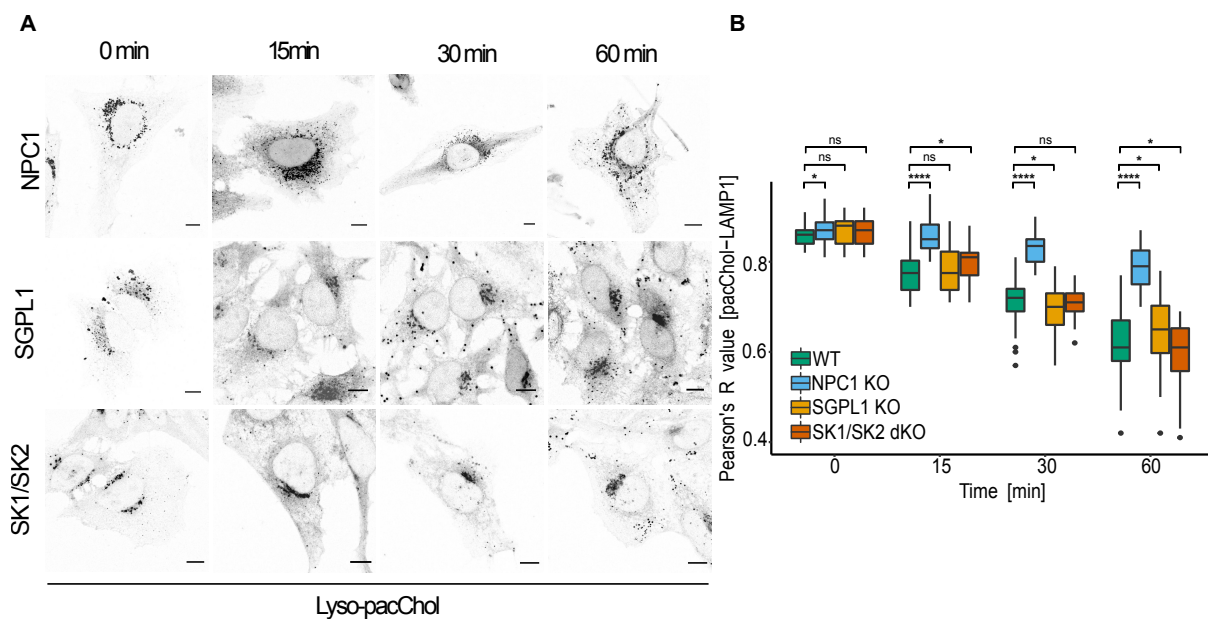


**Fig. 2.17** Time-dependent visualization of lysosomal export of cholesterol in cellular disease models. A) Confocal microscopy of N3-Alexa488-labelled lyso-pacChol fixed cells. Cells were pulsed with  $10 \mu\text{M}$  of Lyso-pacChol for 45 minutes and chased overnight. Next, uncaged (UV-irradiated) and crosslinked immediately or left to a second chase for indicated times. After cell fixation, cells were subjected to click reaction and IF. B) Quantification of lysosomal lipid egress. Pearson's R value of non-thresholded images from lipid channel vs. LAMP1 immunofluorescence, calculated for each time point ( $n \geq 48$ ) using the Coloc 2 feature from Fiji. (ns P-value  $> 0.5$  \* $P \leq 0.05$  \*\* $P$ -value  $\leq 0.01$  \*\*\* $P$ -value  $\leq 0.001$  \*\*\*\* $P$ -value  $\leq 0.0001$ ). Scale bars represent  $10 \mu\text{m}$ .

Interestingly, previous data from the Proia lab<sup>218</sup> showed that SGPL1 deletion resulted in an increased rate of conversion of cholesterol to cholesterol-esters. Specifically, disruption of *Sgpl1* gene resulted in elevated Chol and CE levels in serum and liver of mouse models<sup>218,219</sup>. This could point towards a faster transport of Chol, or towards more efficient esterification. With regards to transport kinetics, my experiments did not allow me to observe increased lysosomal export, given that WT cells showed very fast export of the lyso-pacChol. Although I did not observe cholesterol retention at LE/LY by confocal microscopy or by quantification of PCC, as reported by the Heringdorf lab<sup>219,220</sup>. I could visualize a perturbation in sterol homeostasis by deletion of the *sgpl1* gene, which led to the appearance of Chol-Esters (in form of LD) at earlier time points compared to WT, which agrees with previous studies done in yeast and mice<sup>218,221</sup>. This could be potentially explained by the increase of other lipid specie such as TAG, which were also found to be elevated in livers of *Sgpl1*<sup>-/-</sup> mice<sup>218</sup> and correlate to an increase in the formation of LD as a storage mechanism. Although lipidomics has shed light on this phenomenon, other techniques such as WB could also tell us if indeed the appearance of LD is attributed to this, by looking at the overexpression of known LD proteins such as PLIN-3.

Overall, I was able to time-resolve cholesterol trafficking in HeLa WT and disease models. These experiments also highlight the advantages of using Lyso-pacChol for investigating Chol metabolism: Primarily, this method allows to follow cholesterol from a very well-defined starting point and time. In comparison to other methods<sup>56,57,222</sup> such as complexation with BSA, delivery in LDL particles or via specific cyclodextrin carriers, such as methyl- $\beta$ -cyclodextrin, the temporal resolution is vastly improved.

Next, I sought to investigate the yet unexplored lysosomal transport of sphingosine. Similar to the cholesterol experiments, I sought to investigate the subcellular localization of Sph in a WT background. Towards this end, I pulsed HeLa cells with Lyso-pacSph and chased overnight. After uncaging and photoaffinity labeling, cells were fixed, clicked, and organelles were identified by IF using organellar markers. Figure 2.18 shows the route for sphingosine trafficking. I could observe that 15 minutes are sufficient for sphingosine to exit the lysosome. Moreover, other organelles such as the Golgi could be observed at later time points (see Figure 2.18, A, 30 and 60

minutes) which denotes further metabolism of Cer to SM and GlcCer, which is known to occur at the Golgi.

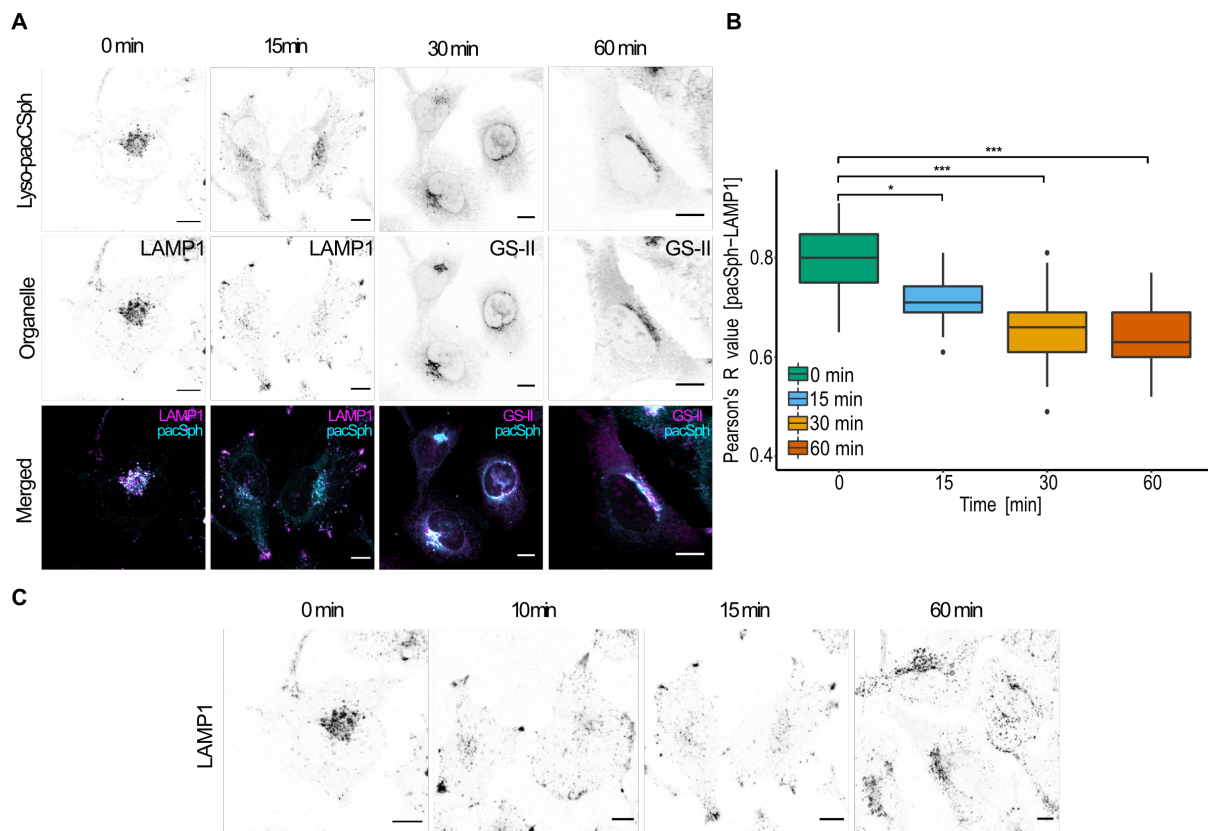


**Fig. 2.18** Visualization of time-dependent subcellular localization of Lyso-pacSph in WT cells. A) Confocal microscopy of N3-Alexa594-labelled lyso-pacSph fixed cells. HeLa cells were pulsed with 10  $\mu$ M of Lyso-pacSph for 60 minutes and chased overnight. Next, uncaged (UV-irradiated) and crosslinked immediately or left to a second chase for indicated times. After cell fixation, cells were subjected to click reaction and IF. B) Quantification of lysosomal lipid egress. Pearson's R value of non-thresholded images from lipid channel vs. LAMP1 immunofluorescence, calculated for each time point ( $n \geq 48$ ) using the Coloc 2 feature from Fiji. ( $ns$  P-value  $> 0.5$  \*P  $\leq 0.05$  \*\*P-value  $\leq 0.01$  \*\*\*P-value  $\leq 0.001$  \*\*\*\*P-value  $\leq 0.0001$ ). C) Relocalization of lysosomes towards the PM. Scale bars represent 10  $\mu$ m.

Interestingly, one observation I had was that photorelease of Sph caused lysosomes to be rearranged or relocalized towards the PM as seen from the LAMP1 pictures, where lysosomes at 0 minutes are localized more to the nuclear periphery and after uncaging and chasing between 10-15 minutes it can be observed that the signal from LAMP1 is localized more to the PM (see figure 2.18, C). It is reported that upon cytosolic calcium increase (which follows Lyso-pacSph uncaging, see figure 2.14), lysosomes fuse with the PM<sup>223,224</sup>. Therefore, a route such as exocytosis cannot be

ruled out, where the uncaged sphingosine is released into the extracellular space<sup>225</sup>. This could also explain the loss of Sph signal over time (data not shown).

Next, I employed NPC1, SGPL1 and SK1/SK2  $-/-$  cells and followed sphingosine transport. Strikingly, I found that Sph was retained in lysosomes during the entire time course in NPC1 and SK1/SK2  $-/-$  cells (see figure 2.19 A, B for quantification by Pearson's correlation coefficient). The role of NPC1 disease has been highly debated for many years. For example, a study from the Ikonen lab<sup>226</sup> showed that Sph is not stored in NPC1  $-/-$  cells. However, this study is hindered by the spatial and temporal resolution, given that radiolabeled analogues of SM, Cer and Sph were fed to cells as LDL particles. In these settings, experimental readouts did not show elevated levels or storage of Sph at all. This could be explained by the hour-long chasing times, in which the lipid species were recognized, metabolized and incorporated into their metabolic pathway. In contrast, studies using bifunctional or trifunctional Sph analogues have already found that lysosomal Sph export is delayed in NPC1<sup>148,153</sup>. Similarly, my findings present evidence of Sph storage in NPC1 KO cells.

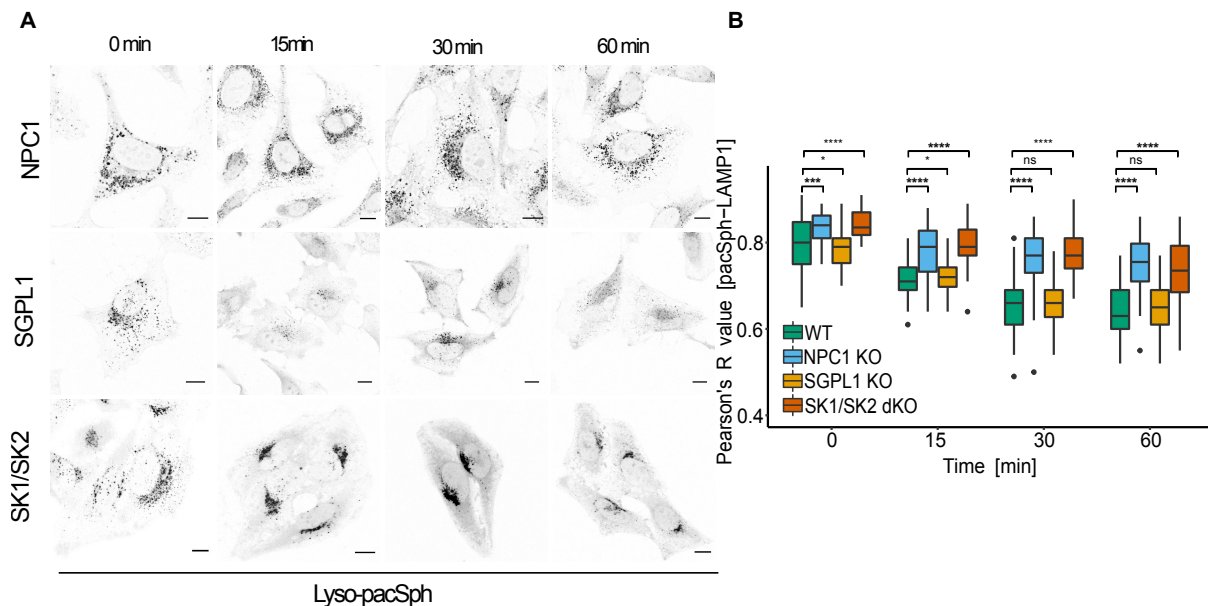


**Fig. 2.19** Time-dependent visualization of lysosomal export of sphingosine in cellular disease models. A) Confocal microscopy of fixed HeLa cells. Cells were pulsed with 10  $\mu$ M of Lyso-pacSph for 60 minutes and chased overnight. Next, uncaged (UV-irradiated) and crosslinked immediately or left to a second chase for indicated times. After cell fixation, cells were subjected to click reaction and IF. B) Quantification of lysosomal lipid egress. Pearson's R value of non-thresholded images from lipid channel vs. LAMP1 immunofluorescence, calculated for each time point ( $n \geq 51$ ) using the Coloc 2 feature from Fiji. (ns P-value > 0.5 \*P  $\leq$  0.05 \*\*P-value  $\leq$  0.01 \*\*\*P-value  $\leq$  0.001 \*\*\*\*P-value  $\leq$  0.0001). Scale bars represent 10  $\mu$ m.

On the other hand, it is very interesting that SK1/SK2  $-/-$  cells do present a similar NPC1 storage phenotype, whereas SGPL1  $-/-$  cells do not as seen in Figure 2.21 (A) and quantified in Figure 2.21 (B). Therefore, it is tempting to speculate that the kinases themselves could act at contact sites and serve in facilitating LY/ER export. It has been shown that particularly SK1 localizes to endosomes and phagosomes, where depletion of SK1 impacts endocytic trafficking<sup>227</sup>. However, further experimental evidence is needed to determine in which way the kinases contribute to lysosomal sphingosine exit, but previous data could point towards SK1 having a role in lysosomal export<sup>228</sup>.

### 2.3.1 Miglustat as a drug for the treatment of Niemann-Pick Type C1

To date, miglustat, an inhibitor of the enzyme glucosylceramide synthase (GCS)<sup>229</sup>, which is involved in the first step of glycosphingolipid synthesis, is the only drug approved for the treatment of NPC1 patients. However, the mechanism of action of miglustat in NPC has not been fully elucidated. Initially it was developed for patients with Type 1 Gaucher disease<sup>230–232</sup>, another lysosomal storage disorder. Therefore, I envisioned that the lyso-probes could be used in studying the subcellular effects of miglustat. To address if treatment with miglustat would improve Chol and or Sph trafficking in NPC1  $-/-$  cells. I pulsed cells with lyso-pacSph or lyso-pacChol for 1 hour and 45 minutes, respectively. Then, the medium was removed, and cells were subjected to incubation with 50  $\mu$ M miglustat, 16-18h prior to experiments.

Reassuring previous findings, and as seen from Figure 2.20 (A,B) and quantification (C), Miglustat treated cells, showed reduced PCC of total lipid signal versus LAMP1 stained compartments, which suggests an efflux of lysosomal cholesterol<sup>233,234</sup> comparable to WT levels (as seen from quantification in figure 2.20, C). It is tempting to speculate that this phenomenon could be attributed to the formation of dedicated membrane contact sites and that cholesterol could be rescued by the actions of proteins such as Gramd1b<sup>85</sup>, ORP1L<sup>88,89,235,236</sup>, or STARD3<sup>90</sup>. Here, it is possible that the formation of LD, which is observed at 60 minutes, could be enhanced due to contact sites. This observation has been previously attributed to ORP1L playing a role in the rescue of cholesterol and restoring LD formation in the absence of NPC1<sup>237</sup>. It

is also possible that cholesterol rescue could be enhanced by activation of another protein/enzyme up- or downstream, in the same fashion as methyl- $\beta$ -cyclodextrin which leads to activation of AMP-activated protein kinase and restores lysosomal cholesterol accumulation<sup>238</sup>. Similarly, the Spiegel lab has demonstrated, that cholesterol could be rescued in NPC1<sup>-/-</sup> cells when employing an SphK1 activator (SK1-A), resulting in reduced levels of cholesterol and other sphingoid bases<sup>239</sup>.

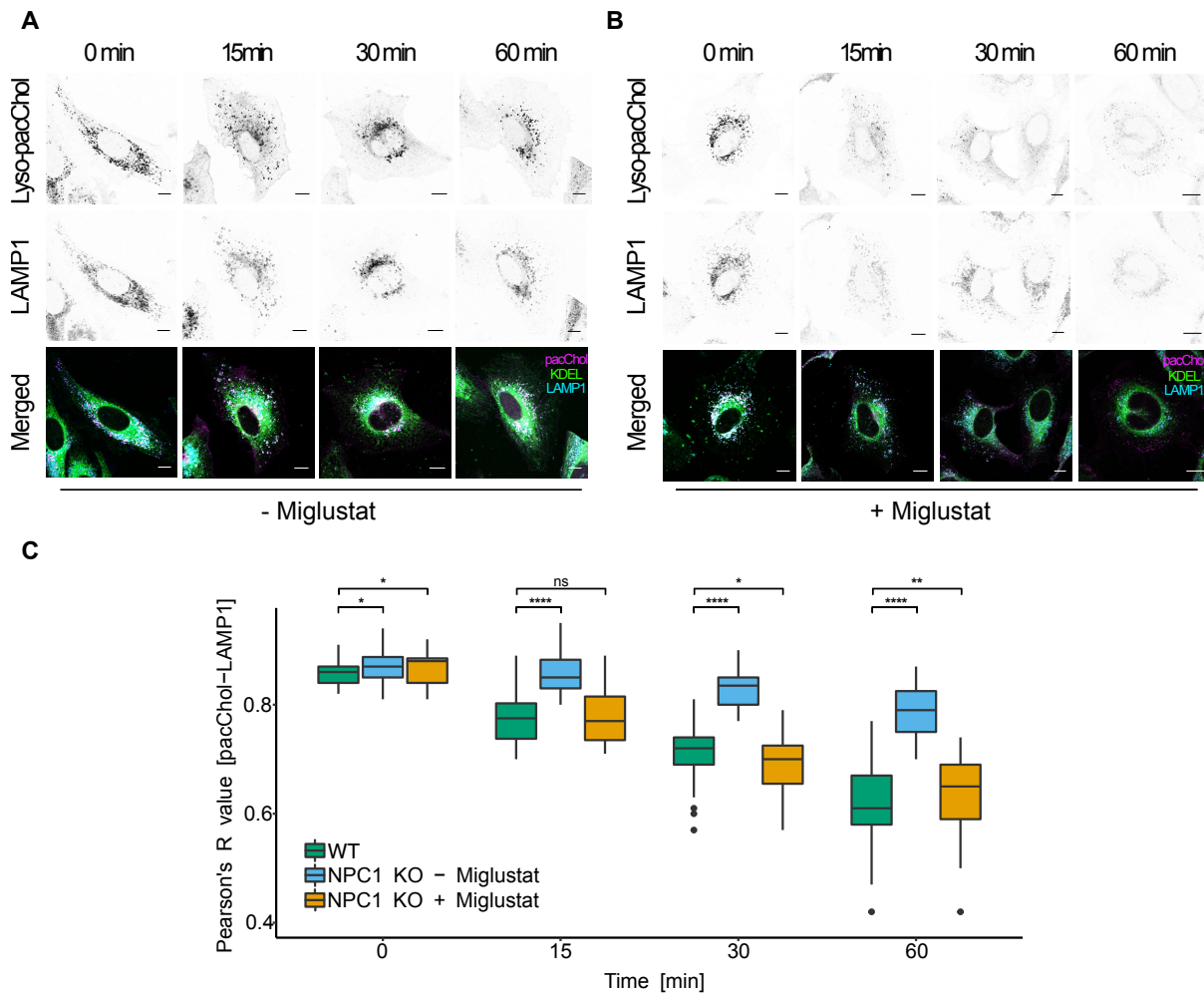


**Fig. 2.20** Visualization of lysosomal export of cholesterol in NPC1 cells in treated and non-treated with miglustat. A) Confocal microscopy of N3-Alexa488-labelled lyso-pacChol fixed cells. HeLa cells were pulsed with 10  $\mu$ M of Lyso-pacChol for 45 minutes and chased overnight. Next, uncaged (UV-irradiated) and crosslinked immediately or left to a second chase for indicated times. After cell fixation, cells were subjected to click reaction and IF. A) Non-treated B) Treated with miglustat C) Quantification of lysosomal lipid egress. Pearson's R value of non-thresholded images from lipid channel vs. LAMP1 immunofluorescence, calculated for each time point ( $n \geq 48$ ) using the Coloc 2 feature from Fiji. (ns P-value  $> 0.5$  \*P  $\leq 0.05$  \*\*P-value  $\leq 0.01$  \*\*\*P-value  $\leq 0.001$  \*\*\*\*P-value  $\leq 0.0001$ ). Scale bars represent 10  $\mu$ m.

On the other hand, the sphingosine export blockage in NPC1 did not show further improvement upon Miglustat treatment as seen from Figure 2.21, which shows a consistently high colocalization with LAMP1-positive compartments for the entire duration of the timecourse. This could be another hint towards Miglustat influencing cholesterol-dedicated contact sites and therefore, facilitating cholesterol transport. Moreover, it could also indicate a direct NPC1-dependent transport of Sph out of LE/LY, where Sph can not escape LE/LY if NPC1 is not present. However, one still open question is: how can a drug that inhibits the synthesis of glycosphingolipids ameliorate NPC symptoms and restore cholesterol transport? Few potential mechanisms could explain an NPC1-independent transport of cholesterol. It is possible that cholesterol transport could be enhanced by NPC2 in a lipid-dependent manner, as it has been shown that increments of intracellular LBPA levels lead to NPC2-mediated transport of cholesterol out of LE/LY in the absence of NPC1<sup>240,241</sup>. Here, lipidomic analyses of NPC1 treated with miglustat could reveal which lipid species are up- and down-regulated to abide by this theory. Furthermore, intracellular cholesterol trafficking could be facilitated by additional lysosomal accessory proteins, such as the lysosomal abundant membrane protein 1 and 2 (LAMP1/LAMP2) and the lysosomal integral membrane protein 2 (LIMP-2), proteins which have been demonstrated to transport cholesterol<sup>91,92,242,243</sup>, alongside NPC1. Here it is tempting to speculate that reduction in levels of glycosphingolipids, could influence and restore the blockage of cholesterol transport in an NPC1-independent manner, enlisting LAMP1/2 and LIMP-2.

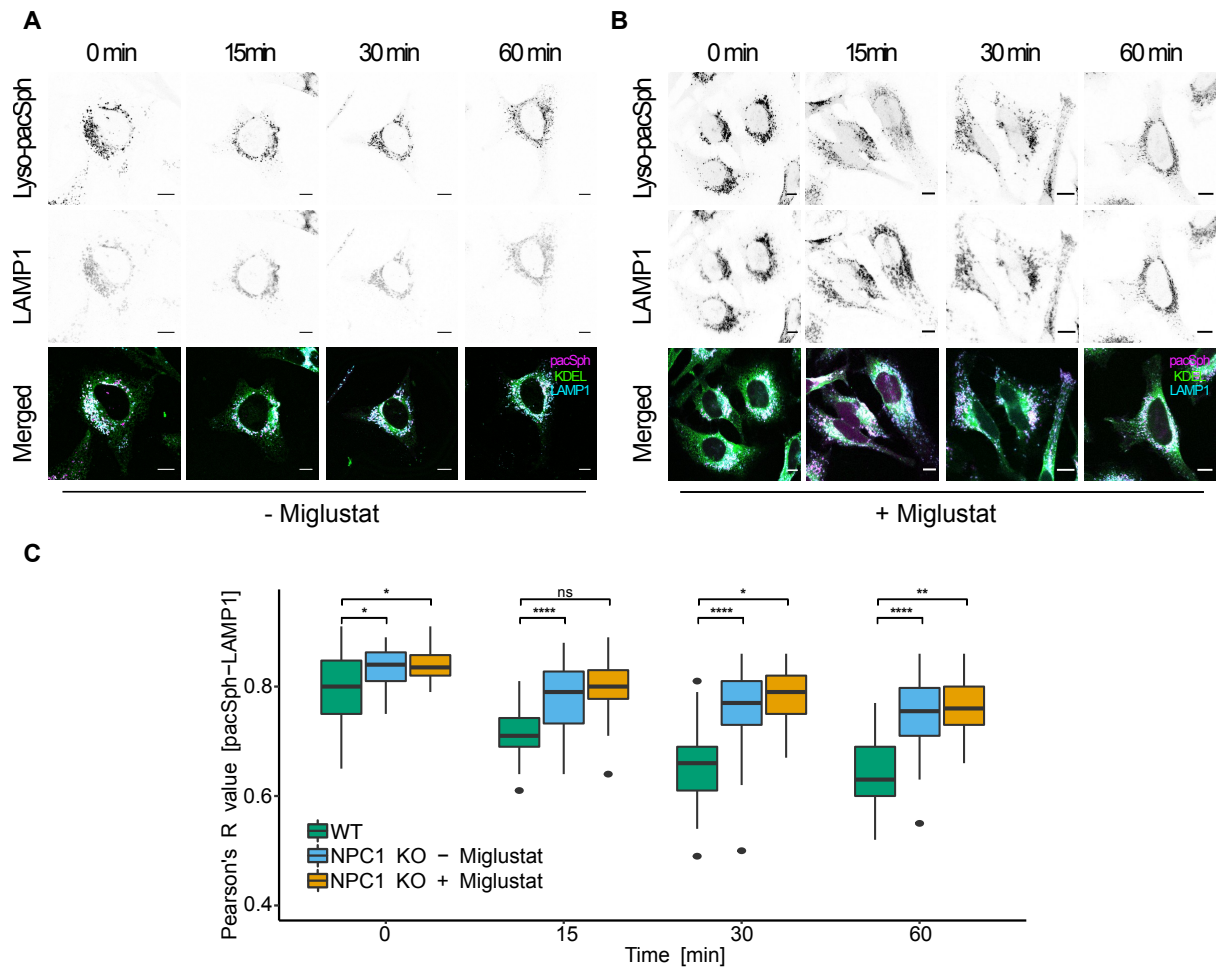


**Fig. 2.21** Visualization of lysosomal export of sphingosine in NPC1 cells in treated and non-treated with miglustat. A) Confocal microscopy of N3-Alexa594-labelled lyso-pacSph fixed cells. HeLa cells were pulsed with 10  $\mu$ M of Lyso-pacSph for 60 minutes and chased overnight. Next, uncaged (UV-irradiated) and crosslinked immediately or left to a second chase for indicated times. After cell fixation, cells were subjected to click reaction and IF. A) Non-treated B) Treated with miglustat C) Quantification of lysosomal lipid egress. Pearson's R value of non-thresholded images from lipid channel vs. LAMP1 immunofluorescence, calculated for each time point ( $n \geq 48$ ) using the Coloc 2 feature from Fiji. (ns P-value  $> 0.5$  \*P  $\leq 0.05$  \*\*P-value  $\leq 0.01$  \*\*\*P-value  $\leq 0.001$  \*\*\*\*P-value  $\leq 0.0001$ ). Scale bars represent 10  $\mu$ m.

Overall, I have been able to show the applicability of the lyso-probes in a new setup, such as drug therapy on a cellular disease model. My findings back up reassuring previous findings<sup>233,244-246</sup>, which employ miglustat in animal mouse models and patient cells and show the benefits of miglustat treatment in NPC.

## 2.4 Design, outcome and biochemical validation of chemoproteomic profiling of Lyso-pacSph and Lyso-pacChol

A key improvement of the lyso-probes is the tempo-spatially controlled liberation of lipid probes, which can also profile for protein-lipid interactions. In this way we are able to identify the interacting proteome for a single lipid species such as Sph or Chol on a subcellular level i.e., the lysosome. To this end, a master student in the lab, Judith Notbohm performed an unbiased chemoproteomic profiling of cholesterol and sphingosine lysosomal interacting proteins (for workflow see figure 2.22). Briefly, HeLa SGPL1  $-/-$  were labeled with 5  $\mu$ M Lyso-pacSph or HeLa WT cells with 10  $\mu$ M Lyso-pacChol for 1h and chased overnight. As a control, the globally distributed probes pacSph (2  $\mu$ M) and pacChol (10  $\mu$ M) were fed to the cells for 1h. Next, cells were irradiated with UV light for 90 s, whereas control samples were treated with the probes but were not UV irradiated (-UV light control). After uncaging, photoaffinity labeling was performed under ice-cold conditions to ensure maximal lysosomal crosslinking. Next, protein-lipid complexes were reacted via click chemistry with biotin-azide and subsequently enriched via streptavidin beads. MS samples were further processed and analysed by Frank Stein and Per Haberkant at EMBL proteomic facility, where samples were subjected to tandem mass tag (TMT) labelling<sup>247</sup>, digested by trypsin and separated via liquid chromatography before mass spectrometric identification.

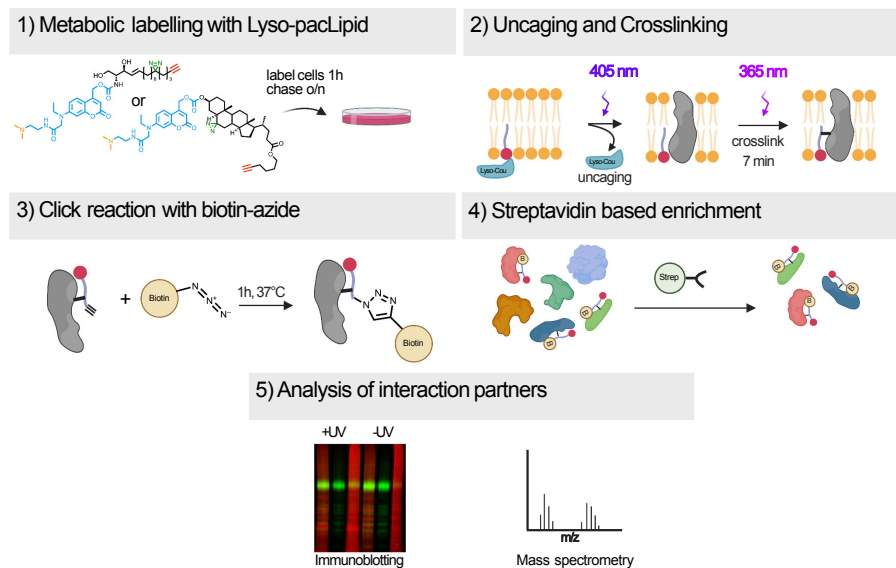


**Fig. 2.22** Workflow for streptavidin pull-down of Lyso-pacSph and Lyso-pacChol probes as performed by Judith Notbohm. Created with BioRender.com

Chemoproteomic analysis revealed a total of 1629 proteins for cholesterol and 1642 proteins for sphingosine (data not shown). Next, proteins were curated and considered a hit if the false discovery rate was below 0.05 and if additionally, a fold-change of at least 2 was observed. While a high number of background proteins that were not classified as hits or candidates were present, a small number of proteins were classified hits for both Lyso-pacSph (6 proteins) and Lyso-pacChol (12 proteins) (see table 2.3). Reassuringly, mostly lysosomal or endosomal proteins, as well as known cholesterol interactors such as NPC1, were identified in the cholesterol screen. Additionally, 6 of the identified proteins were previously found employing bi-functional cholesterol<sup>147</sup>, further strengthening them as bona fide interactors. For the lesser investigated Sph hits, Judith found 2 proteins previously reported to interact with sphingosine using bi-functional analogs<sup>148</sup> and 4 which have not been reported to date.

Surprisingly, two lysosomal proteins, which are known for facilitating cholesterol export out of LE/LY were found as well in the Sph screen. Here, NPC1 and LIMP-2 were identified as Sph interactors. This in addition to previous confocal microscopy experiments, where I could visualize a transport defect on NPC1 *-/-* cells, argues for NPC1 to have a direct role in Sph transport out of LE/LY. This would reassure our hypothesis of NPC1 as a potential Sph transporter.

**A**

Lyso-pacChol hits			
Gene name	Protein	Subcellular localisation	Identified with pacChol?*
<i>NPC1</i>	Niemman-Pick C1 protein	Lysosome, Endosome	Yes
<i>LAMP1</i>	Lysosomal-associated membrane protein 1	Lysosome, Endosome	Yes
<i>TMEM87A</i>	Transmembrane protein 87A	Golgi apparatus	Yes
<i>MFSD1</i>	Major facilitator superfamily domain-containing protein 1	Lysosome	No
<i>NCSTN</i>	Nicastrin	Cytosol	No
<i>SLC3A2</i>	4F2 cell-surface antigen heavy chain	Lysosome	No
<i>SLC7A5</i>	Large neutral amino acids transporter small unit 1	Lysosome	Yes
<i>CD63</i>	Cell surface antigen	Lysosome, Endosome	Yes
<i>TMEM192</i>	Transmembrane protein 192	Lysosome, Endosome	No
<i>HIST1H2BF</i>	Histone H2B type 1-C/E/F/G/I	Nucleus	No
<i>CD44</i>	CD44 antigen	Plasma membrane	Yes
<i>TMEM245</i>	Transmembrane protein 245	Plasma membrane, cytosol	No

**B**

Lyso-pacSph hits			
Gene name	Protein	Subcellular localisation	Identified with pacSph?*
<i>NPC1</i>	Niemman-Pick C1 protein	Lysosome, Endosome	No
<i>TPP1</i>	Tripeptidyl-peptidase 1	Lysosome	Yes
<i>TSPAN3</i>	Tetraspanin-3	Endosome	No
<i>LIMP2</i>	Lysosome membrane protein 2	Lysosome	Yes
<i>TTYH3</i>	Protein tweety homolog 3	Plasma membrane	No
<i>SCARB1</i>	Scavenger receptor class B member 1	Plasma membrane	No

**Table 2.3** List of hit proteins for both lyso-pacChol and lyso-pacSph screen. Hits were compared to previous screens from pacChol<sup>147</sup> and pacSph<sup>148</sup>.

To test this possibility and as well to validate MS hits. Judith performed immunoprecipitation assays for NPC1 and LIMP-2, where antibody detection for both proteins was performed successfully in multiple replicates (data not shown), thus verifying the validity of the MS screen and corroborating the interaction of Sph with NPC1 and LIMP-2. Together this data implies additional transport/recycling pathway(s) of lysosomal Sph, which could work in parallel, as they do for cholesterol.

Another interesting observation was the finding of two PM membrane proteins in the sphingosine screen. Potentially in agreement with my previous finding that Lyso-pacSph uncaging leads to redistribution of lysosomes to the cell periphery (see figure 2.18, C), this interaction could be attributed to the effect of calcium release from acidic stores which leads to LE/LY fusion with the PM<sup>223-225</sup>. An interesting candidate, SCARB-1 was identified as a potential interactor of Sph. This protein has been identified as a receptor for HDL, and uptake of cholesterol, fatty acids, and phospholipids from the extracellular space<sup>248-250</sup>. Moreover, SCARB-1 has been characterized as an HDL-dependent cholesterol efflux protein<sup>250</sup>. Therefore, I validated this interaction in a pulse-chase fashion. Due to my previous observations, I decided to perform immunoprecipitation assays, first at 0 minutes, as a starting point and in order to ensure that Sph has time to reach the PM, I uncaged cells incubated with lyso-pacSph and then allowed for an additional 20 minutes chase (as seen previously from my microscopy images, where there is a lysosomal rearrangement towards the PM). Antibody detection in streptavidin-mediated pull-down showed SCARB-1 a faint band in the eluate fraction (see figure 2.23), suggesting successful crosslinking of lyso-pacSph with a small number of SCARB-1 molecules. However, additional replicates did not show the presence of SCARB-1 in the eluates fractions (data not shown).

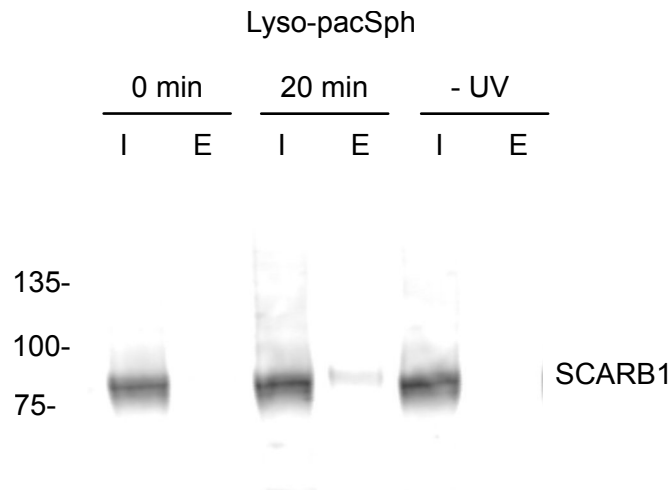


**Fig. 2.23** Validation of SCARB1 as a potential Sph interactor. Western blot of SCARB1 upon biotin-streptavidin pulldown. I: Input, E: Eluate. Samples were either UV irradiated or – UV (control) where the photocrosslinking step was omitted.

This could indicate that SCARB1 interacts with a low-abundant Sph-metabolite such as S1P as this interaction has been shown for other PM-resident proteins<sup>251–254</sup>. Additionally, it could direct that its identification in the mass spectrometric screen was a false positive, which highlights the necessity of hit validation in order to reassure the interactions obtained from the MS screen.

#### **2.4.1 Metabolism and subcellular localization of Sph and Chol in NPC1 and LIMP2 null cells**

Following up on Judith’s MS screen with the identification and biochemical validation of both NPC1 and LIMP2 proteins as Chol and novel Sph-binding proteins. I next sought to investigate if loss of either protein would impact on sphingosine as it does cholesterol transport. Therefore, I employed HeLa WT, NPC1  $\text{-/-}$  cells which were a kind gift from the Annaert Lab in Belgium and LIMP2  $\text{-/-}$  cells generated by the Saftig lab in Kiel. The metabolic incorporation of Lyso-pacChol and Lyso-pacSph was conducted by TLC analysis following pulse-chase experiments for up to 240 min as previously described<sup>153</sup>. To this end, I followed the post-lysosomal metabolism of cholesterol to cholesterol-esters (see figure 2.24, A). TLC analysis showed reduced levels of chol-esters as well as slower conversion to chol-esters in NPC1  $\text{-/-}$  and LIMP2  $\text{-/-}$  compared to WT (see figure 2.24, B), where LIMP2  $\text{-/-}$  cells seem to show slightly, albeit not significantly, faster conversion. Considered together, these data suggest that

lysosomal cholesterol fails to reach the ER in LIMP-2  $-/-$  in a similar way as it does in NPC1  $-/-$ , this is in agreement with previous studies where incorporation of bi-functional cholesterol or BODIPY-Cholesterol into chol-esters is severely delayed<sup>57,85,92</sup>.

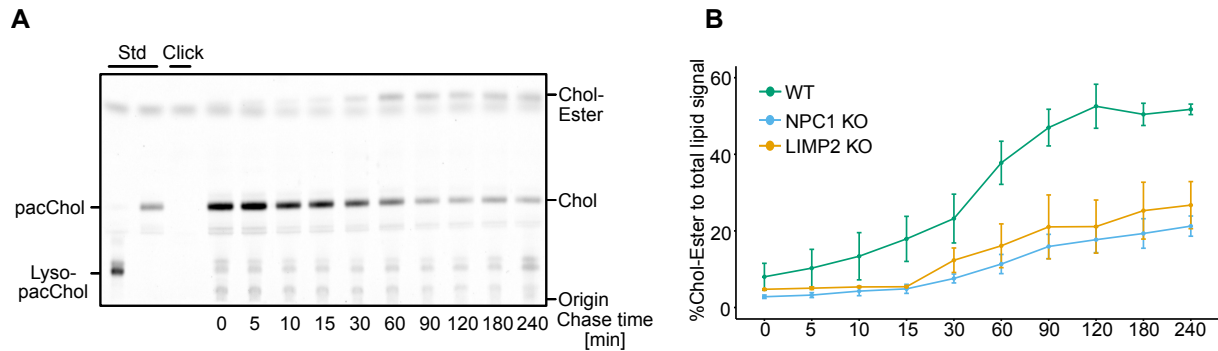


**Fig. 2.24** Thin-layer chromatography of lysosomal export of cholesterol in cellular disease models. Post lysosomal metabolism of Lyso-pacChol. A) HeLa WT cells were labelled with Lyso-pacChol (10  $\mu$ M) for 45 minutes and chased overnight. Upon uncaging, cells were chased and lipids extracted at indicated times, clicked with 3-azido-7-hydroxycoumarin and visualized by thin-layer chromatography. B) Quantification of post lysosomal cholesterol metabolism. Quantification of cholesterol esterification in WT, NPC1, and LIMP2 -deficient HeLa cells. The intensity of the bands corresponding to pacChol and pacChol-Ester were added for each time point and the intensity of the ester-band with respect to the sum of both was displayed as a percentage. All values were calculated for each time point in three independent experiments

On the other hand, analysis of post-lysosomal metabolism of Sph in WT cells revealed immediate conversion into higher sphingolipids, such as Cer and SM, as well as the incorporation of the labeled backbone into phospholipids, yielding species such as PC and PE (see figure 2.25, A). Observing such varied metabolites even at nominally 0 minutes of chase could be attributed to minute-long incubation times after uncaging and before lipid extraction that could not be prevented due to time needed for cell collection. Of note, the Riezman lab recently reported a caged, lysosome-targeted deuterated sphingosine. However, when analyzing its metabolic fate, only immediate metabolites S1P and Cer were analyzed<sup>187</sup>. With respect to our data, it is highly possible that the rapid metabolism also generated other lipid species such as phospholipids. Moreover, I performed a detailed analysis of Cer production. Here, I found equal results in HeLa WT cells, as previously reported from Feng *et al.*<sup>187</sup> when analyzing Cer production; after exiting the lysosome, sphingosine reaches the ER to form Cer, a reaction that is catalyzed by various Cer-synthases. Here, I found that levels of Cer are increased up to 5-10 minutes, maintained, and decreased after 15-30 minutes. Similarly, studies employing tri-functional sphingosine showed increased

levels of Cer up to 10 minutes; however, these levels remained constant up to 180 minutes<sup>153</sup>, which is consistent with previous findings where the subcellular localization of sphingosine determines ceramide synthesis and lipid footprint<sup>153,187,188</sup>. Next, I analyzed the post-lysosomal metabolism of Sph in NPC1  $-/-$  cells. Here, I could visualize (and quantify in figure 2.25 D) less conversion into other lipid species across all time points, but most importantly, I found consistently higher levels of Sph (as seen from quantification) in NPC1  $-/-$  for the duration of the experiments. This already speaks for the fact that loss of NPC1 has a dramatic effect on Sph levels, as seen from confocal microscopy images in Figure 2.19, where I visualized Sph storage in LAMP-1 positive compartments. On the other hand, LIMP-2  $-/-$  cells appear to have only a minor elevation in the levels of Sph but a time-dependent decrease with similar kinetics as WT cells.

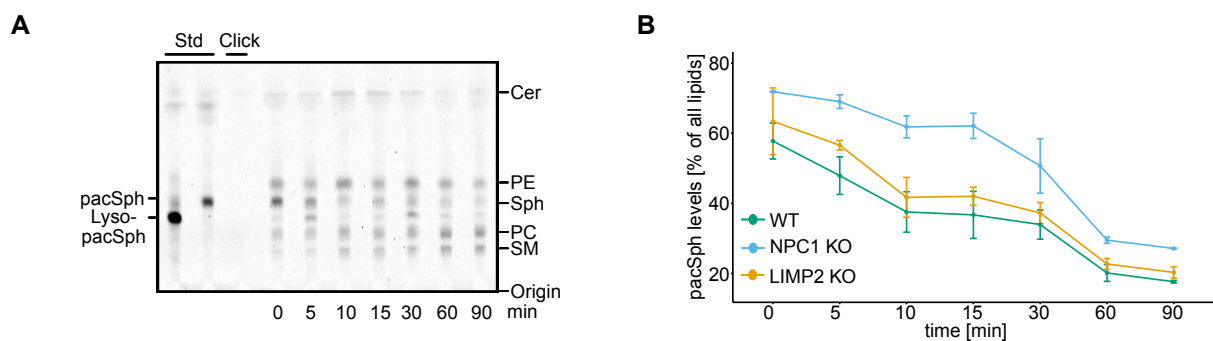


**Fig. 2.25** Thin-layer chromatography of lysosomal export of sphingosine in cellular disease models. Post lysosomal metabolism of Lyso-pacSph. A) HeLa WT cells were labeled with Lyso-pacSph (10  $\mu$ M) for 1h and chased overnight. Upon uncaging, cells were chased, and lipids extracted at indicated times, clicked with 3-azido-7-hydroxycoumarin and visualized by thin-layer chromatography. B) Quantification of post lysosomal sphingosine metabolism. Quantification of lysosomal sphingosine (Sph) export in WT, NPC1 and LIMP2-deficient HeLa cells. Sph is readily metabolized to ceramide (Cer) and sphingomyelin (SM) via the biosynthetic sphingolipid pathway, but also to phosphatidylethanolamine (PE) and phosphatidylcholine (PC) via the SGPL1-breakdown pathway. The intensity of Sph is expressed as a percentage compared to the sum of all labeled lipids. All values were calculated for each time point in three independent experiments. Data are shown as mean  $\pm$  standard error.

Demonstrated by us and other labs, two lysosomal proteins NPC1 and LIMP-2 facilitate cholesterol export. Here, I have demonstrated that loss of either protein leads to impaired lysosomal egress of not just cholesterol, but also sphingosine, as hinted by TLC. Therefore, I asked if this defect could also be visualized by confocal microscopy. To this end, HeLa WT, NPC1  $-/-$  and LIMP-2  $-/-$  were pulsed with Lyso-pacSph or Lyso-pacChol and chased overnight.

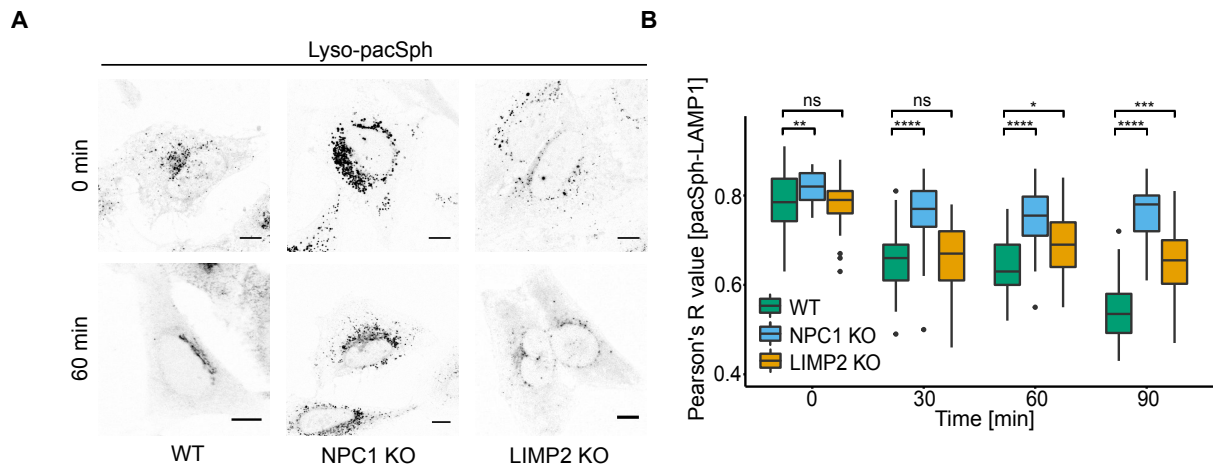


**Fig. 2.26** Visualization of lysosomal export of sphingosine in WT and NPC1 KO and LIMP2 KO cells. A) Confocal microscopy of N3-Alexa594-labelled lyso-pacSph fixed cells. HeLa cells were pulsed with 10  $\mu$ M of Lyso-pacSph for 60 minutes and chased overnight. Next, uncaged (UV-irradiated) and crosslinked immediately or left to a second chase for indicated times. After cell fixation, cells were subjected to click reaction and IF. B) Quantification of lysosomal lipid egress. Pearson's R value of non-thresholded images from lipid channel vs. LAMP1 immunofluorescence, calculated for each time point ( $n \geq 48$ ) using the Coloc 2 feature from Fiji. (ns P-value  $> 0.5$  \* $P \leq 0.05$  \*\* $P$ -value  $\leq 0.01$  \*\*\* $P$ -value  $\leq 0.001$  \*\*\*\* $P$ -value  $\leq 0.0001$ ). Scale bars represent 10  $\mu$ m.

Pulse-chase experiments in HeLa WT cells revealed the subcellular localization of Lyso-pacSph to exclusively colocalize with the late endosomal/lysosomal marker LAMP-1 at 0 minutes in all 3 cell lines, after uncaging and including an additional chase time, I could visualize sphingosine transport across other organelles such as the Golgi network up to 90 minutes (see Appendix for time course with organelle co-localization). However, in NPC1  $-/-$  cells a severe accumulation of sphingosine in LAMP-1 positive compartments was again detected (see figure 2.26, A), whereas LIMP-2  $-/-$  cells display an intermediate phenotype showing impaired egress out of endocytic organelles (see figure 2.26, A). Moreover, colocalization analysis corroborated these observations with a PCC remaining constant for NPC1  $-/-$  cells and a slight drop for LIMP-2  $-/-$  cells, compared to WT; suggesting that Lyso-pacSph has been retained/delayed at the lysosome (see figure 2.26,A and quantification in B).

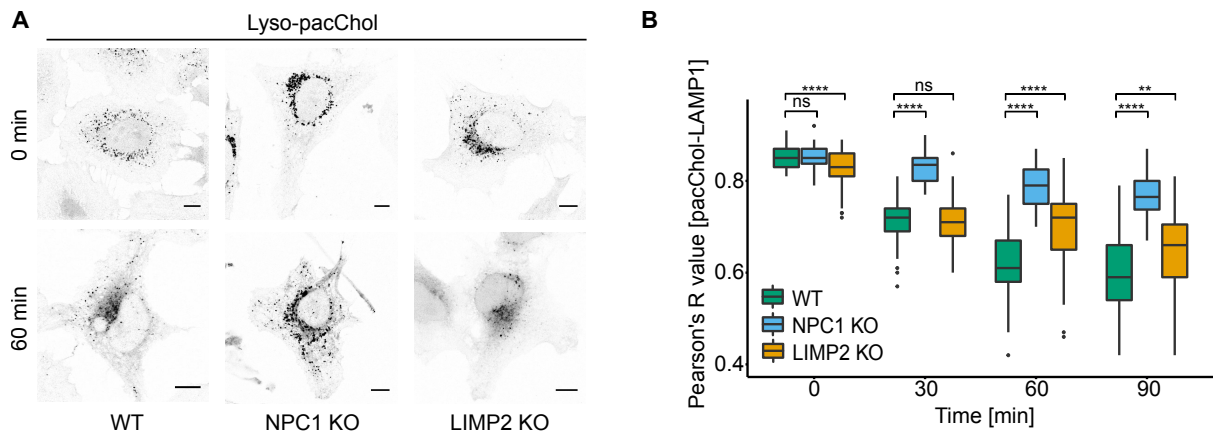


**Fig. 2.27** Visualization of lysosomal export of cholesterol in WT and NPC1 KO and LIMP2 KO cells A) Confocal microscopy of N3-Alexa488-labelled lyso-pacChol fixed cells. HeLa cells were pulsed with 10  $\mu$ M of Lyso-pacChol for 45 minutes and chased overnight. Next, uncaged (UV-irradiated) and crosslinked immediately or left to a second chase for indicated times. After cell fixation, cells were subjected to click reaction and IF. B) Quantification of lysosomal lipid egress. Pearson's R value of non-thresholded images from lipid channel vs. LAMP1 immunofluorescence, calculated for each time point ( $n \geq 48$ ) using the Coloc 2 feature from Fiji. (ns P-value  $> 0.5$  \*P  $\leq 0.05$  \*\*P-value  $\leq 0.01$  \*\*\*P-value  $\leq 0.001$  \*\*\*\*P-value  $\leq 0.0001$ ). Scale bars represent 10  $\mu$ m.

These results were comparable when visualizing Lyso-pacChol trafficking in NPC1  $-/-$  and LIMP2  $-/-$  cells (see figure 2.27, quantification in B) where a defective transport of cholesterol is known, resulting in endo/lysosomal accumulation of cholesterol. Again, the effect of LIMP2  $-/-$  is less pronounced. Altogether, this data demonstrates that lysosomal sphingosine transport can happen with help of other proteins such as LIMP-2, the function of which was reported for binding to cholesterol and PS<sup>255</sup>. Alternatively, I show that the absence of NPC1 results in dramatic storage of Sph. This has been previously shown in multiple tissues of NPC patients, where Sph levels are increased in a distinctive manner<sup>73</sup>. This could represent an alternative transport for Sph, which could work in parallel with the LIMP-2 pathway. However, studies by TLC and confocal microscopy show that NPC1 deficiency leads to a much stronger delay in sphingosine metabolism and export, which could argue for an NPC1-dependent transport being the dominant pathway. NPC1 and LIMP-2 crystal structures are available, both proteins feature a hydrophobic tunnel-like cavity<sup>60,100,256</sup>, through which cholesterol has been demonstrated to exit LE/LY. Here is tempting to speculate that such tunnels could also facilitate Sph export from the LE/LY to the ER or other subcellular compartments. However, more experimental data needs to be generated to support this theory.

## 2.4.2 Lysosomal impaired efflux of sphingosine is a direct effect of NPC1 disfunction

While structural studies have provided helpful insight into the architecture of NPC1, its function has not been fully elucidated. However, in diseased cells sphingosine storage has been described as the initiating step of NPC disease and being the first detectable lipid to accumulate in LE/LY upon pharmacological inhibition of NPC1<sup>257</sup>, leading to the accumulation of other lipid species such as cholesterol, GSL and SM in LE/LY<sup>71,72,234,258,259</sup>. Next, we tested the hypothesis that blockage of sphingosine in lysosomes might be directly due to defective NPC1-mediated transport. Alternatively, such an export block could be a secondary effect of cholesterol accumulation. To study this, I tried to uncouple NPC1 presence from high lysosomal cholesterol levels. First, I incubated NPC1 <sup>-/-</sup> cells with lipoprotein-free medium, which drastically lowered lysosomal cholesterol levels as seen from filipin staining (see figure 2.28, A and quantified in B). In a second approach, I combined lipoprotein starvation with simvastatin treatment, in order to inhibit the first steps of sterol biosynthesis and to reduce cellular cholesterol levels even further. On this background, I incubated cells with Lyso-pacSph and followed its transport. As seen from Figure 2.28 (C) both treatments show as high Sph colocalization with lysosomal marker levels as in non-treated NPC1 cells. Therefore, reducing cholesterol levels in NPC1 <sup>-/-</sup> cells failed to rescue sphingosine the export defect (see quantification as well).

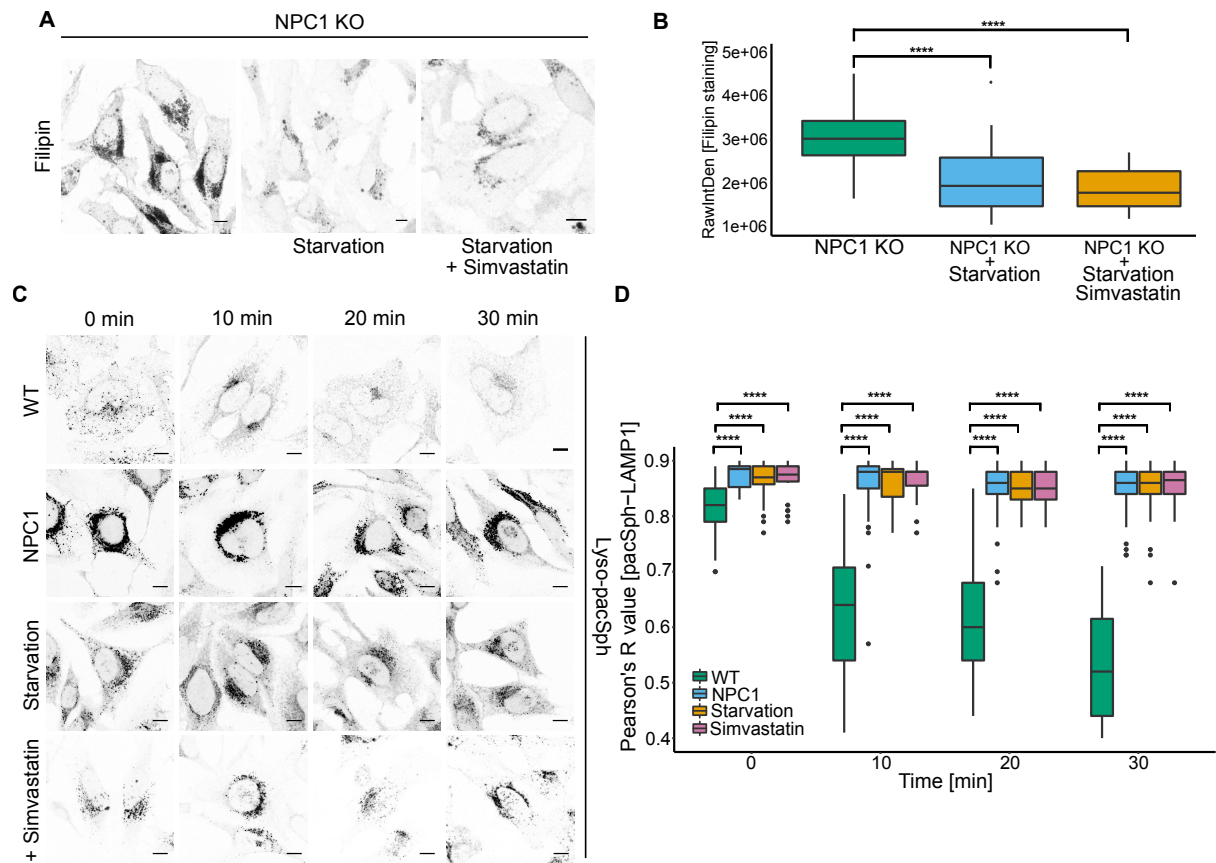


**Fig. 2.28** Sphingosine accumulation is a direct effect from loss of NPC1

A) Effect of lipoprotein deficient medium. Confocal images of HeLa NPC1 KO cells in regular medium conditions, incubated with lipoprotein deficient medium and simvastatin treatment 48h prior imaging. B) Quantification of cholesterol levels via filipin staining. C) HeLa NPC1 KO cells incubated with lipoprotein deficient medium 48h prior to imaging (Starvation) and treated with 5  $\mu$ M 24h prior to imaging. Next, cells were labeled with Lyso-pacSph (1.25  $\mu$ M) for 1h and chased overnight. Upon uncaging, cells were chased from 0 to 30 min, crosslinked, fixed with methanol and functionalized with AlexaFluor 594-Picolyl-Azide. Scale bar: 10  $\mu$ m. D) Quantification of lysosomal lipid egress. Pearson's R value of non-thresholded images from lipid channel vs LAMP1 immunofluorescence, calculated for each timepoint ( $n \geq 42$ ) using the Coloc 2 feature from Fiji. (ns P-value > 0.05 \*P  $\leq$  0.05 \*\*P-value  $\leq$  0.01 \*\*\*P-value  $\leq$  0.001 \*\*\*\*P-value  $\leq$  0.0001).

To investigate whether the NPC1 protein itself is involved in Sph trafficking, I made use of a small cationic amphiphile drug U1866A, which directly binds to NPC1 and was shown to block the export of cholesterol out of lysosomes<sup>80</sup>. Here, I incubated cells with 750 nM Lyso-pacChol or 1.25  $\mu$ M Lyso-pacSph and followed their transport after pulse-chase experiments. Not surprisingly, treatment with U1866A lead to cholesterol accumulation in LAMP1 positive compartments, which was expected. However, when using Lyso-pacSph, I could also visualize a transport defect, where Sph is indeed retained in lysosomes (see figure 2.29, A and quantified in B). These findings confirm the previous data obtained on NPC1  $-/-$  cells. Thereby supporting a

direct effect of NPC1 as opposed to potential compensatory mechanisms by deletion of the *Npc1* gene. This could potentially point towards a common export route between cholesterol and sphingosine.

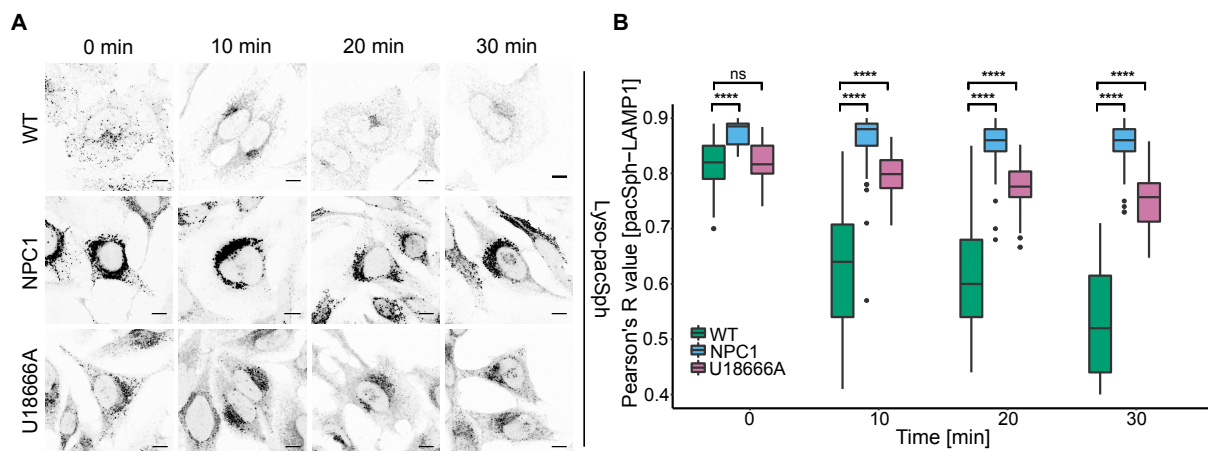


**Fig. 2.29** Sphingosine accumulation is a direct effect from loss of NPC1 A) HeLa WT cells treated with 0.5  $\mu\text{g}/\text{mL}$  U18666A 24h prior to imaging (U18666A) and HeLa NPC1 KO cells were labelled with Lyso-pacSph (1.25  $\mu\text{M}$ ) for 1h and chased overnight. Upon uncaging, cells were chased from 0 to 30 min, crosslinked, fixed with methanol and functionalised with AlexaFluor 594-Picolyl-Azide. Scale bar: 10  $\mu\text{m}$ . D) Quantification of lysosomal lipid egress. Pearson's R value of non-thresholded images from lipid channel vs LAMP1 immunofluorescence, calculated for each timepoint ( $n \geq 42$ ) using the Coloc 2 feature from Fiji. (ns P-value  $> 0.05$  \*P  $\leq 0.05$  \*\*P-value  $\leq 0.01$  \*\*\*P-value  $\leq 0.001$  \*\*\*\*P-value  $\leq 0.0001$ ).

Having confirmed that both cholesterol and sphingosine transport depend directly on NPC1, I next asked which lipid is the initially accumulating metabolite. To this end, I employed, the previously synthesized Lyso-Sph and Lyso-Chol probes, which lack the chemical functionalities of the Lyso-pacLipids in order to artificially increase lysosomal sph or Chol levels. To follow lipid export in this cellular model of NPC, HeLa WT cells were either labeled with 750 nM Lyso-pacChol (see figure 2.30, C) or 1.25  $\mu\text{M}$  Lyso-pacSph (see figure 2.30, A) and at the same time incubated with a 20x fold excess of Lyso-Sph (see figure 2.30, D). of note, sphingosine concentrations above this threshold lead to cellular death) or Lyso-Chol (see figure 2.30, B) to create NPC-like lipid accumulations. Next, the localization of the respective lyso-pacLipids was assessed by time-dependent crosslinking and staining. Surprisingly, I found that HeLa cells treated with 20x fold Sphingosine excess showed a prominent lysosomal cholesterol staining and a higher PCC after quantification (see figure 2.30, F) throughout the time course, whereas cells treated with a 20x fold excess cholesterol showed decreasing Sph co-localization as observed in WT cells. (see figure 2.30, E).

Lipid metabolites stored in NPC have been controversially debated over the years. Is it sphingosine the initially stored lipid? Perhaps initial sphingosine accumulation leads to the fatal and degenerative lysosomal storage disease? A previous study from the Platt lab shed light on NPC disease, demonstrating that upon incubation of WT cells with U18666A (such as I performed in this study), sphingosine is accumulated inside LE/LY and it is the earliest measurable readout (ca. 10 minutes) along with calcium impairment. While cholesterol accumulation was only observed after a 6-hour pulse with U18666A<sup>257</sup>. Throughout this thesis, we have talked about sphingosine and its subcellular actions. I have shown that after lysosomal Sph photorelease, calcium levels are elevated, as Höglinger et al.<sup>165</sup> previously demonstrated and that an excess of Sph can impair cholesterol trafficking, as shown from competition experiments. It is tempting to speculate, that after prolonged sphingosine storage, lysosomal calcium levels are lowered and this could influence lysosomal pH and therefore, an increase of lysosomal pH leads to a malfunction of NPC1? Previous studies have shown that cells incubated with U18666A restore cholesterol transport and other lipid species upon re-acidification of LE/LY<sup>260,261</sup>. Here, specifically, the use of lyso-pacSph in this condition could shed light on whether Sph transport is pH-dependent.

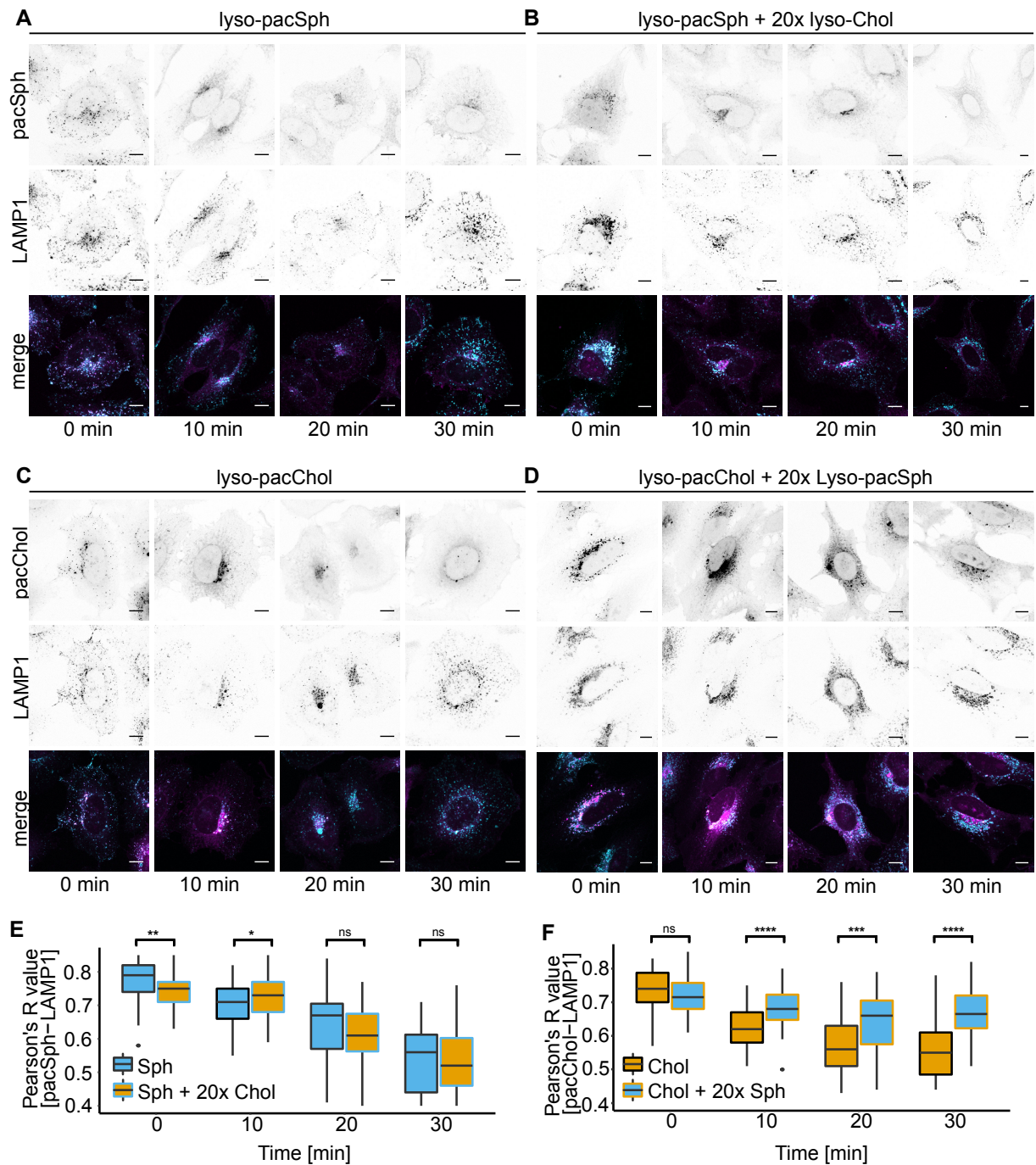


**Fig. 2.30** Spingosine accumulation is a direct effect from loss of NPC1 and can re-create an NPC1-like phenotype. Confocal images from HeLa WT cells labelled with either Lyso-pacSph (1.25  $\mu$ M) (A) and Lyso-Chol (25  $\mu$ M) (B) or Lyso-pacChol (750 nM) (C) and Lyso-Sph (15  $\mu$ M) (D) for 1h and chased overnight. Upon uncaging, chase-crosslinking experiments were performed from 0 to 30 min. Cells were fixed with methanol and functionalised with AlexaFluor 594-Picolyl-Azide (A,B) or AlexaFluor 488-Azide (C,D). (E, F) Quantification of lysosomal lipid egress from competition experiments. Pearson's R value of non-thresholded images from lipid channel vs LAMP1 immunofluorescence, calculated for each timepoint ( $n \geq 42$ ) using the Coloc 2 feature from Fiji. (ns P-value  $> 0.05$  \* $P \leq 0.05$  \*\* $P$ -value  $\leq 0.01$  \*\*\* $P$ -value  $\leq 0.001$  \*\*\*\* $P$ -value  $\leq 0.0001$ ). Scale bars represent 10  $\mu$ m.

In summary, my competition experiments revealed that Sph and Chol likely use the same NPC1-dependent export mechanism. To further investigate this commonality, I designed crosslinking experiments to study whether an excess of one lipid would affect binding of the other lipid to NPC1. Therefore, I performed in-lysate competition experiments and followed up on the interaction of NPC1 with sphingosine and cholesterol. As seen from Figure 2.31, immunoprecipitation of NPC1 can be achieved with concentrations above 50  $\mu$ M of pacSph. Of note, this is the first report (along with Judith's pull-down results) of an assay where it can be demonstrated that NPC1 interacts with Sph. In order to investigate if Sph or Chol excess would affect the interaction of pacSph with NPC1, I performed competition experiments with pacSph and endogenous Sph and Chol. Preliminary data shows that even at lower concentrations of 750 nM for lyso-pacChol and 1.25  $\mu$ M for lyso-pacSph, NPC1 can be pull-downed efficiently with the lyso-probes, once more highlighting the sensitivity of this assay (see figure 2.31, B). Moreover, I have demonstrated as seen from Figure 2.31 (C) that pacSph, can be competed with a 10x of Sph. This finding represents the genuine interaction between Sph and NPC1 and potentially hints towards a dedicated domain for Sph export. In this way, when incubating lysates from 500  $\mu$ M to 2.5 mM of Sph, NPC1 cannot be immunoprecipitated anymore as seen from the absence of the NPC1 band on the eluate fraction. From a physical chemistry point of view, two molecules cannot occupy the same space at the same moment, therefore it can be inferred that an excess of Sph can replace pacSph if there is an authentic interaction. On the other hand, cholesterol excess (up to 2.5 mM) failed to displace NPC1-Sph interaction as seen from Figure 2.31 (E), whereas a faint band in the eluate fraction can be seen even at higher concentrations of Chol in comparison to the Sph Western Blot, where after 250  $\mu$ M, NPC1 immunoprecipitation it is no longer seen.

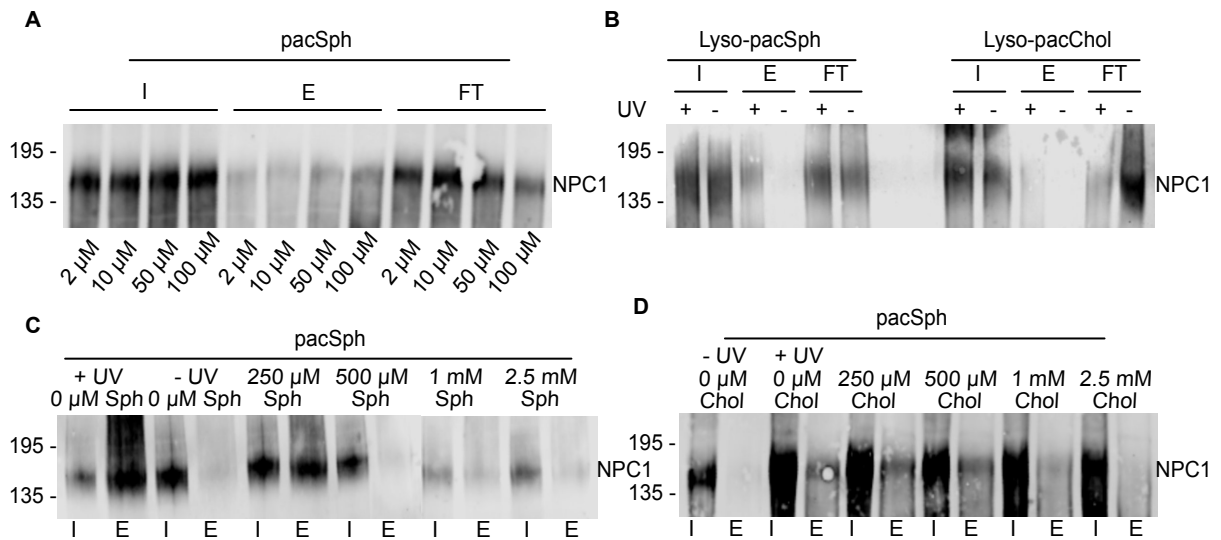


**Fig. 2.31** In-lysate competition experiments of NPC1 with Sph and Chol. A) Western Blot of NPC1-Sph immunoprecipitation titration. B) Western Blot of NPC1 immunoprecipitation with Lyso-pacChol and Lyso-pacSph in visualization competition conditions. C) Western Blot of pacSph competition with Sph D) Western Blot of pacSph competition with Chol. I: Input, E: Eluate, FT: Flow-through

In summary, this data suggests that Sph and Chol, indeed share a common mechanism of export, arguably via NPC1. Additionally, my experiments showed that sphingosine is likely the offending metabolite, which causes an NPC-like defect, given that it was the first to accumulate upon NPC1 inhibition<sup>257</sup> and that artificial elevation of its levels cause downstream cholesterol storage. Moreover, preliminary results of competition experiments in lysates revealed that an excess of cholesterol cannot (or only partially) displace Sph interaction with NPC1. Here, it is tempting to speculate that NPC1 could be a sphingosine regulated protein or likely a lysosomal sphingosine transporter. However, more detailed studies and replicates need to be performed in order to support this theory.

### 2.4.3 Conclusion and outlook

Caged, organelle-targeted lipid probes are powerful tools to dissect the actions of single lipid species on a subcellular level. They allow for their study with subcellular precision, granting insight into metabolism and protein-lipid interactions. Their photo-cleavable mask permits the manipulation of the levels of a single lipid species without

modifying lipid-handling proteins by inhibitors or genetic approaches, which often results in cells finding a mode to compensate for this loss.

Sph has been reported as a bioactive lipid. However, this small lipid has remained enigmatic, where few details, such as which enzymes participate in its metabolism and its inhibitory effect on PKC<sup>262</sup> are known. Yet, a detailed picture of its subcellular actions hasn't been described until now. In this thesis, I have synthesized new lysosome-targeted cholesterol and sphingosine probes, and due to their multifunctionalities, these probes can be employed to study lipid-protein interactions, metabolism, and visualization of lipid trafficking, starting from the lysosome. Using these probes, chemoproteomic analysis of cholesterol and sphingosine-interacting proteins has revealed unknown sphingosine-binding proteins such as LIMP-2 and NPC1. This could indicate that these proteins could be regulated by or be transporters of Sph. Biochemical validation, as immunoprecipitation experiments revealed direct binding, as well as competition between Sph and Chol to NPC1 and LIMP-2 uncovering a direct role of NPC1 in Sph handling. This paves a new and exciting way for further studies of sphingolipid trafficking. How NPC1 and LIMP-2 interact or directly contribute to lysosomal sphingosine egress remains unclear; however, it is tempting to speculate that sphingosine export could be facilitated in the same fashion as cholesterol via NPC1 or LIMP2 through their intramolecular efflux tunnel<sup>75,100,263</sup>. Recently, studies have shown that mutations to either tunnel arrest lysosomal cholesterol egress, reducing Chol-Ester levels<sup>263</sup>. Here, it would be particularly interesting to make use of tunnel mutants and employ lyso-pacSph in order to visualize its trafficking and conclude if indeed, Chol and Sph share the same export route.

Several questions remain concerning the mechanism of Sph transport out of LE/LY. First, it is unclear why a lipid would need of two different escape mechanisms, as in using NPC1 as a primary transport route and LIMP-2 as a secondary. This could be explained by the results performed by confocal microscopy and TLC. Where Chol and Sph retention at the LE/LY it is more severe in NPC1 <sup>-/-</sup> cells, compared to LIMP-2 where just a delay in lipid kinetics is observed. Second, how does the photorelease of an excess of Sph, induces cholesterol storage as in an NPC1-like phenotype? Here it is tempting to speculate that NPC1 could be an Sph-regulated protein.

Additional experiments revealed a direct effect of NPC1 on Sph transport. First, metabolic studies in NPC1 showed a delayed conversion of Sph to higher metabolites such as Cer and SM. Secondly, visualization experiments revealed a striking prolonged staining in LAMP-1 positive compartments in NPC1 <sup>-/-</sup> cells, which was comparable as in experiments with pharmacological inhibition of NPC1 with U18666A. Thirdly, I could observe that an excess of Sph can impair cholesterol trafficking. Here, it would be interesting to perform additional experiments, such as a lipidome analysis, in order to visualize if other lipid species such as glycosphingolipids are also retained at LE/LY such as in previous NPC1 disease models. Fourthly, additional competition experiments in lysates have gathered additional data on Sph and its interaction with NPC1. This last finding could suggest that Sph is indeed, preferentially trafficked by NPC1. Here, it is tempting to speculate about a possible biological model in which NPC1 is able to move Sph to the limiting membrane of the lysosome for transport at LE/LY-ER contact sites and there be transported by dedicated lipid transport proteins. Could it be that additionally to Chol and Sph, NPC1 is able to move other lipid species out of the LE/LY? And last, more in-depth investigations such as cross-linking mass spectrometry could potentially reveal and determine a binding site for Sph.

Taken together, these results provide first insights and a body of evidence, that lysosomal sphingosine egress is major dependent on NPC1, but its egress can also be facilitated by other lysosomal proteins such as LIMP-2, which until date have been only implied on cholesterol trafficking. Additionally, using this method we have provided powerful insight into cholesterol and sphingosine trafficking and metabolism in a time-resolved manner and hints of which organelle(s) might serve as the initial acceptor(s). Overall, lysosome-targeted, multi-functional lipid probes have allowed us to identify their organelle-specific interactome and established binding and possible transport of sphingosine by known cholesterol transporters. We envision that this technology could be further exploited to dissect the actions of single lipid species at other organelles such as the ER to have a clear image of LE/LY-ER lipid transport, adding to our understanding of not only sphingolipid trafficking but overall lipid biology.

# Chapter 3 – Experimental methods

---

## 3.1 Reagents

All common laboratory chemicals were obtained from commercial sources (Alfa Aesar, AppliChem, Carl Roth, Fisher Chemicals, Honeywell, Merck, Sigma-Aldrich and VWR) and were used without further purification. Synthetic d-erythro-sphingosine was purchased from Biozol (Eching, DE), photoclick sphingosine (pacSph) was purchased from Avanti polar lipids, photoclick cholesterol (pacChol) was purchased from Sigma Aldrich, supplied by Avanti polar lipids. Standards of photoactivatable and clickable lipids pacCer, pacSM, pacPC, pacGlcCer and pacHexCer analogues were a kind gift of Prof. Dr. Britta Brügger (BZH, Universität Heidelberg). Anhydrous solvents were either obtained from Sigma Aldrich or prepared via drying over activated molecular sieve 3 Å (Roth). Deuterated solvents for NMR analysis were purchased from Deutero (Karlsruhe, DE). CuAAC-based click chemistry reaction buffer kit and fluorescent Alexa-picolyl 488, 594, 647 azides were obtained from Jena Bioscience (Jena, DE). 3-Azido-7-hydroxycoumarin from Roth. The fluorescent calcium indicator Fluo-4-AM, LysoTracker Red DND-99 and Griffonia simplicifolia Lectin GS-II 647 were obtained from Life Technologies (Thermo Fisher Scientific, Waltham, USA).

## 3.2 Chemical Synthesis

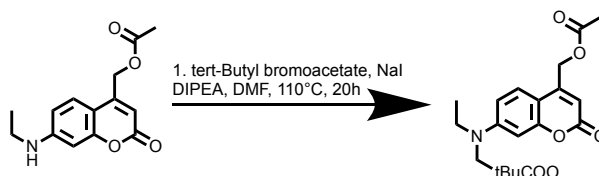
### 3.2.1 General synthetic procedures

All chemical reactions were carried out in dried glassware under inert atmosphere using dry solvents, all chemicals were purchased from commercial sources (Sigma Aldrich, Acros, VWR, Alfa Aesar, Roth or Merck) and were used without further purification. Deuterated solvents ( $\text{CDCl}_3$ ) were purchased from Deutero. Reactions at 0°C were performed in an ice/water cooling bath, reactions at – 20°C in an acetone/sodium chloride ice bath, changed every 1h. Reactions were monitored via TLC on precoated plates of silica gel 60 (Merck) using UV light for fluorescent

compounds (302 nm), using a solution of 10% phosphomolybdic acid (Sigma-Aldrich) in absolute EtOH (w/v) or precoated plates of silica gel 60 with fluorescent indicator F<sup>254</sup> (Merck 60). Preparative column chromatography was performed using silica gel 60, grain size 0.063 – 0.212 mm (Sigma-Aldrich) under pressure ( $\leq 1.5$  bar). Detailed solvent compositions are indicated individually. Crude product was dissolved in solvent, coated on to silica gel and applied as dry load. Evaporation *in vacuo* was performed at 40 °C and 900 – 0.1 mbar. NMR spectra were recorded on a Varian Mercury Plus (300 MHz) or Varian NMR System (500 MHz) at 298 K in the NMR department of the Institute of Pharmacy and Molecular Biotechnology, Heidelberg. Samples were dissolved in deuterated solvents (CDCl<sub>3</sub>) and the solvent residual peak used as an internal reference. Resonance is reported according to the following convention: chemical shift  $\delta$  in parts per million (ppm), coupling constant  $J$  in Hz if applicable, number of protons assigned to the resonance and structural assignment if possible. Multiplicities are abbreviated as following: singlet (s), doublet (d), triplet (t), quartet (q), quintet (quint), multiplet (m), broad (br). Spectra were evaluated using MestReNova v12.0.1-20560 (MestreLab Research S.L.); assignment of signals was possible with measured 2D spectra (COSY and HSQC), not included. Electrospray ionisation mass spectrometry measurements (ESI-MS) were recorded on a Bruker ApexQe FT-ICR at the Organic Chemistry Institute, Heidelberg.

**(7-(ethylamino)-2-oxo-2H-chromen-4-yl)methyl acetate precursor was synthesized according to literature** <sup>152,202</sup>

### 3.2.2 *Tert*-butyl-*N*-(4-(acetoxymethyl)-2-oxo-2H-chromen-7-yl)-*N*-ethylglycinate



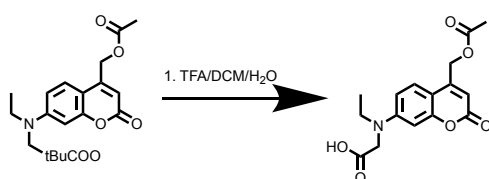
500 mg of (7-(ethylamino)-2-oxo-2H-chromen-4-yl)methyl acetate (382.73  $\mu$ mol, 1 eq) and 57.37 mg sodium iodide (382.73  $\mu$ mol, 1 eq) were dissolved in 25 mL dry DMF with activated molecular sieve (3Å). Then, 730  $\mu$ L *N,N*-Diisopropylethylamine (7.654 mmol, 4 eq) and 2.460  $\mu$ L bromoacetic acid *tert*-butyl ester (9.568 mmol, 5 eq) were

added and refluxed overnight under inert atmosphere. The mixture was cooled down to room temperature and diluted with 100 mL of water and extracted with dichloromethane (3x 70 mL). The combined organic layers were dried over sodium sulfate and the solvents were removed under reduced pressure. Flash chromatography was performed on a 15-35% gradient ethyl acetate/cyclohexane to afford **578 mg (72% Yield)** of a brownish oil.

$^1\text{H}$  NMR (300 MHz, Chloroform-*d*)  $\delta$  7.30 (d,  $J$  = 8.9 Hz, 2H), 6.55 (dd,  $J$  = 8.9, 2.6 Hz, 1H), 6.49 (d,  $J$  = 2.6 Hz, 1H), 6.18 (d,  $J$  = 1.3 Hz, 1H), 5.21 (d,  $J$  = 1.3 Hz, 3H), 3.97 (s, 3H), 3.49 (p,  $J$  = 7.2 Hz, 3H), 2.18 (s, 4H), 1.62 – 1.39 (m, 21H), 1.24 (t,  $J$  = 7.1 Hz, 4H).  $^{13}\text{C}$  NMR (75 MHz,  $\text{cdCl}_3$ )  $\delta$  170.22, 169.05, 161.65, 155.94, 151.02, 149.29, 107.12, 82.33, 77.43, 77.01, 76.59, 61.62, 61.26, 60.44, 53.00, 46.75.

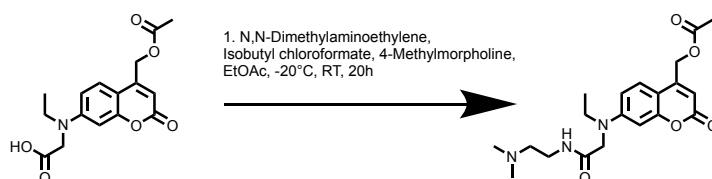
ESI-positive  $m/z$  calculated for  $\text{C}_{20}\text{H}_{25}\text{NO}_6$ : 375.42; found: 376.426  $[\text{M}+\text{H}]^+$ .

### 3.2.3 N-(4-(acetoxymethyl)-2-oxo-2H-chromen-7-yl)-N-ethylglycine



540 mg of *tert*-butyl *N*-(4-(acetoxymethyl)-2-oxo-2*H*-chromen-7-yl)-*N*-ethylglycinate (1.438 mmol, 1 eq) were dissolved in 500  $\mu\text{L}$  dichloromethane, 20  $\mu\text{L}$  of water and 1.5 mL of trifluoroacetic acid (25/2/75). The reaction was stirred at room temperature for 3 hours. Then, Toluene (3x 5 mL) was added and the mixture was concentrated under reduced pressure to azeotropically remove residual trifluoroacetic acid. The product was used without further purification.

### 3.2.4 2-(dimethylamino)ethyl N-(4-(acetoxymethyl)-2-oxo-2H-chromen-7-yl)-N-ethylglycinate

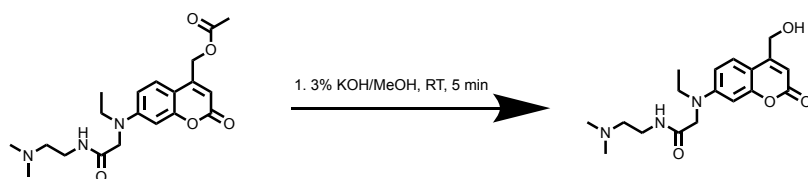


450 mg of *N*-(4-(acetoxymethyl)-2-oxo-2H-chromen-7-yl)-*N*-ethylglycine (1.409 mmol, 1 eq) were dissolved in 15 mL ethyl acetate and cooled to -20 °C under inert atmosphere. To this solution, 598.7 µL *N*-methylmorpholine (5.919 mmol, 3.5 eq) were added followed by dropwise addition of 230.976 µL isobutylchloroformate (1.691 mmol, 1.2 eq) upon which a yellow-white precipitate formed. After 20 minutes, 120.30 µL *N,N*-dimethylaminoethylene (1.691 mmol, 1.2 eq) were added and stirred for 2 hours at -20 °C. Next, the ice bath was removed and the reaction was let to stir at room temperature for 18 hours. The reaction was quenched with 10 mL ethyl acetate, washed with (1x 10 mL) water, 5% citric acid, 5% sat. sodium carbonate. The combined organic layers were dried over sodium sulfate and the solvents were removed under reduced pressure. Flash chromatography was performed on a 5-100% gradient methanol in chloroform to afford **395 mg (72% Yield)** of a dark yellow oil.

<sup>1</sup>H NMR (300 MHz, Chloroform-*d*) δ 7.32 (s, 1H), 7.32 – 7.26 (m, 1H), 7.02 (s, 1H), 6.57 (d, *J* = 8.4 Hz, 2H), 6.17 (d, *J* = 1.3 Hz, 1H), 5.20 (d, *J* = 1.4 Hz, 2H), 3.97 (s, 2H), 3.53 (d, *J* = 7.1 Hz, 2H), 3.38 (d, *J* = 5.8 Hz, 2H), 2.47 (t, *J* = 5.9 Hz, 2H), 2.20 (d, *J* = 12.2 Hz, 9H), 1.23 (t, *J* = 7.1 Hz, 3H). <sup>13</sup>C NMR (75 MHz, cdcl<sub>3</sub>) δ 124.50, 109.48, 107.88, 99.29, 45.01, 44.69, 20.71, 11.80, 0.99.

ESI-positive *m/z* calculated for C<sub>20</sub>H<sub>27</sub>N<sub>3</sub>O<sub>5</sub>: 389.45; found: 390.457 [M+H]<sup>+</sup>.

### 3.2.5 2-(dimethylamino)ethyl *N*-ethyl-*N*-(4-(hydroxymethyl)-2-oxo-2H-chromen-7-yl)glycinate (Lyso-coumarin cage)

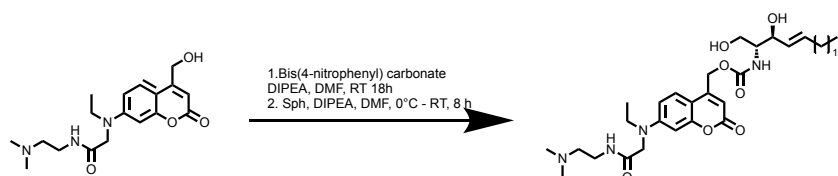


350 mg of 2-(dimethylamino)ethyl *N*-(4-(acetoxymethyl)-2-oxo-2H-chromen-7-yl)-*N*-ethylglycinate (0.898 mmol, 1 eq) were dissolved in 100 mL 3% KOH in MeOH and stirred at room temperature for 5 minutes. The reaction was quenched with 100 mL NH<sub>4</sub>Cl and the mixture extracted with (3x 250 mL) chloroform. The combined organic layers were dried over sodium sulfate and the solvents were removed under reduced pressure. Flash chromatography was performed with CHCl<sub>3</sub>:MeOH:NH<sub>3</sub>(<sub>aq</sub>):H<sub>2</sub>O (22.5:5:0.025:0.25) to afford **245.7 mg (82% Yield)** of a yellow solid.

$^1\text{H}$  NMR (500 MHz, Chloroform-*d*)  $\delta$  7.36 (t,  $J$  = 5.5 Hz, 1H), 7.12 (d,  $J$  = 8.9 Hz, 1H), 6.46 (dd,  $J$  = 8.9, 2.6 Hz, 1H), 6.42 (d,  $J$  = 2.6 Hz, 1H), 6.12 (s, 1H), 4.63 – 4.57 (m, 2H), 4.47 (s, 1H), 3.93 (s, 2H), 3.47 (q,  $J$  = 7.1 Hz, 2H), 3.42 (q,  $J$  = 5.9 Hz, 2H), 2.49 (t,  $J$  = 6.0 Hz, 2H), 2.23 (s, 6H), 1.20 (t,  $J$  = 7.1 Hz, 3H).  $^{13}\text{C}$  NMR (126 MHz, Chloroform-*d*)  $\delta$  169.66, 162.19, 155.39, 155.31, 150.63, 107.77, 60.04, 58.05, 54.56, 46.19, 36.57.

ESI-positive  $m/z$  calculated for  $\text{C}_{18}\text{H}_{25}\text{N}_3\text{O}_4$ : 333.39; found: 334.411  $[\text{M}+\text{H}]^+$ .

### 3.2.6 (7-((2-((2-(dimethylamino)ethyl)amino)-2-oxoethyl)(ethyl)amino)-2-oxo-2*H*-chromen-4-yl)methyl ((2*R*,3*S*,*E*)-1,3-dihydroxyoctadec-4-en-2-yl)carbamate (Lyso-Sph)



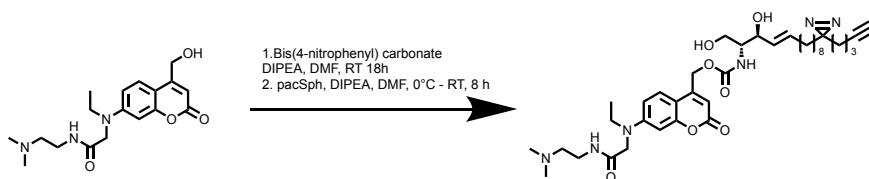
13.7 of **1** (39  $\mu\text{mol}$ , 1.9 eq) were dissolved in 350  $\mu\text{L}$  dry DMF and 10 mg Bis-(4-nitrophenyl) carbonate (33  $\mu\text{mol}$ , 1.6 eq) were dissolved in 500  $\mu\text{L}$  dry DMF and added to the stirred coumarin solution. Next, 17  $\mu\text{L}$  DIPEA (99  $\mu\text{mol}$ , 5 eq) were added dropwise under light protection and stirred overnight. The crude reaction was cooled to 0  $^\circ\text{C}$  under stirring, then 6 mg sphingosine (20  $\mu\text{mol}$ , 1 eq) were dissolved in 1 mL dry DMF, 7  $\mu\text{L}$  DIPEA (40  $\mu\text{mol}$ , 2 eq) were added and pre-cooled to 0  $^\circ\text{C}$ , then added dropwise to the cold stirred coumarin solution. The reaction was stirred at 0  $^\circ\text{C}$  for 1h, then allowed to warm to room temperature and stirred for additional 5h, until TLC showed full consumption of sphingosine. Solvents were removed *in vacuo* and the crude product was purified by flash chromatography using  $\text{CHCl}_3/\text{MeOH}$  (10-70%) with 0.1%  $\text{NH}_3(\text{aq})/\text{H}_2\text{O}$  (v/v) as additive. Fractions containing pure product were combined and concentrated to afford **10.4 mg (78% yield)** of **2** as a yellow oil.

$^1\text{H}$  NMR (500 MHz, Chloroform-*d*)  $\delta$  8.16 (t, 3JHH = 6 Hz, 1H, OCN-43H), 7.22 (d, 3JHH = 8.9 Hz, 1H, C-6H), 6.60 (dd, 3JHH = 9 Hz, 4JHH = 2 Hz, 1H, Car-1H), 6.50 (d, 3JHH = 8.3 Hz, 1H, OCON-16H), 6.40 (d, 4JHH = 2 Hz, 1H, C-3H), 6.11 (s, 1H, C-9H), 5.80 (dt, 3JHH = 14.6 Hz, 3JHH = 7.3 Hz, 1H, C-23H), 5.55 (dd, 3JHH = 15.3 Hz, 3JHH = 5.8 Hz, 1H, C-22H), 5.14 (d, 2JHH = 16 Hz, 1H, C-12H $\alpha$ ), 5.08 (d, 2JHH = 16Hz, 1H, C-12H $\beta$ ), 4.39 (s, br, 1H, C-20H), 4.05 (s, 2H, C-26H $_2$ ), 3.98 (dd, 2JHH =

11.6 Hz, 3JHH = 3.7 Hz, 1H, C-18H $\alpha$ ), 3.74 – 3.66 (m, 4H, C-18H $\beta$ , C-44H<sub>2</sub>, C-17H), 3.61 (q, 3JHH = 7 Hz, 2H, C-28H<sub>2</sub>), 3.22 (t, 3JHH = 5 Hz, 2H, C-45H<sub>2</sub>), 2.84 (s, 6H, C-47/48H<sub>3</sub>), 2.05 (q, 3JHH = 7 Hz, 2H, C-24H<sub>2</sub>), 1.20 -1.40 (m, C-29-39H<sub>2</sub>, 22H), 1.19 (t, 3JHH = 7.1 Hz, 3H, C-41H<sub>3</sub>), 0.87 (t, 3JHH = 6.9 Hz, 3H, C-40H<sub>3</sub>). Due to their amphiphilic nature and the low amount of material, <sup>13</sup>C NMR spectra of Lyso-Sph could not be accurately described.

ESI-positive m/z calculated for C<sub>46</sub>H<sub>69</sub>N<sub>3</sub>O<sub>6</sub>: 673.4535; found: 673.4543 [M+H]<sup>+</sup>.

### 3.2.7 (7-((2-((2-(dimethylamino)ethyl)amino)-2-oxoethyl)(ethyl)amino)-2-oxo-2H-chromen-4-yl)methyl ((2R,3S,E)-1,3-dihydroxy-13-(3-(pent-4-yn-1-yl)-3H-diazirin-3-yl)tridec-4-en-2-yl)carbamate (Lyso-pacSph) final synthetic procedure performed by Judith Notbohm

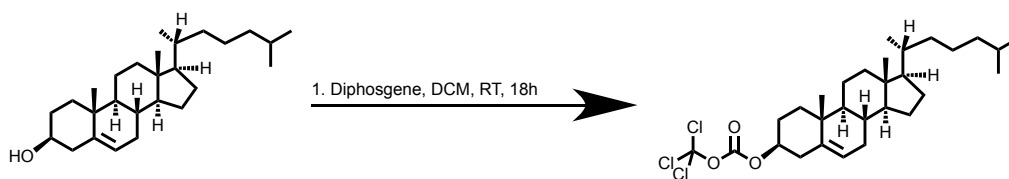


13.8 mg of **1** (40  $\mu$ mol, 1.9 eq) were dissolved in 500  $\mu$ L dry DMF and 10.2 mg Bis-(4-nitrophenyl) carbonate (34  $\mu$ mol, 1 eq) were dissolved in 500  $\mu$ L dry DMF and added to the stirred coumarin solution. Next, 17.5  $\mu$ L DIPEA (101  $\mu$ mol, 5 eq) were added dropwise under light protection and stirred overnight. The crude reaction was cooled to 0 °C under stirring, then 7 mg Photoclick Sphingosine (21  $\mu$ mol, 1 eq) were dissolved in 1 mL dry DMF, pre-cooled to 0 °C and added dropwise to the cold stirred coumarin solution. The reaction was stirred at 0 °C for 1h, then allowed to warm to room temperature and stirred for additional 8h, until TLC showed full consumption of Photoclick Sphingosine. Solvents were removed *in vacuo* and the crude product was purified 2x by flash chromatography using CHCl<sub>3</sub>/MeOH (10-70%) with 0.1% NH<sub>3(aquo)</sub>/H<sub>2</sub>O (v/v) as additive to afford 6.9 mg of pure **3**, **15.5 mg (99% yield)**

<sup>1</sup>H NMR (500 MHz, Chloroform-*d*)  $\delta$  8.16 (t, 3JHH = 5 Hz, 1H, OCN-43H), 7.22 (d, 3JHH = 9 Hz, 1H, C-6H), 6.60 (dd, 3JHH = 9.1, 4JHH = 2.1 Hz, 1H, C-1H), 6.52 (d, 3JHH = 8.7 Hz, 1H, OCONH), 6.39 (d, 4JHH = 1.5 Hz, 1H, C-3H), 6.12 (s, 1H, C-9H), 5.80 (dt, 3JHH = 14.4, 3JHH = 6.8 Hz, 1H, C-26H), 5.54 (dd, 3JHH = 15.4, 3JHH = 6.0 Hz,

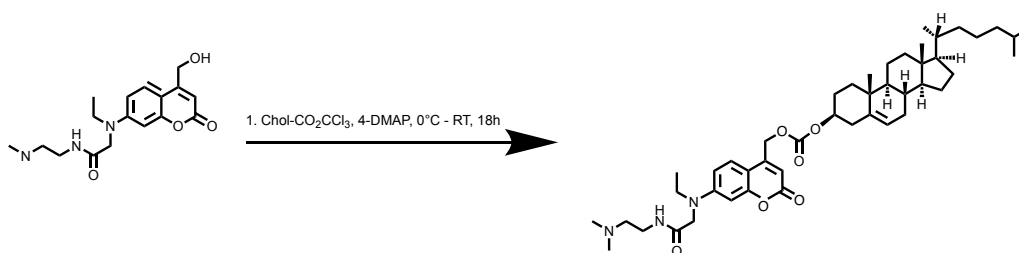
1H, C- 25H), 5.14 (d, 2JHH = 16 Hz, 1H, C-12H $\alpha$ ), 5.09(d, 2JHH = 16 Hz, 1H, C-12H $\beta$ ), 4.39 (s, br, 1H, C-23H), 4.05 (s, 2H, C-15H<sub>2</sub>), 3.97 (dd, 2JHH = 10.9, 3JHH = 4.5 Hz, 1H, C-20H $\alpha$ ), 3.77-3.72 (m, 3H, C-20H $\beta$ , C- 44H<sub>2</sub>), 3.67 (m, 1H, C-21H), 3.62 (q, 3JHH = 7.1 Hz, 2H, C-16H<sub>2</sub>), 3.24 (t, 3JHH = 5 Hz, 2H, C-45H<sub>2</sub>), 2.86 (s, 6H, C-47/48H<sub>3</sub>), 2.15 (td, 3JHH = 7 Hz, 4JHH = 2.5 Hz, 2H, C-38H<sub>2</sub>), 2.05 (q, 3JHH = 7 Hz, 2H, C- 27H<sub>2</sub>), 1.95 (t, 4JHH = 2.5 Hz, 1H, C-51H), 1.50 – 1.46 (m, 2H, C-36H<sub>2</sub>), 1.30 – 1.38 (m, 6H, C-37H<sub>2</sub>, C-28H<sub>2</sub>; C-34H<sub>2</sub>), 1.17 – 1.27 (m, 11H, C-29H<sub>2</sub> – C-33H<sub>2</sub>, C-40H<sub>3</sub>), 1.06 (m, 2H, C-XH<sub>2</sub>). Due to their amphiphilic nature and the low amount of material, <sup>13</sup>C NMR spectra of Lyso-pacSph could not be accurately described. ESI-positive m/z calculated for C<sub>37</sub>H<sub>60</sub>N<sub>4</sub>O<sub>7</sub>: 709.4283; found: 709.4297 [M+H]<sup>+</sup>.

**3.2.8 (3S,8S,9S,10R,13R,14S,17R)-10,13-dimethyl-17-((R)-6-methylheptan-2-yl)-2,3,4,7,8,9,10,11,12,13,14,15,16,17-tetradecahydro-1H-cyclopenta[a]phenanthren-3-yl (trichloromethyl) carbonate**



10 mg of cholesterol (25.862  $\mu$ mol, 1 eq) were dissolved in 1 mL dry DCM under an inert argon atmosphere. After 5 minutes, 8.38  $\mu$ L diphosgene (25.862  $\mu$ mol, 1 eq) were added dropwise. Next, 3.31 mg of 4-DMAP (27.256  $\mu$ mol, 1.05 eq) were added and stirred overnight. Solvents were removed *in vacuo* and the crude was used without further purification.

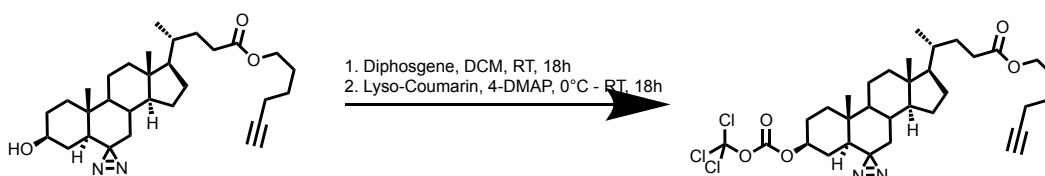
**3.2.9 (3S,8S,9S,10R,13R,14S,17R)-10,13-dimethyl-17-((R)-6-methylheptan-2-yl)-2,3,4,7,8,9,10,11,12,13,14,15,16,17-tetradecahydro-1H-cyclopenta[a]phenanthren-3-yl ((7-((2-((2-(dimethylamino)ethyl)amino)-2-oxoethyl)(ethyl)amino)-2-oxo-2H-chromen-4-yl)methyl) carbonate (Lyso-Chol)**



8.46 mg of *N*-(2-(dimethylamino)ethyl)-2-(ethyl(4-(hydroxymethyl)-2-oxo-2*H*-chromen-7-yl)amino)acetamide (24.379  $\mu\text{mol}$ , 1 eq) were dissolved in 500  $\mu\text{L}$  dry DCM and placed on an ice bath. Then 11 mg of cholesterol chloroformate (**6**) (24.492  $\mu\text{mol}$ , 1.05 eq) was dissolved in 500  $\mu\text{L}$  dry DCM and added dropwise to the cold stirred coumarin solution, then 3 mg of 4-DMAP (24.492  $\mu\text{mol}$ , 1.05 eq) was added. The flask was sealed and filled with argon and stirred overnight. The crude product was purified by flash chromatography using  $\text{CHCl}_3:\text{MeOH}:\text{NH}_3(\text{aq}):\text{H}_2\text{O}$  (22.5:2.5:0.025:0.0125), to afford **16.2 mg (87% Yield)** of a greenish oil.

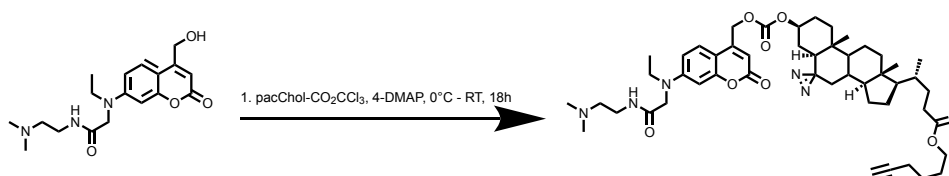
$^1\text{H}$  NMR (500 MHz, Chloroform-*d*)  $\delta$  8.23 (t,  $J$  = 6.0 Hz, 1H), 7.32 (d,  $J$  = 9.0 Hz, 1H), 6.68 (dt,  $J$  = 9.1, 2.5 Hz, 1H), 6.49 (t,  $J$  = 2.0 Hz, 1H), 6.19 (d,  $J$  = 1.3 Hz, 1H), 5.41 (d,  $J$  = 4.8 Hz, 1H), 5.24 (d,  $J$  = 1.3 Hz, 2H), 4.57 – 4.47 (m, 1H), 4.07 (d,  $J$  = 2.3 Hz, 2H), 3.75 – 3.62 (m, 4H), 3.17 (q,  $J$  = 5.2 Hz, 2H), 2.88 – 2.82 (m, 4H), 2.80 (d,  $J$  = 3.0 Hz, 1H), 2.46 – 2.36 (m, 2H), 2.05 – 1.93 (m, 3H), 1.90 (dt,  $J$  = 13.5, 3.6 Hz, 1H), 1.82 (ddd,  $J$  = 13.2, 9.5, 6.0 Hz, 1H), 1.69 (ddd,  $J$  = 14.4, 12.2, 3.8 Hz, 2H), 1.62 – 1.40 (m, 9H), 1.40 – 1.29 (m, 4H), 1.25 – 1.18 (m, 5H), 1.14 – 1.11 (m, 3H), 1.02 (s, 5H), 0.89 – 0.79 (m, 13H), 0.68 (s, 3H).  $^{13}\text{C}$  NMR (126 MHz, Chloroform-*d*)  $\delta$  170.21, 161.41, 154.00, 150.99, 148.97, 139.12, 107.25, 64.20, 58.38, 54.47, 46.97, 42.32, 39.71, 39.51, 37.96, 36.82, 36.54, 36.18, 34.57, 31.91, 28.22, 27.66, 24.28, 23.82, 21.05. ESI-positive  $m/z$  calculated for  $\text{C}_{46}\text{H}_{69}\text{N}_3\text{O}_6$ : 759.52; found: 760.5265 [ $\text{M}+\text{H}$ ] $^+$ .

**3.2.10 hex-5-yn-1-yl (4*R*)-4-((3*S*,5*S*,10*R*,13*R*,14*S*,17*R*)-10,13-dimethyl-3-(((trichloromethoxy)carbonyl)oxy)-1,2,3,4,5,7,8,9,10,11,12,13,14,15,16,17-hexadecahydrospiro[cyclopenta[*a*]phenanthrene-6,3'-diazirin]-17-yl)pentanoate**



10 mg Photo-reactive Clickable trans-Sterol probe (20.716  $\mu\text{mol}$ , 1 eq) were dissolved in 1 mL dry DCM under argon atmosphere. After 5 minutes, 6.9  $\mu\text{L}$  diphosgene (21.33  $\mu\text{mol}$ , 1.03 eq) were added dropwise. Next, 2.65 mg 4-DMAP (21.75  $\mu\text{mol}$ , 1.05 eq) were added and stirred overnight. Solvents were removed *in vacuo* and the crude was used without further purification.

**3.2.11 Hex-5-yn-1-yl (4R)-4-((3S,5S,10R,13R,14S,17R)-3-(((7-((2-((2-(dimethylamino) ethyl)amino)-2-oxoethyl)(ethyl)amino)-2-oxo-2H-chromen-4-yl)methoxy)carbonyl)oxy)-10,13-dimethyl-1,2,3,4,5,7,8,9,10,11,12,13,14,15,16,17-hexadecahydrospiro[cyclopenta[a]phenanthrene-6,3'-diazirin]-17-yl)pentanoate (Lyso-pacChol)**



6.85 mg of **1** (19.725  $\mu\text{mol}$ , 1 eq) were dissolved in 500  $\mu\text{L}$  dry DCM and placed in an ice bath. Then 11.29 mg pacChol-chloroformate (20.70  $\mu\text{mol}$ , 1.05 eq) was dissolved in 500  $\mu\text{L}$  dry DCM and added dropwise to the cold stirred coumarin solution, then 2.53 mg 4-DMAP (20.70  $\mu\text{mol}$ , 1.05 eq) was added. The flask was sealed, filled with argon and stirred overnight at room temperature. Solvents were removed *in vacuo* and the crude product was purified by flash chromatography using CHCl<sub>3</sub>/MeOH/NH<sub>3(aquo)</sub>/H<sub>2</sub>O (22.5:2.5:0.025:0.0125), to afford **13.5 mg (96%)** of **4** as a greenish oil.

<sup>1</sup>H NMR (500 MHz, Chloroform-d)  $\delta$  8.23 (t, J = 5.9 Hz, 1H), 7.30 (d, J = 9.0 Hz, 1H), 6.68 (dd, J = 9.0, 2.6 Hz, 1H), 6.50 (d, J = 2.6 Hz, 1H), 6.14 (d, J = 1.4 Hz, 1H), 5.23 – 5.14 (m, 2H), 4.47 (dt, J = 11.5, 6.4 Hz, 1H), 4.09 – 4.06 (m, 4H), 3.76 – 3.63 (m, 4H), 3.17 (t, J = 5.3 Hz, 2H), 2.83 (d, J = 4.8 Hz, 6H), 2.36 – 2.30 (m, 1H), 2.23 (d, J

= 2.7 Hz, 2H), 2.05 – 1.97 (m, 2H), 1.95 (t, J = 2.6 Hz, 1H), 1.81 – 1.72 (m, 8H), 1.69 (s, 6H), 1.60 (d, J = 7.8 Hz, 2H), 1.42 (s, 1H), 1.21 (s, 1H), 1.16 (d, J = 2.1 Hz, 4H), 0.92 (d, J = 6.5 Hz, 6H), 0.83 (d, J = 9.2 Hz, 1H), 0.69 (s, 4H), 0.60 (d, J = 12.3 Hz, 2H), 0.42 (dd, J = 13.9, 4.6 Hz, 2H). Due to their amphiphilic nature and the low amount of material, <sup>13</sup>C NMR spectra of Lyso-pacChol could not be accurately described.

ESI-positive m/z calculated for C<sub>46</sub>H<sub>69</sub>N<sub>5</sub>O<sub>8</sub>: 855.5146 ; found: 856.5215 [M+H]<sup>+</sup>.

### 3.3 Buffers and solutions

#### **PBS**

##### **10x stock**

10 mM Na<sub>2</sub>HPO<sub>4</sub>

2 mM KH<sub>2</sub>PO<sub>4</sub>

137 mM NaCl

2.7 mM KCl

1 mM EDTA

All chemicals were dissolved in ddH<sub>2</sub>O, pH adjusted to 7.4 using HCl, filtered and sterilized. PBS was prepared at the BZH.

#### **Imaging buffer**

20 mM HEPES

115 mM NaCl

1.8 mM CaCl<sub>2</sub>

1.2 mM MgCl<sub>2</sub>

1.2 mM KH<sub>2</sub>PO<sub>4</sub>

0.2% Glucose (w/v)

All chemicals were dissolved in ddH<sub>2</sub>O, pH adjusted to 7.4 using HCl or NaOH, filtered and stored at 4 °C.

## **Lysis buffer**

0.1% SDS

1% Triton

1x Protease inhibitor

SDS + Triton containing aliquots were prepared and stored at -20 °C. Protease inhibitor was taken from a 100x aliquot and added fresh at the beginning of each experiment.

## **Amido black**

50% H<sub>2</sub>O (v/v)

40% MeOH (v/v)

10% AcOH (v/v)

0.02% Amido black (w/v)

## **3.4 Cell culture**

### **Eukaryotic cell lines**

**HeLa WT** (Human cervical adenocarcinoma cells, No. CCL2)

**HeLa NPC1** (NPC1 null human cervical adenocarcinoma cell)

Dr. Wim Annaert (VIB-KU Leuven Center for Brain & Disease Research, Leuven, BE)

**HeLa SK1/SK2 dKO** (Sphingosine kinase 1 and 2 null human adenocarcinoma cell)

Prof. Dr. Sarah Spiegel (Department of Biochemistry and Molecular Biology at Virginia Commonwealth University, Virginia, USA)

**HeLa SGPL1** (SGPL1 null human cervical adenocarcinoma cell)

Prof. Dr. Britta Brügger (Heidelberg University Biochemistry Centre, Heidelberg, DE)

**HeLa LIMP2** (LIMP2 null human cervical adenocarcinoma cell)

Prof. Dr. Paul Saftig (Unit of Molecular Cell Biology and Transgenic Research  
University of Kiel, Kiel, DE)

All cells were grown in (complete medium) Dulbecco's Modified Eagle's Medium (DMEM) (4500 mg/L glucose, L-glutamine, sodium bicarbonate, without sodium pyruvate, Sigma Aldrich) supplemented with 10% FCS (Bio&Sell), 1% penicillin/streptomycin (Biowest) at 37°C in 5% CO<sub>2</sub> atmosphere and passaged 2-3 times per week. Cells were seeded into appropriated experimental dishes at least 24h prior to the experiment.

### **3.5 Lipid analyses by thin-layer chromatography**

TLC procedure adapted from<sup>153,264</sup>

#### **3.5.1 TLC analysis of Lyso-pacSph**

Cells were grown in 6-well plates (CellStar, greiner bio-one) to 70-85% confluency and labeled with 10 μM Lyso-pacSph in DMEM medium for 1h, washed twice with PBS and chased overnight in DMEM medium. Cells were washed with PBS, overlaid with 500 μL of ice-cold imaging buffer and UV-irradiated on ice for 90s with a NailStar Professional LED lamp. Cells were either incubated further for indicated times in DMEM medium or collected directly. After uncaging and chasing for desired times, cells were washed with 1x PBS and air dried for 5 s. Then, 500 μL of MeOH/CHCl<sub>3</sub> (5:1) were added in one add. 6-well plate was placed into a bath-like sonicator for 60 s at RT (Frequency: 37, Power: 100, Sweep), detached cells were collected and transferred to a 1.5 mL tube. After transfer, cells were lysed by centrifugation (20000 rpm, 5min) and the supernatant was decanted into a fresh 2 mL tube. 400 μL CHCl<sub>3</sub> and 600 μL 0.1% AcOH (v/v) were added, the mixture was vortexed, centrifuged

(20000 rpm, 5min) and the aqueous upper phase was discarded. The remaining organic phase was transferred into a 1.5 mL tube and dried in a speed-vac (45°C, 20 min). The lipids were dissolved in 30  $\mu$ L click mix reaction (0.6  $\mu$ L, 44.4 mM 3-azido-7-hydroxycoumarin, 125  $\mu$ L, 10 mM Cu(I)BF<sub>4</sub> dissolved in ACN and 0.5 mL EtOH). Copper-catalysed azide-alkyne cycloaddition was performed in a speed-vac (45°C, 20 min). Click lipids were dissolved in 15  $\mu$ L EtOH/ACN (5:1) and applied to a 10 x 20 cm TLC silica gel 60 aluminum plate. TLC plates were developed using CHCl<sub>3</sub>/MeOH/H<sub>2</sub>O/AcOH (65:25:4:1) for 5 cm, dried for 30 minutes and then Cyh/EtOAc (1:1) for 9 cm. Lipids containing the fluorescent coumarin group were visualised by UV light using a gel-doc system. Quantification of extracted lipids was performed by determining the total intensity of each band in ImageJ. The raw integrated density of an equal rectangular ROI was measured for each lipid species and corrected for background via an identical, blank adjacent ROI.

### **3.5.2 TLC analysis of Lyso-pacChol**

Cells were grown in 12-well plates (CellStar, greiner bio-one) to 70-85% confluency and labeled with 10  $\mu$ M Lyso-pacChol in DMEM medium for 45 min, washed twice with PBS and chased overnight in DMEM medium. Cells were washed, overlaid with 500  $\mu$ L of ice-cold imaging buffer and UV-irradiated on ice for 90s with a NailStar Professional LED lamp. Cells were either incubated further for indicated times in DMEM medium or directly trypsinised and transferred to a 1.5 mL tube. After transfer, cells were pelleted by centrifugation (1500 rpm, 5min) and the supernatant was discarded. The cell pellet was resuspended in 300  $\mu$ L of PBS and mixed with 600  $\mu$ L MeOH and 150  $\mu$ L CHCl<sub>3</sub> to precipitate proteins and DNA. The mixture was vortexed and centrifuged (14000 rpm, 5 min) and the lipid containing supernatant transferred to a 2 mL tube; the protein pellet was stored at 4°C and used for protein determination with amido black. 300  $\mu$ L CHCl<sub>3</sub> and 600  $\mu$ L 0.9% NaCl (w/v) were added, the mixture was vortexed, centrifuged (14000 rpm, 5min) and the aqueous upper phase was discarded. The organic phase was transferred into a 1.5 mL tube and dried in a speed-vac (30°C, 20 min). The lipids were dissolved in 30  $\mu$ L click mix reaction (0.6  $\mu$ L, 44.4 mM 3-azido-7-hydroxycoumarin, 125  $\mu$ L, 10 mM Cu(I)BF<sub>4</sub> dissolved in ACN and 0.5

mL EtOH). Copper-catalysed azide-alkyne cycloaddition was performed in a speed-vac (45°C, 20 min). Click lipids were dissolved in 15  $\mu$ L EtOH/ACN (5:1) and applied on a 14 x 20 cm TLC silica gel 60 aluminum plate. TLC plates were developed using CHCl<sub>3</sub>/MeOH/H<sub>2</sub>O/AcOH (65:25:4:1) for 2 cm, dried for 30 minutes and then Cy/EtOAc (2:1) for 13 cm. Lipids containing the fluorescent coumarin group were visualised by UV light using a gel-doc system. Quantification of extracted lipids was performed by determining the total intensity of each band in ImageJ. The raw integrated density of an equal rectangular ROI was measured for each lipid species and corrected for background via an identical, blank adjacent ROI.

## **3.6 Confocal microscopy**

### **3.6.1 Live cell microscopy of lysosome-targeted compounds**

For co-localisation analysis and assessment of compound uptake, cells were grown in 8-well  $\mu$ -slides (ibidi) to 50-70% confluency. Cells were labeled with 200  $\mu$ L of lyso-pacSph or lyso-pacChol (750 nM - 10  $\mu$ M) up to 1h, imaged immediately or chased for indicated times. Prior to imaging, cells were washed and overlaid with 200  $\mu$ L imaging buffer. For co-localisation analysis, lysosomes were stained by incubating cells with 200  $\mu$ L of 100 nM LysoTracker Red DND-99 (Thermo Fisher Scientific) in DMEM for 15 min, washed twice with PBS and further incubated for 15 min at 37°C. Prior to imaging, cells were washed and overlaid with 200  $\mu$ L imaging buffer. Cells were imaged using a confocal laser scanning microscope (Zeiss LSM800) with a 63x oil objective.

### **3.6.2 Calcium studies with lyso-probes**

Visualization of changes in intracellular Ca<sup>2+</sup> were performed on a Zeiss LSM 800 confocal microscope, with a baseline of 3 s before uncaging with a LED 385 nm laser, 30% power in a circular area, and visualization of Fluo-4 AM was performed with a 561 nm laser. Images were acquired every 2s and monitored any changes in fluorescence. Time-lapse images were analyzed using Fiji software with the FluoQ macro<sup>265</sup> set to the following parameters:

Background subtraction method: Mean of an interactively selected ROI  
 Noise reduction/smoothing method: None  
 Threshold method: Interactively with ImageJ's built-in threshold window  
 ROI segmentation: Semi-automatically with binary mask modification  
 Calculate amplitude changes: Using maximum observed amplitude change

### 3.6.2 Visualization of time-resolved subcellular localization of lysosome-targeted compounds

Cells were seeded onto 11-mm glass coverslips (Thermo Scientific) in 24-well plates (CellStar, greiner bio-one) to 70-85% confluency, labeled with 10  $\mu$ M Lyso-pacSph or Lyso-pacChol for 1h and 45 min respectively, washed twice in PBS and chased overnight in complete DMEM medium. Cells were washed, overlaid with 350  $\mu$ L of ice-cold imaging buffer and UV-irradiated on ice for 90s with a NailStar Professional LED lamp, either followed by a second UV-irradiation at 365 nm with a UVP Blak-Ray B100-AP High Intensity lamp 7 min or chased for second time and UV-irradiated after desired timepoints. For 0' timepoint, cells were immediately irradiated for 7 min at 365 nm with a UVP Blak-Ray B100-AP High Intensity lamp.

#### 3.6.2.1 Visualization of Lyso-pacSph

Cells were fixed with -20°C Methanol for 20 min at -20°C, washed three times with CHCl<sub>3</sub>/MeOH/AcOH (10:55:0.75) then washed two times in PBS. Crosslinked protein-lipid complexes were labelled with AlexaFluor 594 picolyl azide (Jena Bioscience) using a CuAAC-based click chemistry reaction buffer kit according to the manufacturer's instructions (Jena Bioscience) and subjected to immunofluorescence experiments. Microscopy images were acquired using a confocal laser scanning microscope (Zeiss LSM800) with a 63x oil objective, settings as following:

Channel	Pinhole	Laser power	NA	Gain	Digital gain	Stain
488	2.04 AU / 90 $\mu$ m	0.2%	1.4	625	1	LE/LY

594	1.70 AU / 90 $\mu$ m	2.5%	1.4	670	1	Lipid
647	1.17 AU / 66 $\mu$ m	3.5%	1.4	650	1	Golgi

Images were further analysed using ImageJ 2.1.0/1.53c. The Pearson coefficient for analysis of signal distribution within cells and lysosomes were extracted from the raw images with Coloc2 plugin.

### 3.6.2.2 Visualization of Lyso-pacChol

Cells were fixed with 4% PFA and 0.1% glyoxal in PBS for 30 min at room temperature, washed three times in PBS, solubilized with 0.3% Triton/SDS in PBS for 15 min, shaking 350 rpm, RT (using a Thermomixer). Then, washed two times with PBS and blocked for 1h with 2% BSA in PBS. Crosslinked protein-lipid complexes were labelled with AlexaFluor 488 picolyl azide (Jena Bioscience) using a CuAAC-based click chemistry reaction buffer kit according to the manufacturer's instructions (Jena Bioscience) and subjected to immunofluorescence experiments. Before mounting, cells were washed for 30 min with 2% BSA in PBS at RT. Microscopy images were acquired using a confocal laser scanning microscope (Zeiss LSM800) with a 63x oil objective, settings as following:

Channel	Pinhole	Laser power	NA	Gain	Digital gain	Stain
488	1.00 AU / 44 $\mu$ m	1.5%	1.4	650	1	Lipid
594	0.87 AU / 44 $\mu$ m	2.5%	1.4	750	1	LE/LY
594	0.80 AU / 45 $\mu$ m	3.5%	1.4	700	1	Golgi
647	0.88 AU / 45 $\mu$ m	2.0%	1.4	700	1	LD

Images were further analysed using ImageJ 2.1.0/1.53c. The Pearson coefficient for analysis of signal distribution within cells and lysosomes were extracted from the raw images with Coloc2 plugin.

### 3.6.2.3 Immunofluorescence of fixed cells

After fixation, cells were stained with a 200-fold diluted antibodies (rabbit  $\alpha$ -LAMP1, Cell signaling technology, mouse  $\alpha$ -KDEL, Enzo life sciences, rabbit  $\alpha$ -Perilipin 3, Abcam) in 1% BSA, 0.3% Triton in PBS overnight at 4°C, washed two times with PBS

and incubated with a 800-fold diluted antibodies (Alexa Fluor 488  $\alpha$ -rabbit, Alexa Fluor 594  $\alpha$ -rabbit or Alexa Fluor 647  $\alpha$ -mouse, Cell signaling). After washing two times with PBS and H<sub>2</sub>O, stained coverslips were mounted with ProLong Gold Antifade Mountant (Thermo Fisher).

### **3.6.3 Starvation assay**

Cells were seeded onto 11-mm glass coverslips (Thermo Scientific) in 24-well plates (CellStar, greiner bio-one) to 70-85% confluency. Labeled with Lyso-pacSph (1.25  $\mu$ M) and Lyso-Chol (25  $\mu$ M) or Lyso-pacChol (750 nM) and Lyso-Sph (15  $\mu$ M), washed twice in PBS and chased overnight in DMEM medium. Cells were washed, overlaid with 350  $\mu$ L of ice-cold imaging buffer and UV-irradiated on ice for 90s with a NailStar Professional LED lamp, either followed by a second UV-irradiation at 365 nm with a UVP Blak-Ray B100-AP High Intensity lamp 7 min or chased for second time and UV-irradiated after desired timepoints. Cells were fixed with -20°C Methanol for 20 min at -20°C, washed three times with CHCl<sub>3</sub>/MeOH/AcOH (10:55:0.75) then washed two times in PBS. Crosslinked protein-lipid complexes were labelled with AlexaFluor 594 picolyl azide (Jena Bioscience) using a CuAAC-based click chemistry reaction buffer kit according to the manufacturer's instructions (Jena Bioscience) and subjected to immunofluorescence experiments. Microscopy images were acquired using a confocal laser scanning microscope (Zeiss LSM800) with a 63x oil objective. Images were further analyzed using ImageJ 2.1.0/1.53c. The Pearson coefficient for analysis of signal distribution within cells and lysosomes were extracted from the raw images with Coloc2 plugin.

### **3.6.4 NPC1-like induced assay**

Cells were seeded onto 11-mm glass coverslips (Thermo Scientific) in 24-well plates (CellStar, greiner bio-one) to 70-85% confluency. Labeled with Lyso-pacSph (1.25  $\mu$ M) and Lyso-Chol (25  $\mu$ M) or Lyso-pacChol (750 nM) and Lyso-Sph (15  $\mu$ M), washed twice in PBS and chased overnight in DMEM medium. Cells were washed, overlaid with 350  $\mu$ L of ice-cold imaging buffer and UV-irradiated on ice for 90s with a NailStar Professional LED lamp, either followed by a second UV-irradiation at 365 nm with a UVP Blak-Ray B100-AP High Intensity lamp 7 min or chased for second time and UV-

irradiated after desired timepoints. Cells were fixed with -20°C Methanol for 20 min at -20°C, washed three times with CHCl<sub>3</sub>/MeOH/AcOH (10:55:0.75) then washed two times in PBS. Crosslinked protein-lipid complexes were labelled with AlexaFluor 594 picolyl azide (Jena Bioscience) using a CuAAC-based click chemistry reaction buffer kit according to the manufacturer's instructions (Jena Bioscience) and subjected to immunofluorescence experiments. Microscopy images were acquired using a confocal laser scanning microscope (Zeiss LSM800) with a 63x oil objective. Images were further analyzed using ImageJ 2.1.0/1.53c. The Pearson coefficient for analysis of signal distribution within cells and lysosomes were extracted from the raw images with Coloc2 plugin.

## **3.7 Streptavidin Pull Down assay**

### **3.7.1 Cell Labelling and Crosslinking**

Cells were grown in 10 cm plates (CellStar, greiner bio-one) until 95% confluent; for low probe concentration experiments 2 plates per condition were utilized and cell pellets combined. Cells were labeled at the indicated concentrations in complete medium and for the indicated times shown below. After labelling, cells were washed twice with PBS, complete medium was added and cells incubated at 37°C for the specified chase times. Cells were overlaid with cold imaging buffer and cells labelled with a lysosome-targeted probe were UV irradiated at 405 nm with a NailStar Professional LED lamp for 90s, then immediately UV-irradiated at 365 nm with a UVP Blak-Ray B100-AP High Intensity lamp for 7 minutes at 4°C and directly UV irradiated at 365 nm for 10 minutes. Cells were trypsinised and collected in 15 mL cold PBS, centrifuged at 1200 g for 5 minutes at 4°C, then resuspended in 1 mL cold PBS and centrifuged at 1500 g for 5 minutes at 4°C. Supernatant was removed and the cell pellet resuspended in 100 – 300 µL lysis buffer (0.1 % SDS, 1 % Triton in PBS) depending on the cell pellet size. Cells were incubated at 4°C for 30 minutes, then sonicated with a BioRuptor (Diagenode) (3 cycles, 10 s pulse, high intensity, 45 s pause), then incubated at 4 °C for further 1 hour under rotation. The lysate was centrifuged at 14 000 g for 5 min at 4°C and the supernatant collected and stored at 4°C until further use.

For lysates, cells were grown in 10 cm plates (CellStar, greiner bio-one) until 95% confluent; 2 plates per condition were utilized and cell pellets combined. Cells were trypsinised and collected in 15 mL cold PBS, centrifuged at 1200 g for 5 minutes at 4°C, then resuspended in 1 mL cold PBS and centrifuged at 1500 g for 5 minutes at 4°C. Supernatant was removed and the cell pellet resuspended in 200 µL lysis buffer (0.1 % SDS, 1 % Triton in PBS) after lysis, samples were prepared with 200 µg protein and incubated with 50 mM pacSph and either Sph or Chol from concentrations 250 µM to 2.5 mM and incubated in the dark for 1 hour. Next, samples were placed in a bucket with ice and UV irradiated for 8 minutes and followed by streptavidin pulldown protocol.

<b>Probe</b>	<b>Concentration</b>	<b>Pulse time</b>	<b>Chase time</b>
Lyso-pacSph	5 µM	60 min	16 hours
Lyso-pacChol	10 µM	60 min	16 hours
Lyso-pacChol (competition)	750 nM	60 min	16 hours
Lyso-pacSph (competition)	1.25 µM	60 min	16 hours
pacSph (lysates)	50 µM	60 min	

### **3.7.2 Protein determination using Amido Black**

Protein pellets were dissolved in 400 µL of a master mix (2% SDS, 1 µL DNase in 4 mL PBS) vortexed, incubated and mixed (350 rpm, 37°C) for 30 min, then sonicated (37 kHz, 37°C) for additional 30 min. Then, 20 µL were added into a new tube and a serial dilution of BSA was prepared with 0, 25, 50, 75 and 100 µg BSA in 100 µL of water. All samples were diluted to 100 µL. To all samples, 400 µL of amido black solution was added, vortexed, incubated at room temperature for 5 min, and centrifuged (14000 rpm, 5 min). The supernatant was discarded and the pellets were washed twice with 500 µL MeOH/AcOH (10:1). The pellets were dissolved in 300 µL 0.1 N NaOH, and 150 µL were spotted onto a 96-well plate. Absorbance was measured at 550 nm on a SpectraMax M5 microplate reader (Molecular Devices).

### 3.7.3 Biotinylation and protein precipitation

The volume of the lysate was adjusted to 100 µg protein for western blot analysis and diluted with lysis buffer to 100 µL. Then, 7 µL of click mix (see below) was added to each sample and shaken at 37°C for 1 hour.

	Final concentration	Volume [µL]
		For 100 µL
1)CuSO <sub>4</sub> (50mM in H <sub>2</sub> O)	500 µM	1
2) TBTA (2mM in DMSO)	50 µM	2.5
3)Ascorbic acid (50mM, in H <sub>2</sub> O)	500 µM	1
4) Picolyl-azide-PEG <sub>4</sub> -Biotin (10mM)	250 µM	2.5
Total volume for 1 sample		7

Proteins were precipitated 2x by CHCl<sub>3</sub>/MeOH precipitation. For 100 µl click samples 400 µL MeOH, 100 µL CHCl<sub>3</sub> and 300 µL CHCl<sub>3</sub> (all solutions at 4°C) were added to each sample, vortexed and centrifuged (14 000 rcf, 5 minutes, 4 °C). The top layer was removed, 400 µL MeOH added, samples vortexed (14 000 rcf, 5 minutes, 4°C) and the supernatant removed. The protein pellet was redissolved in 100 µL 2% SDS in H<sub>2</sub>O by sonication in a BioRuptor (Diagenode) (3 cycles, low intensity, 5 s on, 45 s off) and shaking at 37 °C. Proteins were precipitated a second time as described above, protein pellet was air-dried for 10 minutes after removing supernatant; for 250 µL MS samples volumes were adjusted accordingly. Dry protein pellet was resuspended in 20 µL / 40 µL 2% SDS in H<sub>2</sub>O and dissolved via sonication (3x 3 cycles low intensity,5 s on, 45 s off) and shaking at 37°C, then diluted to 0.2 % SDS in H<sub>2</sub>O and sonicated again (3x 3 cycles low intensity,5 s on, 45 s off). 20 µL (10 µL for MS quality control) of input was removed and stored separately at -20°C.

### 3.7.4 Streptavidin Pull Down

25 µL Streptavidin Sepharose High Performance (GE Healthcare) beads per sample were equilibrated with 500 µL equilibration buffer (0.2 % SDS in H<sub>2</sub>O) for 10 minutes. Buffer was removed via centrifugation (1000 rcf, 2 minutes) and input samples mixed with the beads, then the slurry was incubated overnight under rotation at 4°C. Flow-

through was removed via centrifugation (1000 rcf, 2 minutes), 20  $\mu$ L samples (10  $\mu$ L for MS quality control) were stored separately at  $-20^{\circ}\text{C}$ . Beads were washed 2x for 5 minutes each with wash buffer 1 (1 mL 2% SDS in  $\text{H}_2\text{O}$ ) and wash buffer 2 (1 mL 50 mM HEPES pH7.4, 1 mM EDTA, 500 mM NaCl, 1% Triton X-100, 0.1% Na-deoxycholate in  $\text{H}_2\text{O}$ ), centrifugating in between (1000 rcf, 1 minute). Final buffer was removed and protein eluted with 20  $\mu$ L elution buffer ( $\text{H}_2\text{O}$ , 10% NP40, 10% SDS, 2mM biotin) for 5 minutes at  $98^{\circ}\text{C}$ . Beads were removed from eluate by centrifugation in 1.5 mL Mobicol Classic screw top tubes equipped with a 10  $\mu$ M filter (MoBiTec), 7  $\mu$ L 4x Laemmli buffer with 0.1 mM DTT added and samples boiled at  $98^{\circ}\text{C}$  for further 5 minutes. Denatured and reduced eluates were stored at  $-80^{\circ}\text{C}$  until further use or applied directly to SDS PAGE.

### **3.7.5 SDS PAGE and Western Blot analysis off pull-down probes**

Protein samples were applied to SDS PAGE (NuPage 4-12% Bis-Tris Gel) and ran for 5 minutes at 100 V, then for 45 minutes in MOPS buffer (Novex). Gels were blotted on to PVDF membrane at 30 V for 1 hour in transfer buffer (25 mM Tris, 20 mM glycine, 20% MeOH in  $\text{H}_2\text{O}$ ). The membrane was blocked for 1 hour in 5% milk in PBS, washed 3x with 0.1% Tween in PBS (PBS-T) and 1<sup>st</sup> antibody diluted 1:1000 – 1:2000 in 2% BSA in PBS added and incubated overnight at  $4^{\circ}\text{C}$  under shaking. 1<sup>st</sup> antibody dilution was removed, the membrane washed 3x with PBST and incubated with secondary antibody (anti-mouse or anti-rabbit Alexa-Fluor 800, ThermoFisher, 1:10000) and Streptavidin DyLight 680 (ThermoFisher, 1:15000) diluted in 2% BSA in PBS for 1 hour. The membrane was washed 3x with PBST, PBS was added and the membrane imaged using a LiCOR Odyssey infrared scanner. Images were analysed and processed in Image Studio Lite Quantification Software (Li-COR) and ImageJ software.

### **3.8 Data processing**

Microscopy data was analyzed and extracted parameters (Manders M1, M2, Pearson's R value, area, mean, raw intensity density) using the FluoQ macro<sup>265</sup> or Coloc2 plugging from ImageJ. TLC quantification of extracted lipids was performed by

determining the total intensity of each band in ImageJ. The raw integrated density of an equal rectangular ROI was measured for each lipid species and corrected for background via an identical, blank adjacent ROI. All line, bar, boxplot graphs and statistical analyses were generated using the ggplot2 package in R<sup>266</sup>. All figures were created in BioRender and all chemical structures were produced using ChemDraw Profesional v16.0 and images were curated using affinity designer studio v1.10.4

# References

---

1. Cohena, P. & Spiegel, B. M. Cell biology of fat storage. *Molecular Biology of the Cell* vol. 27 2523–2527 (2016).
2. An, S., Zheng, Y. & Bleu, T. Sphingosine 1-phosphate-induced cell proliferation, survival, and related signaling events mediated by G protein-coupled receptors Edg3 and Edg5. *Journal of Biological Chemistry* **275**, 288–296 (2000).
3. Malek, M. *et al.* Inositol triphosphate-triggered calcium release blocks lipid exchange at endoplasmic reticulum-Golgi contact sites. *Nature Communications* **12**, (2021).
4. van Meer, G. & de Kroon, A. I. P. M. Lipid map of the mammalian cell. *Journal of Cell Science* vol. 124 5–8 (2011).
5. Pichler, H. & Emmerstorfer-Augustin, A. Modification of membrane lipid compositions in single-celled organisms – From basics to applications. *Methods* **147**, 50–65 (2018).
6. Fernandez, C. *et al.* Plasma Lipid Composition and Risk of Developing Cardiovascular Disease. *PLoS ONE* **8**, (2013).
7. Kolter, T. & Sandhoff, K. Sphingolipid metabolism diseases. *Biochimica et Biophysica Acta - Biomembranes* **1758**, 2057–2079 (2006).
8. van Meer, G. Cellular lipidomics. *EMBO Journal* **24**, 3159–3165 (2005).
9. Vance, J. E. Phospholipid Synthesis and Transport in Mammalian Cells. *Traffic* vol. 16 1–18 (2015).
10. Kah Gedal, K., Zhao, M. & Brunk, U. T. *Sphingosine-induced apoptosis is dependent on lysosomal proteases.* *Biochem. J* vol. 359 (2001).
11. Chang, H.-C., Tsai, L.-H., Chuang, L.-Y. & Hung, W.-C. *Role of AKT Kinase in Sphingosine-Induced Apoptosis in Human Hepatoma Cells.* *Journal of cellular physiology* vol. 188 (2001).
12. Cuvillier, O., Edsall, L. & Spiegel, S. Involvement of sphingosine in mitochondria-dependent Fas-induced apoptosis of type II Jurkat T cells. *Journal of Biological Chemistry* **275**, 15691–15700 (2000).
13. Hö Glinger, D. *et al.* Intracellular sphingosine releases calcium from lysosomes. doi:10.7554/eLife.10616.001.
14. Pandol, S. J., Schoeffield-Payne, M. S., Gukovskaya, A. S. & Rutherford, R. E. *Sphingosine regulates Ca<sup>2+</sup>-ATPase and reloading of intracellular Ca<sup>2+</sup> stores in the pancreatic acinar cell.* *Biochimica et Biophysica Acta* vol. 1195 (1994).
15. Sweeney, E. A. *et al.* *Sphingosine and its methylated derivative in a variety of human cancer cell lines n,n-dimethylsphingosine (dms) induce apoptosis.* *Int. J. Cancer* vol. 66 (1996).
16. Ohta, H., Yatomi, Y., Sweeney, E. A. & Yasuyuki Igarashiayb, S. *A possible role of sphingosine in induction of apoptosis by tumor necrosis factor-α in human neutrophils.* *FEBS Letters* vol. 355 (1994).
17. Sakakura, C. *et al.* *Selectivity of Sphingosine-Induced Apoptosis Lack of Activity of DL-erythro-Dihydrosphingosine.* *Biochemical and biophysical research communications* vol. 246 (1998).

18. Levy, M. & Futerman, A. H. Mammalian ceramide synthases. *IUBMB Life* vol. 62 347–356 (2010).
19. Wattenberg, B. W. The long and the short of ceramides. *Journal of Biological Chemistry* **293**, 9922–9923 (2018).
20. Bourbon, N. A., Yun, J. & Kester, M. Ceramide directly activates protein kinase C  $\zeta$  to regulate a stress-activated protein kinase signaling complex. *Journal of Biological Chemistry* **275**, 35617–35623 (2000).
21. Huang, R. Cell adhesion mediated by glycolipids. *Nature* **276**, 624–626 (1978).
22. Furukawa, K. *et al.* Glycolipids: Essential regulator of neuro-inflammation, metabolism and gliomagenesis. *Biochimica et Biophysica Acta - General Subjects* vol. 1861 2479–2484 (2017).
23. Prinetti, A., Chigorno, V., Mauri, L., Loberto, N. & Sonnino, S. *Modulation of cell functions by glycosphingolipid metabolic remodeling in the plasma membrane. J. Neurochem* (2007).
24. Hannun, Y. A. & Obeid, L. M. Sphingolipids and their metabolism in physiology and disease. *Nature Reviews Molecular Cell Biology* vol. 19 175–191 (2018).
25. Dufourc, E. J. Sterols and membrane dynamics. *Journal of Chemical Biology* **1**, 63–77 (2008).
26. Lingwood, D. & Simons, K. *Lipid Rafts As a Membrane-Organizing Principle*. <https://www.science.org>.
27. Simons, K. & Ehehalt, R. Cholesterol, lipid rafts, and disease. *Journal of Clinical Investigation* **110**, 597–603 (2002).
28. Sleat, D. E., Valle, M. C. D., Zheng, H., Moore, D. F. & Lobel, P. The mannose 6-phosphate glycoprotein proteome. *Journal of Proteome Research* **7**, 3010–3021 (2008).
29. Zoncu, R. *et al.* mTORC1 senses lysosomal amino acids through an inside-out mechanism that requires the vacuolar H<sup>+</sup>-ATPase. *Science* **334**, 678–683 (2011).
30. Lee, M. N. *et al.* Glycolytic Flux Signals to mTOR through Glyceraldehyde-3-Phosphate Dehydrogenase-Mediated Regulation of Rheb. *Molecular and Cellular Biology* **29**, 3991–4001 (2009).
31. Rocznik-Ferguson, A. *et al.* The transcription factor TFEB links mTORC1 signaling to transcriptional control of lysosome homeostasis. *Science Signaling* **5**, (2012).
32. Platt, F. M., d’Azzo, A., Davidson, B. L., Neufeld, E. F. & Tiffit, C. J. Lysosomal storage diseases. *Nature Reviews Disease Primers* vol. 4 (2018).
33. Heinrich, M. *et al.* *Cathepsin D targeted by acid sphingomyelinase-derived ceramide. The EMBO Journal* vol. 18 (1999).
34. Wang, S. E., Norred, W. P., Bacon, C. W., Riley, R. T. & Merrill, A. H. *Inhibition of Sphingolipid Biosynthesis by Fumonisin Implications for diseases associated with fusarium moniliforme\**. *The journal of biological chemistry* vol. 266 (1991).
35. Rother, J., van Echten, G., Schwarzmann, G. & Sandhoff, K. *Biochemical and biophysical research communications November 30*. vol. 189 (1992).
36. Kitatani, K., Idkowiak-Baldys, J. & Hannun, Y. A. The sphingolipid salvage pathway in ceramide metabolism and signaling. *Cellular Signalling* vol. 20 1010–1018 (2008).
37. Gillard, B. K., Clement, R. G. & Marcus, D. M. *Variations among cell lines in the synthesis of sphingolipids in de novo and recycling pathways. Glycobiology* vol. 8 <https://academic.oup.com/glycob/article/8/9/885/605382> (1998).
38. Brown, M. S. & Goldstein, J. L. *A receptor-mediated pathway for cholesterol homeostasis*.

39. Chang, T. Y., Chang, C. C. Y., Ohgami, N. & Yamauchi, Y. Cholesterol sensing, trafficking, and esterification. *Annual Review of Cell and Developmental Biology* vol. 22 129–157 (2006).
40. Goldstein, J. L., Dana, S. E., Faust, J. R., Beaudet, A. L. & Brown, M. S. Role of lysosomal acid lipase in the metabolism of plasma low density lipoprotein. Observations in cultured fibroblasts from a patient with cholesteryl ester storage disease. *Journal of Biological Chemistry* **250**, 8487–8495 (1975).
41. Bell, R. M., Ballas, L. M. & Coleman, R. A. *Lipid topogenesis*.
42. Hannun, Y. A. & Obeid, L. M. Principles of bioactive lipid signalling: Lessons from sphingolipids. *Nature Reviews Molecular Cell Biology* **9**, 139–150 (2008).
43. Phillips, M. J. & Voeltz, G. K. Structure and function of ER membrane contact sites with other organelles. *Nature Reviews Molecular Cell Biology* vol. 17 69–82 (2016).
44. Hanada, K. *et al.* *Molecular machinery for non-vesicular trafficking of ceramide*. [www.nature.com/nature](http://www.nature.com/nature) (2003).
45. Peretti, D., Dahan, N., Shimoni, E., Hirschberg, K. & Lev, S. Coordinated Lipid Transfer between the Endoplasmic Reticulum and the Golgi Complex Requires the VAP Proteins and Is Essential for Golgi-mediated Transport. *Molecular Biology of the Cell* **19**, 3871–3884 (2008).
46. Hanada, K. Discovery of the molecular machinery CERT for endoplasmic reticulum-to-Golgi trafficking of ceramide. *Molecular and Cellular Biochemistry* vol. 286 23–31 (2006).
47. Funato, K. & Riezman, H. Vesicular and nonvesicular transport of ceramide from ER to the Golgi apparatus in yeast. *Journal of Cell Biology* **155**, 949–959 (2001).
48. Contreras, F. X. *et al.* Molecular recognition of a single sphingolipid species by a protein's transmembrane domain. *Nature* **481**, 525–529 (2012).
49. Björkholm, P. *et al.* Identification of novel sphingolipid-binding motifs in mammalian membrane proteins. *Biochimica et Biophysica Acta - Biomembranes* **1838**, 2066–2070 (2014).
50. D'Angelo, G. *et al.* Glycosphingolipid synthesis requires FAPP2 transfer of glucosylceramide. *Nature* **449**, 62–67 (2007).
51. Ochoa-Lizarralde, B. *et al.* Structural analyses of 4-phosphate adaptor protein 2 yield mechanistic insights into sphingolipid recognition by the glycolipid transfer protein family. *Journal of Biological Chemistry* **293**, 16709–16723 (2019).
52. Simanshu, D. K. *et al.* Non-vesicular trafficking by a ceramide-1-phosphate transfer protein regulates eicosanoids. *Nature* **500**, 463–467 (2013).
53. Mesmin, B., Kovacs, D. & D'Angelo, G. Lipid exchange and signaling at ER–Golgi contact sites. *Current Opinion in Cell Biology* vol. 57 8–15 (2019).
54. Mesmin, B. *et al.* XA four-step cycle driven by PI(4)P hydrolysis directs sterol/PI(4)P exchange by the ER–Golgi Tether OSBP. *Cell* **155**, 830 (2013).
55. Storch, J. & Cheruku, S. R. Cholesterol Transport in Lysosomes. *Lysosomes* 100–111 (2007) doi:10.1007/0-387-28957-7\_9.
56. Meng, Y., Heybrock, S., Neculai, D. & Saftig, P. Cholesterol Handling in Lysosomes and Beyond. *Trends in Cell Biology* vol. 30 452–466 (2020).
57. Schoop, V., Martello, A., Eden, E. R. & Höglinger, D. Cellular cholesterol and how to find it. *Biochimica et Biophysica Acta - Molecular and Cell Biology of Lipids* vol. 1866 (2021).
58. Infante, R. E. *et al.* NPC2 facilitates bidirectional transfer of cholesterol between NPC1 and lipid bilayers, a step in cholesterol egress from lysosomes. *Proceedings of the National Academy of Sciences of the United States of America* **105**, 15287–15292 (2008).

59. Kwon, H. J. *et al.* Structure of N-Terminal Domain of NPC1 Reveals Distinct Subdomains for Binding and Transfer of Cholesterol. *Cell* **137**, 1213–1224 (2009).
60. Qian, H. *et al.* Structural Basis of Low-pH-Dependent Lysosomal Cholesterol Egress by NPC1 and NPC2. *Cell* **182**, 98–111.e18 (2020).
61. Xu, S., Benoff, B., Liou, H. L., Lobel, P. & Stock, A. M. Structural basis of sterol binding by NPC2, a lysosomal protein deficient in Niemann-Pick type C2 disease. *Journal of Biological Chemistry* **282**, 23525–23531 (2007).
62. McCauliff, L. A. *et al.* Intracellular cholesterol trafficking is dependent upon NPC2 interaction with lysobisphosphatidic acid. *eLife* **8**, 1–31 (2019).
63. Vanier, M. T. & Millat, G. Structure and function of the NPC2 protein. *Biochimica et Biophysica Acta - Molecular and Cell Biology of Lipids* vol. 1685 14–21 (2004).
64. Ko, D. C., Binkley, J., Sidow, A. & Scott, M. P. *The integrity of a cholesterol-binding pocket in Niemann-Pick C2 protein is necessary to control lysosome cholesterol levels.* vol. 100 www.pnas.org/cgi/doi/10.1073/pnas.0530027100 (1999).
65. Côté, M. *et al.* Small molecule inhibitors reveal Niemann-Pick C1 is essential for Ebola virus infection. *Nature* **477**, 344–348 (2011).
66. Carette, J. E. *et al.* Ebola virus entry requires the cholesterol transporter Niemann-Pick C1. *Nature* **477**, 340–343 (2011).
67. Futerman, A. H. & van Meer, G. The cell biology of lysosomal storage disorders. *Nature Reviews Molecular Cell Biology* vol. 5 554–565 (2004).
68. Martina, J. A., Raben, N. & Puertollano, R. SnapShot: Lysosomal Storage Diseases. *Cell* **180**, 602–602.e1 (2020).
69. Meikle, P., Hopwood, J., Clague, A. & Carey, W. Prevalence of lysosomal storage disorders. *Jama* **281**, 249–254 (1999).
70. Liscum, L. *Niemann-Pick Type C Mutations Cause Lipid Traffic Jam.* *Traffic* vol. 1 (2000).
71. Newton, J., Milstien, S. & Spiegel, S. Niemann-Pick type C disease: The atypical sphingolipidosis. *Advances in Biological Regulation* vol. 70 82–88 (2018).
72. Vanier, M. T. & Latour, P. Laboratory diagnosis of Niemann-Pick disease type C: The filipin staining test. *Methods in Cell Biology* **126**, 357–375 (2015).
73. Rodriguez-Lafrasse, C., Rousson, R., Pentchev, P. G., Louisot, P. & Vanier, M. T. *Free sphingoid bases in tissues from patients with type C Niemann-Pick disease and other lysosomal storage disorders.* *Biochimica et Biophysica Acta* vol. 1226 (1994).
74. Choudhury, A., Sharma, D. K., Marks, D. L. & Pagano, R. E. Elevated Endosomal Cholesterol Levels in Niemann-Pick Cells Inhibit Rab4 and Perturb Membrane Recycling □ *D. Molecular Biology of the Cell* **15**, 4500–4511 (2004).
75. Winkler, M. B. L. *et al.* Structural Insight into Eukaryotic Sterol Transport through Niemann-Pick Type C Proteins. *Cell* **179**, 485–497.e18 (2019).
76. Li, X. *et al.* Structure of human Niemann-Pick C1 protein. *Proceedings of the National Academy of Sciences of the United States of America* **113**, 8212–8217 (2016).
77. Lu, F. *et al.* Identification of NPC1 as the target of U18666A, an inhibitor of lysosomal cholesterol export and Ebola infection. (2015) doi:10.7554/eLife.12177.001.
78. Trinha, M. N. *et al.* Triazoles inhibit cholesterol export from lysosomes by binding to NPC1. *Proceedings of the National Academy of Sciences of the United States of America* **114**, 89–94 (2017).
79. Long, T. *et al.* Structural basis for itraconazole-mediated NPC1 inhibition. *Nature Communications* **11**, (2020).
80. Lu, F. *et al.* Identification of NPC1 as the target of U18666A, an inhibitor of lysosomal cholesterol export and Ebola infection. *eLife* **4**, 1–16 (2015).

81. Cheruku, S. R., Xu, Z., Dutia, R., Lobel, P. & Storch, J. Mechanism of cholesterol transfer from the Niemann-Pick type C2 protein to model membranes supports a role in lysosomal cholesterol transport. *Journal of Biological Chemistry* **281**, 31594–31604 (2006).
82. Babalola, J. O. *et al.* Development of an assay for the intermembrane transfer of cholesterol by Niemann-Pick C2 protein. *Biological Chemistry* **388**, 617–626 (2007).
83. Tharkeshwar, A. K. *et al.* A novel approach to analyze lysosomal dysfunctions through subcellular proteomics and lipidomics: The case of NPC1 deficiency. *Scientific Reports* **7**, (2017).
84. Du, X. *et al.* A role for oxysterol-binding protein-related protein 5 in endosomal cholesterol trafficking. *Journal of Cell Biology* **192**, 121–135 (2011).
85. Höglinger, D. *et al.* NPC1 regulates ER contacts with endocytic organelles to mediate cholesterol egress. *Nature Communications* **10**, (2019).
86. Brown, M. S. & Goldstein, J. L. *The SREBP Pathway: Regulation Review of Cholesterol Metabolism by Proteolysis of a Membrane-Bound Transcription Factor.* *Cell* vol. 89 (1997).
87. Thiele, C. & Spandl, J. Cell biology of lipid droplets. *Current Opinion in Cell Biology* vol. 20 378–385 (2008).
88. Wijdeven, R. H. *et al.* Cholesterol and ORP1L-mediated ER contact sites control autophagosome transport and fusion with the endocytic pathway. *Nature Communications* **7**, (2016).
89. Zhao, K. & Ridgway, N. D. Oxysterol-Binding Protein-Related Protein 1L Regulates Cholesterol Egress from the Endo-Lysosomal System. *Cell Reports* **19**, 1807–1818 (2017).
90. Wilhelm, L. P. *et al.* STARD 3 mediates endoplasmic reticulum-to-endosome cholesterol transport at membrane contact sites. *The EMBO Journal* **36**, 1412–1433 (2017).
91. Li, J. & Pfeffer, S. R. Lysosomal membrane glycoproteins bind cholesterol and contribute to lysosomal cholesterol export. *eLife* (2016) doi:10.7554/eLife.21635.001.
92. Heybrock, S. *et al.* Lysosomal integral membrane protein-2 (LIMP-2/SCARB2) is involved in lysosomal cholesterol export. *Nature Communications* **10**, (2019).
93. Kuronita, T. *et al.* A role for the lysosomal membrane protein LGP85 in the biogenesis and maintenance of endosomal and lysosomal morphology. *Journal of Cell Science* vol. 115 4117–4131 (2002).
94. Kuronita, T. *et al.* The NH<sub>2</sub>-terminal transmembrane and lumenal domains of LGP85 are needed for the formation of enlarged endosomes/lysosomes. *Traffic* **6**, 895–906 (2005).
95. Rothaug, M. *et al.* LIMP-2 expression is critical for  $\beta$ -glucocerebrosidase activity and  $\alpha$ -synuclein clearance. *Proceedings of the National Academy of Sciences of the United States of America* **111**, 15573–15578 (2014).
96. Zhao, Y., Ren, J., Padilla-Parra, S., Fry, E. E. & Stuart, D. I. Lysosome sorting of  $\beta$ -glucocerebrosidase by LIMP-2 is targeted by the mannose 6-phosphate receptor. *Nature Communications* **5**, (2014).
97. Fuller, M. Sphingolipids: The nexus between Gaucher disease and insulin resistance. *Lipids in Health and Disease* **9**, 1–12 (2010).
98. Velayati, A. *et al.* A mutation in SCARB2 is a modifier in gaucher disease. *Human Mutation* **32**, 1232–1238 (2011).
99. Yamayoshi, S. *et al.* Scavenger receptor B2 is a cellular receptor for enterovirus 71. *Nature Medicine* **15**, 798–801 (2009).

100. Neculai, D. *et al.* Structure of LIMP-2 provides functional insights with implications for SR-BI and CD36. *Nature* **504**, 172–176 (2013).
101. Acton, S. *et al.* Identification of scavenger receptor SR-BI as a high density lipoprotein receptor. *Science* **271**, 518–520 (1996).
102. F Nieland, T. J., Penman, M., Dori, L., Krieger, M. & Kirchhausen, T. Discovery of chemical inhibitors of the selective transfer of lipids mediated by the HDL receptor SR-BI. *Proceedings of the National Academy of Sciences* **99**, 15422–15427 (2002).
103. Linton, M. F., Tao, H., Linton, E. F. & Yancey, P. G. SR-BI: A Multifunctional Receptor in Cholesterol Homeostasis and Atherosclerosis. *Trends in Endocrinology and Metabolism* vol. 28 461–472 (2017).
104. Ji, Y. *et al.* Scavenger receptor BI promotes high density lipoprotein-mediated cellular cholesterol efflux. *Journal of Biological Chemistry* **272**, 20982–20985 (1997).
105. Harayama, T. & Riezman, H. Understanding the diversity of membrane lipid composition. *Nature Reviews Molecular Cell Biology* vol. 19 281–296 (2018).
106. Maier, O., Oberle, V. & Hoekstra, D. *Fluorescent lipid probes: some properties and applications (a review)*. *Chemistry and Physics of Lipids* vol. 116 www.elsevier.com/locate/chemphyslip (2002).
107. Bielawska, A., Hannun, Y. A. & Szulc, Z. 480 *CHEMICAL AND ENZYMATIc SYNTHESSES [42] [42] Radiolabeling of the Sphingolipid Backbone*. (1999).
108. Bielawska, A., Szulc, Z. & Hannun, Y. A. 518 *CHEMICAL AND ENZYMATIc SYNTHESSES Introduction\**. (1999).
109. Chigorno, V., Sciannamblo, M., Mikulak, J., Prinetti, A. & Sonnino, S. Efflux of sphingolipids metabolically labeled with [1-3H] sphingosine, L-[3-3H]serine and [9,10-3H]palmitic acid from normal cells in culture. *Glycoconjugate Journal* **23**, 159–165 (2006).
110. Michel, C. *et al.* Characterization of Ceramide Synthesis a dihydroceramide desaturase introduces the 4,5-trans-double bond of sphingosine at the level of dihydroceramide\*. *The journal of biological chemistry* vol. 272 <http://www.jbc.org> (1997).
111. Rother, J., van Echten, G., Schwarzmann, G. & Sandhoff, K. *Biochemical and biophysical research communications November 30*. vol. 189 (1992).
112. Merrill, A. H. De novo sphingolipid biosynthesis: A necessary, but dangerous, pathway. *Journal of Biological Chemistry* vol. 277 25843–25846 (2002).
113. Zhang, M. *et al.* MLN64 mediates mobilization of lysosomal cholesterol to steroidogenic mitochondria. *Journal of Biological Chemistry* **277**, 33300–33310 (2002).
114. Kaplan, M. R. & Simoni, R. D. *Transport of Cholesterol from the Endoplasmic Reticulum to the Plasma Membrane*. <http://rupress.org/jcb/article-pdf/101/2/446/1051840/446.pdf>.
115. Infante, R. E. *et al.* Purified NPC1 protein II. Localization of sterol binding to a 240-amino acid soluble luminal loop. *Journal of Biological Chemistry* **283**, 1064–1075 (2008).
116. Infante, R. E. *et al.* NPC2 facilitates bidirectional transfer of cholesterol between NPC1 and lipid bilayers, a step in cholesterol egress from lysosomes. [www.pnas.org/cgi/content/full/](http://www.pnas.org/cgi/content/full/) (2008).
117. Fu, Y. & Finney, N. S. Small-molecule fluorescent probes and their design. *RSC Advances* vol. 8 29051–29061 (2018).
118. Lpsky, N. G. & Pagano, R. E. *Sphingolipid metabolism in cultured fibroblasts: Microscopic and biochemical studies employing a fluorescent ceramide analogue*

- (Golgi apparatus/sphingomyelin/cerebrosides/liposomes/fluorescence). *Proc. Natl Acad. Sci. USA* vol. 80 (1983).
119. Geller Lipsky, N. & E Pagano, R. A vital stain for the Golgi Apparatus. *Science* **228**, 745–747 (1983).
  120. Struck, D. K. & Pagano, R. E. Insertion of Fluorescent Phospholipids into the Plasma Membrane of a Mammalian Cell\*. *The journal of biological chemistry* **255**, 5404–5410 (1980).
  121. Spiegel, S., Kassis, S., Wilchek, M. & Fishman, P. H. Direct Visualization of Redistribution and Capping of Fluorescent Gangliosides on Lymphocytes. *The Journal of Cell Biology* **99**, 1575–1581 (1984).
  122. Hölttä-Vuori, M. *et al.* BODIPY-cholesterol: A new tool to visualize sterol trafficking in living cells and organisms. *Traffic* **9**, 1839–1849 (2008).
  123. van Ijzendoorn, S. C. D., Hoekstra, D., Zegers, M. M. P., Kok, J. W. & Hoek, D. (Glyco)sphingolipids are sorted in Sub-Apical Compartments in HepG2 Cells: A Role for Non-Golgi-Related Intracellular Sites in the Polarized Distribution of (Glyco)sphingolipids. *The Journal of Cell Biology* **142**, 347–457 (1998).
  124. Ledesma, M. D., Brügger, B., Bunning, C., Wieland, F. T. & Dotti, C. G. Maturation of the axonal plasma membrane requires upregulation of sphingomyelin synthesis and formation of protein-lipid complexes. *The EMBO Journal* **18**, 1761–1771 (1999).
  125. Tepper, A. D. *et al.* Sphingomyelin Hydrolysis to Ceramide during the Execution Phase of Apoptosis Results from Phospholipid Scrambling and Alters Cell-surface Morphology. *The Journal of Cell Biology* vol. 150 <http://www.jcb.org> (2000).
  126. Wüstner, D. Fluorescent sterols as tools in membrane biophysics and cell biology. *Chemistry and Physics of Lipids* vol. 146 1–25 (2007).
  127. Chattopadhyay, A. *Chemistry and biology of N-(7-nitrobenz-2-oxa-1,3-diazol-4-yl)-labeled lipids" fluorescent probes of biological and model membranes.* *Chemistry and Physics of Lipids* (1990).
  128. Ashcroft, R., Thulborn, K., J, S., H, C. & Sawyer, W. Perturbations to lipid bilayers by spectroscopic probes as determined by dielectric measurements. *Biochimica et Biophysica Acta* **602**, 299–308 (1980).
  129. Ohki, S., Flanagan, T. D. & Hoekstra, D. Probe Transfer with and without Membrane Fusion in a Fluorescence Fusion Assay †. *Biochemistry* **37**, 7496–7503 (1998).
  130. Fox, J. Bioorthogonal chemistry. *Nature Reviews* (2021).
  131. Kolb, H., Finn, M. G. & Sharpless, B. Click Chemistry : Diverse Chemical Function from a Few Good Reactions. *Angewandte Chemie* **40**, 2004–2021 (2001).
  132. Thiele, C. *et al.* Tracing fatty acid metabolism by click chemistry. *ACS Chemical Biology* **7**, 2004–2011 (2012).
  133. Jao, C. Y., Roth, M., Welti, R. & Salic, A. Metabolic labeling and direct imaging of choline phospholipids in vivo. *PNAS* **106**, 15332–15337 (2009).
  134. Smith, M. D., Sudhakar, C. G., Gong, D., Stahelin, R. v. & Best, M. D. Modular synthesis of biologically active phosphatidic acid probes using click chemistry. *Molecular BioSystems* **5**, 962–972 (2009).
  135. Neef, A. B. & Schultz, C. Selective fluorescence labeling of lipids in living cells. *Angewandte Chemie - International Edition* **48**, 1498–1500 (2009).
  136. Jiang, H. *et al.* Monitoring dynamic glycosylation in vivo using supersensitive click chemistry. *Bioconjugate Chemistry* **25**, 698–706 (2014).
  137. Baskin, J. M. *et al.* Copper-free click chemistry for dynamic in vivo imaging. [www.pnas.org/cgi/content/full/](http://www.pnas.org/cgi/content/full/) (2007).
  138. Sawa, M. *et al.* Glycoproteomic probes for fluorescent imaging of fucosylated glycans in vivo. [www.pnas.org/cgi/doi/10.1073/pnas.0605418103](http://www.pnas.org/cgi/doi/10.1073/pnas.0605418103) (2006).

139. Fantoni, N. Z., El-Sagheer, A. H. & Brown, T. A Hitchhiker's Guide to Click-Chemistry with Nucleic Acids. *Chemical Reviews* vol. 121 7122–7154 (2021).
140. Singh, A., Thornton, E. & Westheimer, F. H. The photolysis of Diazoacetylchymotrypsin. *Journal of Biological Chemistry* **237**, (1962).
141. Wittelsberger, A., Mierke, D. F. & Rosenblatt, M. Mapping ligand-receptor interfaces: Approaching the resolution limit of benzophenone-based photoaffinity scanning. *Chemical Biology and Drug Design* **71**, 380–383 (2008).
142. Rihakova, L. *et al.* Methionine proximity assay, a novel method for exploring peptide ligand-receptor interaction. in *Journal of Receptors and Signal Transduction* vol. 22 297–313 (2002).
143. Grunbeck, A., Huber, T. & Sakmar, T. P. Mapping a ligand binding site using genetically encoded photoactivatable crosslinkers. in *Methods in Enzymology* vol. 520 307–322 (Academic Press Inc., 2013).
144. Pardin, C. *et al.* Photolabeling of tissue transglutaminase reveals the binding mode of potent cinnamoyl inhibitors. *Biochemistry* **48**, 3346–3353 (2009).
145. Lekostaj, J. K., Natarajan, J. K., Paguio, M. F., Wolf, C. & Roepe, P. D. Photoaffinity labeling of the Plasmodium falciparum chloroquine resistance transporter with a novel perfluorophenylazido chloroquine. *Biochemistry* **47**, 10394–10406 (2008).
146. Xia, Y. & Peng, L. Photoactivatable lipid probes for studying biomembranes by photoaffinity labeling. *Chemical Reviews* vol. 113 7880–7929 (2013).
147. Hulce, J. J., Cognetta, A. B., Niphakis, M. J., Tully, S. E. & Cravatt, B. F. Proteome-wide mapping of cholesterol-interacting proteins in mammalian cells. *Nature Methods* **10**, 259–264 (2013).
148. Haberkant, P. *et al.* Bifunctional Sphingosine for Cell-Based Analysis of Protein-Sphingolipid Interactions. *ACS Chemical Biology* **11**, 222–230 (2016).
149. Haberkant, P. *et al.* In vivo profiling and visualization of cellular protein-lipid interactions using bifunctional fatty acids. *Angewandte Chemie - International Edition* **52**, 4033–4038 (2013).
150. Bockelmann, S. *et al.* A search for ceramide binding proteins using bifunctional lipid analogs yields CERT-related protein StarD7. *Journal of Lipid Research* **59**, 515–530 (2018).
151. Höglinger, D., Nadler, A. & Schultz, C. Caged lipids as tools for investigating cellular signaling. *Biochimica et Biophysica Acta - Molecular and Cell Biology of Lipids* **1841**, 1085–1096 (2014).
152. Wagner, N., Stephan, M., Höglinger, D. & Nadler, A. A Click Cage: Organelle-Specific Uncaging of Lipid Messengers. *Angewandte Chemie - International Edition* **57**, 13339–13343 (2018).
153. Höglinger, D. *et al.* Trifunctional lipid probes for comprehensive studies of single lipid species in living cells. *Proceedings of the National Academy of Sciences of the United States of America* **114**, 1566–1571 (2017).
154. Nadler, A. *et al.* Exclusive photorelease of signalling lipids at the plasma membrane. *Nature Communications* **6**, 1–10 (2015).
155. Schuhmacher, M. *et al.* Addressing lipid structural diversity in signalling: Photochemical probes for live-cell lipid biochemistry. *bioRxiv* 711291 (2019) doi:10.1101/711291.
156. Chauhan, N., Sere, Y. Y., Sokol, A. M., Graumann, J. & Menon, A. K. A PhotoClick cholesterol-based quantitative proteomics screen for cytoplasmic sterol-binding proteins in *Saccharomyces cerevisiae*. *Yeast* **37**, 15–25 (2020).
157. Gerl, M. J. *et al.* Sphingosine-1-phosphate lyase deficient cells as a tool to study protein lipid interactions. *PLoS ONE* **11**, (2016).

158. Goeldner, Maurice. & Givens, Richard. *Dynamic studies in biology : phototriggers, photoswitches and caged biomolecules*. (Wiley-VCH, 2005).
159. Bardhan, A. & Deiters, A. Development of photolabile protecting groups and their application to the optochemical control of cell signaling. *Current Opinion in Structural Biology* vol. 57 164–175 (2019).
160. Mccray, J. A., Herbettet, L., Kihara, T. & Trentham, D. R. *A new approach to time-resolved studies of ATP-requiring biological systems: Laser flash photolysis of caged ATP (spectrophotometry/actomyosin ATPase/transient kinetics) The photolysis of I results in the formation of 2-nitrosoacetophenone (5) and a proton, depending on the ionization state of ATP (Eq. 1)*. *Biophysics* vol. 77 (1980).
161. Cui, J., Gropeanu, R. A., Stevens, D. R., Rettig, J. & Campo, A. del. New photolabile BAPTA-based Ca<sup>2+</sup> cages with improved photorelease. *Journal of the American Chemical Society* **134**, 7733–7740 (2012).
162. Ellis-Davies, G. C. R. Two-Photon Uncaging of Glutamate. *Frontiers in Synaptic Neuroscience* **10**, (2019).
163. Sansalone, L. *et al.* Photopotential of the GABA<sub>A</sub> receptor with caged diazepam. *Proceedings of the National Academy of Sciences of the United States of America* **116**, 21176–21184 (2019).
164. Bourbon, P. *et al.* Synthesis and photochemical behavior of coumarin-caged cholesterol. *Bioorganic and Medicinal Chemistry Letters* **23**, 2162–2165 (2013).
165. Höglinger, D. *et al.* Intracellular sphingosine releases calcium from lysosomes. *eLife* **4**, 1–20 (2015).
166. Müller, R., Kojic, A., Citir, M. & Schultz, C. Synthesis and Cellular Labeling of Multifunctional Phosphatidylinositol Bis- and Trisphosphate Derivatives. *Angewandte Chemie - International Edition* **60**, 19759–19765 (2021).
167. Zhao, Y. R. *et al.* New Caged Coumarin Fluorophores with Extraordinary Uncaging Cross Sections Suitable for Biological Imaging Applications. *Journal of the American Chemical Society* **126**, 4653–4663 (2004).
168. Al-Haiza, M. A., Mostafa, M. S. & El-Kady, M. Y. Synthesis and biological evaluation of some new coumarin derivatives. *Molecules* **8**, 275–286 (2003).
169. Kapp, E. *et al.* Versatility of 7-substituted coumarin molecules as antimycobacterial agents, neuronal enzyme inhibitors and neuroprotective agents. *Molecules* **22**, (2017).
170. Givens, R. S., Rubina, M. & Wirz, J. Applications of p-hydroxyphenacyl (pHP) and coumarin-4-ylmethyl photoremovable protecting groups. *Photochemical and Photobiological Sciences* vol. 11 472–488 (2012).
171. Voilquin, L. *et al.* STARD3: A Swiss Army Knife for Intracellular Cholesterol Transport. *Contact* **2**, 251525641985673 (2019).
172. Höglinger, D., Nadler, A. & Schultz, C. Caged lipids as tools for investigating cellular signaling. *Biochimica et Biophysica Acta - Molecular and Cell Biology of Lipids* **1841**, 1085–1096 (2014).
173. Winterbourn, C. C. Reconciling the chemistry and biology of reactive oxygen species. *Nature Chemical Biology* vol. 4 278–286 (2008).
174. Paulsen, C. E. & Carroll, K. S. Cysteine-mediated redox signaling: Chemistry, biology, and tools for discovery. *Chemical Reviews* vol. 113 4633–4679 (2013).
175. Xu, W., Zeng, Z., Jiang, J. H., Chang, Y. T. & Yuan, L. Discerning the Chemistry in Individual Organelles with Small-Molecule Fluorescent Probes. *Angewandte Chemie - International Edition* **55**, 13658–13699 (2016).
176. Murphy, M. P. *Slip and leak in mitochondrial oxidative phosphorylation*. *Biochimica et Biophysica Acta* vol. 977 (1989).

177. Ross, M. F., Kelso, F. G., Blaikie, H. F. & Murphy, M. P. Lipophilic Triphenylphosphonium Cations as Tools in Mitochondrial Bioenergetics and Free Radical Biology. *Biochemistry* **70**, 222–230 (2005).
178. Porteous, C. M. *et al.* Rapid uptake of lipophilic triphenylphosphonium cations by mitochondria in vivo following intravenous injection: Implications for mitochondria-specific therapies and probes. *Biochimica et Biophysica Acta - General Subjects* **1800**, 1009–1017 (2010).
179. Colom, A. *et al.* A fluorescent membrane tension probe. *Nature Chemistry* **10**, 1118–1125 (2018).
180. Danylchuk, D. I., Jouard, P. H. & Klymchenko, A. S. Targeted Solvatochromic Fluorescent Probes for Imaging Lipid Order in Organelles under Oxidative and Mechanical Stress. *Journal of the American Chemical Society* **143**, 912–924 (2021).
181. Tian, X. *et al.* Endoplasmic Reticulum Targeting Ratiometric Fluorescent Probe for Carboxylesterase 2 Detection in Drug-Induced Acute Liver Injury. *Analytical Chemistry* **91**, 15840–15845 (2019).
182. Song, W. *et al.* Development of an endoplasmic reticulum-targeting fluorescent probe for the imaging of polarity in living cells and tissues. *New Journal of Chemistry* **43**, 12103–12108 (2019).
183. Casey, J. R., Grinstein, S. & Orlowski, J. Sensors and regulators of intracellular pH. *Nature Reviews Molecular Cell Biology* vol. 11 50–61 (2010).
184. Kaufmann, A. M. & Krise, J. P. Lysosomal sequestration of amine-containing drugs: Analysis and therapeutic implications. *Journal of Pharmaceutical Sciences* vol. 96 729–746 (2007).
185. Yu, H., Xiao, Y. & Jin, L. A lysosome-targetable and two-photon fluorescent probe for monitoring endogenous and exogenous nitric oxide in living cells. *Journal of the American Chemical Society* **134**, 17486–17489 (2012).
186. *Probes for Organelles Molecular Probes™ Handbook A Guide to Fluorescent Probes and Labeling Technologies 11th Edition (2010) Fluorophores and Their Amine-Reactive Derivatives The Molecular Probes® Handbook A GUIDE TO FLUORESCENT PROBES AND LABELING TECHNOLOGIES 11th Edition (2010).* [www.invitrogen.com/probes](http://www.invitrogen.com/probes).
187. Feng, S. *et al.* Lysosome-targeted photoactivation reveals local sphingosine metabolism signatures. *Chemical Science* **10**, 2253–2258 (2019).
188. Feng, S. *et al.* Mitochondria-specific photoactivation to monitor local sphingosine metabolism and function. *eLife* **7**, 1–23 (2018).
189. Klán, P. *et al.* Photoremovable protecting groups in chemistry and biology: Reaction mechanisms and efficacy. *Chemical Reviews* vol. 113 119–191 (2013).
190. Goeldner, Maurice. & Givens, Richard. *Dynamic studies in biology : phototriggers, photoswitches and caged biomolecules.* (Wiley-VCH, 2005).
191. Bogyo, M., Verhelst, S., Bellingard-Dubouchaud, V., Toba, S. & Greenbaum, D. Selective targeting of lysosomal cysteine proteases with radiolabeled electrophilic substrate analogs. *Chemistry & Biology* **7**, 27–38 (2000).
192. Hang, H. C. *et al.* Mechanism-based probe for the analysis of cathepsin cysteine proteases in living cells. *ACS chemical biology* **1**, 713–723 (2006).
193. Meara, J. P. & Rich, D. H. Mechanistic Studies on the Inactivation of Papain by Epoxysuccinyl Inhibitors. *J. Med. Chem.* **39**, 3357–3366 (1996).
194. Albeck, A. & Kliper, S. *Mechanism of cysteine protease inactivation by peptidyl epoxides.* *Biochem. J* vol. 322 (1997).

195. Gour-Salin, J., B. J., Lachance, P., Plouffe, C., Storer, A. C. & Mbnard, R. *Epoxy succinyl Dipeptides as Selective Inhibitors of Cathepsin Bt. J. Med. Chem* vol. 36 (1993).
196. Siklos, M., BenAissa, M. & Thatcher, G. R. J. Cysteine proteases as therapeutic targets: Does selectivity matter? A systematic review of calpain and cathepsin inhibitors. *Acta Pharmaceutica Sinica B* vol. 5 506–519 (2015).
197. Chehade, K. A. H., Baruch, A., Verhelst, S. H. L. & Bogyo, M. An improved preparation of the activity-based probe JPM-OEt and in situ applications. *Synthesis* 240–244 (2005) doi:10.1055/s-2004-837295.
198. Han, Y., Li, M., Qiu, F., Zhang, M. & Zhang, Y. H. Cell-permeable organic fluorescent probes for live-cell long-term super-resolution imaging reveal lysosome-mitochondrion interactions. *Nature Communications* **8**, (2017).
199. Iwasawa, H. & Mori, K. Stereoselective synthesis of optically active forms of Multistriatin, the attractant for european populations of the smaller european elm back beetle. *Tetrahedron* **36**, 87–90 (1980).
200. Lundquist IV, J. T. & Pelletier, J. C. Improved solid-phase peptide synthesis method utilizing  $\alpha$ -azide-protected amino acids. *Organic Letters* **3**, 781–783 (2001).
201. Montalbetti, C. A. G. N. & Falque, V. Amide bond formation and peptide coupling. *Tetrahedron* vol. 61 10827–10852 (2005).
202. Cürten, B., Kullmann, P. H. M., Bier, M. E., Kandler, K. & Schmidt, B. F. Synthesis, Photophysical, Photochemical and Biological Properties of Caged GABA, 4-[[[(2H-1-Benzopyran-2-one-7-amino-4-methoxy) carbonyl] amino] Butanoic Acid. *Photochemistry and Photobiology* **81**, 641–648 (2007).
203. Kometani Tadashi, Shiotani Shunsaku & Mitsushashi Kemmotsu. On the cleavage of tertiary amines with ethyl chloroformate. *Chem. Pharm. Bull* **24**, 342–349 (1976).
204. Keisuke Kurita, Matsumura Toru & Iwakura Yoshio. Trichloromethyl Chloroformate. Reaction with Amines, Amino Acids and Amino Alcohols. *J. Org. Chem* **41**, 2070–2071 (1976).
205. Müller, R., Citir, M., Hauke, S. & Schultz, C. Synthesis and Cellular Labeling of Caged Phosphatidylinositol Derivatives. *Chemistry - A European Journal* **26**, 384–389 (2020).
206. Scott, R. H., Pollock, J., Ayar, A., Thatcher, N. M. & Zehavi, U. Synthesis and use of caged sphingolipids. *Methods in Enzymology* **312**, 387–400 (2000).
207. Saunders J.H, Clocombe R.J & Hardy E. Edgar. The Vapor Phase Reaction between Phosgene and Alcohols. *J. Phys. Chem* **73**, 3796–3798 (1950).
208. Dixon, S. L. & Jurs, P. C. Estimation of pKa for Organic Oxyacids Using Calculated Atomic Charges. *Journal of Computational Chemistry* **14**, 1460–1467 (1993).
209. Lu, Y. *et al.* Highly Selective Semihydrogenation of Alkynes to Alkenes by Using an Unsupported Nanoporous Palladium Catalyst: No Leaching of Palladium into the Reaction Mixture. *ACS Catalysis* **7**, 8296–8303 (2017).
210. Li, B. & Ge, H. *Highly selective electrochemical hydrogenation of alkynes: Rapid construction of mechanochromic materials.* *Sci. Adv* vol. 5 <https://www.science.org> (2019).
211. Mosquera, J., García, I. & Liz-Marzán, L. M. Cellular Uptake of Nanoparticles versus Small Molecules: A Matter of Size. *Accounts of Chemical Research* **51**, 2305–2313 (2018).
212. Kell, D. B. & Oliver, S. G. How drugs get into cells: tested and testable predictions to help discriminate between transporter-mediated uptake and lipoidal bilayer diffusion. *Frontiers in Pharmacology* **5**, (2014).

213. Wender, P. A. *et al.* The design, synthesis, and evaluation of molecules that enable or enhance cellular uptake: Peptoid molecular transporters. [www.pnas.org](http://www.pnas.org).
214. Xia, Y. & Peng, L. Photoactivatable lipid probes for studying biomembranes by photoaffinity labeling. *Chemical Reviews* **113**, 7880–7929 (2013).
215. Solanko, K. A., Modzel, M., Solanko, L. M. & Wüstner, D. Fluorescent sterols and cholesteryl esters as probes for intracellular cholesterol transport. *Lipid Insights* **2015**, 95–114 (2015).
216. Tallman, K. A. *et al.* Probes for protein adduction in cholesterol biosynthesis disorders: Alkynyl lanosterol as a viable sterol precursor. *Redox Biology* **12**, 182–190 (2017).
217. Ikonen, E. & Blom, T. Lipoprotein-mediated delivery of BODIPY-labeled sterol and sphingolipid analogs reveals lipid transport mechanisms in mammalian cells. *Chemistry and Physics of Lipids* **194**, 29–36 (2016).
218. Bektas, M. *et al.* Sphingosine 1-phosphate lyase deficiency disrupts lipid homeostasis in liver. *Journal of Biological Chemistry* **285**, 10880–10889 (2010).
219. Spohner, A. K. *et al.* Mouse liver compensates loss of sgpl1 by secretion of sphingolipids into blood and bile. *International Journal of Molecular Sciences* **22**, (2021).
220. Vienken, H. *et al.* Characterization of cholesterol homeostasis in sphingosine-1-phosphate lyase-deficient fibroblasts reveals a Niemann-Pick disease type C-like phenotype with enhanced lysosomal Ca<sup>2+</sup> storage. *Scientific Reports* **7**, (2017).
221. Li Guan, X. *et al.* Functional Interactions between Sphingolipids and Sterols in Biological Membranes Regulating Cell Physiology. *Molecular Biology of the Cell* **20**, 2083–2095 (2009).
222. Maxfield, F. R. & Wüstner, D. Intracellular cholesterol transport. *Journal of Clinical Investigation* **110**, 891–898 (2002).
223. Reddy, A., Caler, E. v. & Andrews, N. W. Plasma membrane repair is mediated by Ca<sup>2+</sup>-regulated exocytosis of lysosomes. *Cell* **106**, 157–169 (2001).
224. Sbano, L. *et al.* TFEB-mediated increase in peripheral lysosomes regulates store-operated calcium entry. *Scientific Reports* **7**, (2017).
225. Jaiswal, J. K., Andrews, N. W. & Simon, S. M. Membrane proximal lysosomes are the major vesicles responsible for calcium-dependent exocytosis in nonsecretory cells. *Journal of Cell Biology* **159**, 625–635 (2002).
226. Blom, T., Li, Z., Bittman, R., Somerharju, P. & Ikonen, E. Tracking Sphingosine Metabolism and Transport in Sphingolipidoses: NPC1 Deficiency as a Test Case. *Traffic* **13**, 1234–1243 (2012).
227. Shen, H. *et al.* Coupling between endocytosis and sphingosine kinase 1 recruitment. *Nature Cell Biology* **16**, 652–662 (2014).
228. Lima, S., Milstien, S. & Spiegel, S. Sphingosine and sphingosine kinase 1 involvement in endocytic membrane trafficking. *Journal of Biological Chemistry* **292**, 3074–3088 (2017).
229. Platt, F. M., Neises, G. R., Dwek, R. A. & Butters, T. D. N-butyldeoxynojirimycin is a novel inhibitor of glycolipid biosynthesis. *Journal of Biological Chemistry* **269**, 8362–8365 (1994).
230. Can Ficiocioglu. Review of miglustat for clinical management in Gaucher disease type 1. *Therapeutics and Clinical Risk Management* **4**, 425–431 (2008).
231. Pastores, G. M., Barnett, N. L. & Kolodny, E. H. An Open-Label, Noncomparative Study of Miglustat in Type I Gaucher Disease: Efficacy and Tolerability Over 24 Months of Treatment. *Clinical Therapeutics* **27**, 1215–1227 (2005).

232. Hollak, C. E. M., Hughes, D., van Schaik, I. N., Schwierin, B. & Bembi, B. Miglustat (Zavesca®) in type 1 Gaucher disease: 5-Year results of a post-authorisation safety surveillance programme. *Pharmacoepidemiology and Drug Safety* **18**, 770–777 (2009).
233. Neßlauer, A. M. *et al.* A therapy with miglustat, 2-hydroxypropyl- $\beta$ -cyclodextrin and allopregnanolone restores splenic cholesterol homeostasis in Niemann-pick disease type C1. *Lipids in Health and Disease* **18**, (2019).
234. Chang, T. Y. *et al.* Niemann-Pick type C disease and intracellular cholesterol trafficking. *Journal of Biological Chemistry* vol. 280 20917–20920 (2005).
235. Rocha, N. *et al.* Cholesterol sensor ORP1L contacts the ER protein VAP to control Rab7-RILP-p150Glued and late endosome positioning. *Journal of Cell Biology* **185**, 1209–1225 (2009).
236. Dong, J. *et al.* Allosteric enhancement of ORP1-mediated cholesterol transport by PI(4,5)P<sub>2</sub>/PI(3,4)P<sub>2</sub>. *Nature Communications* **10**, (2019).
237. Cianciola, N. L., Greene, D. J., Morton, R. E. & Carlin, C. R. Adenovirus RIDa uncovers a novel pathway requiring ORP1L for lipid droplet formation independent of NPC1. *Molecular Biology of the Cell* **24**, 3209–3225 (2013).
238. Dai, S. *et al.* Methyl- $\beta$ -cyclodextrin restores impaired autophagy flux in Niemann-Pick C1-deficient cells through activation of AMPK. *Autophagy* **13**, 1435–1451 (2017).
239. Newton, J. *et al.* Targeting defective sphingosine kinase 1 in Niemann–Pick type C disease with an activator mitigates cholesterol accumulation. *Journal of Biological Chemistry* **295**, 9121–9134 (2020).
240. Ilnytska, O. *et al.* Enrichment of NPC1-deficient cells with the lipid LBPA stimulates autophagy, improves lysosomal function, and reduces cholesterol storage. *Journal of Biological Chemistry* **297**, (2021).
241. Mccauliff, L. A. *et al.* Intracellular cholesterol trafficking is dependent upon NPC2 interaction with lysobisphosphatidic acid. *eLife* 1–31 (2019) doi:10.7554/eLife.50832.001.
242. Chaudhry, N. *et al.* Lamp1 mediates lipid transport, but is dispensable for autophagy in Drosophila. *BioRxiv* (2021) doi:10.1101/2021.03.03.432938.
243. Eskelinen, E.-L. *et al.* Disturbed Cholesterol Traffic but Normal Proteolytic Function in LAMP-1/LAMP-2 Double-deficient Fibroblasts □ D. *Molecular Biology of the Cell* **15**, 3132–3145 (2004).
244. Stein, V. M. *et al.* Miglustat improves purkinje cell survival and alters microglial phenotype in feline niemann-pick disease type C. *Journal of Neuropathology and Experimental Neurology* **71**, 434–448 (2012).
245. Platt, F. M. *et al.* Disorders of cholesterol metabolism and their unanticipated convergent mechanisms of disease. *Annual Review of Genomics and Human Genetics* **15**, 173–194 (2014).
246. Lachmann, R. H. *et al.* Treatment with miglustat reverses the lipid-trafficking defect in Niemann-Pick disease type C. *Neurobiology of Disease* **16**, 654–658 (2004).
247. Werner, T. *et al.* Ion coalescence of neutron encoded TMT 10-plex reporter ions. *Analytical Chemistry* **86**, 3594–3601 (2014).
248. Liu, Y. *et al.* The SCARB1 gene is associated with lipid response to dietary and pharmacological interventions. *Journal of Human Genetics* **53**, 709–717 (2008).
249. Linton, M. F., Tao, H., Linton, E. F. & Yancey, P. G. SR-BI: A Multifunctional Receptor in Cholesterol Homeostasis and Atherosclerosis. *Trends in Endocrinology and Metabolism* vol. 28 461–472 (2017).

250. Jian, B. *et al.* Scavenger Receptor Class B Type I as a Mediator of Cellular Cholesterol Efflux to Lipoproteins and Phospholipid Acceptors. *The Journal of Biological Chemistry* **273**, 5599–5606 (1998).
251. Kobayashi, N. *et al.* MFSD2B is a sphingosine 1-phosphate transporter in erythroid cells. *Scientific Reports* **8**, (2018).
252. Spiegel, S. & Milstien, S. The outs and the ins of sphingosine-1-phosphate in immunity. *Nature Reviews Immunology* vol. 11 403–415 (2011).
253. Sato, K. *et al.* Critical role of ABCA1 transporter in sphingosine 1-phosphate release from astrocytes. *Journal of Neurochemistry* **0**, 071106212736004-??? (2007).
254. Tanfin, Z., Serrano-Sanchez, M. & Leiber, D. ATP-binding cassette ABCC1 is involved in the release of sphingosine 1-phosphate from rat uterine leiomyoma ELT3 cells and late pregnant rat myometrium. *Cellular Signalling* **23**, 1997–2004 (2011).
255. Conrad, K. S. *et al.* Lysosomal integral membrane protein-2 as a phospholipid receptor revealed by biophysical and cellular studies. *Nature Communications* **8**, (2017).
256. Kwon, H. J. *et al.* Structure of N-Terminal Domain of NPC1 Reveals Distinct Subdomains for Binding and Transfer of Cholesterol. *Cell* **137**, 1213–1224 (2009).
257. Lloyd-Evans, E. *et al.* Niemann-Pick disease type C1 is a sphingosine storage disease that causes deregulation of lysosomal calcium. *Nature Medicine* **14**, 1247–1255 (2008).
258. Vanier, M. T. Complex lipid trafficking in Niemann-Pick disease type C. *Journal of Inherited Metabolic Disease* **38**, 187–199 (2014).
259. Zervas, M., Somers, K. L., Thrall, M. A. & Walkley, S. U. Critical role for glycosphingolipids in Niemann-Pick disease type C. *Current Biology* **11**, 1283–1287 (2001).
260. Bourdenx, M. *et al.* Nanoparticles restore lysosomal acidification defects: Implications for Parkinson and other lysosomal-related diseases. *Autophagy* **12**, 472–483 (2016).
261. Folts, C. J., Scott-Hewitt, N., Pröschel, C., Mayer-Pröschel, M. & Noble, M. Lysosomal Re-acidification Prevents Lysosphingolipid-Induced Lysosomal Impairment and Cellular Toxicity. *PLoS Biology* **14**, (2016).
262. Hannun, Y. A., Loomis, C. R., Merrill, A. H. & Bell, R. M. Sphingosine inhibition of protein kinase C activity and of phorbol dibutyrate binding in vitro and in human platelets. *Journal of Biological Chemistry* **261**, 12604–12609 (1986).
263. Vanharanta, L. *et al.* High-content imaging and structure-based predictions reveal functional differences between Niemann-Pick C1 variants. *Traffic* **21**, 386–397 (2020).
264. Thiele, C., Wunderling, K. & Leyendecker, P. Multiplexed lipid metabolic tracing using click chemistry mass spectrometric reporter molecules. (2019) doi:10.21203/rs.2.12570/v1.
265. Stein, F., Kress, M., Reither, S., Piljić, A. & Schultz, C. FluoQ: A tool for rapid analysis of multiparameter fluorescence imaging data applied to oscillatory events. *ACS Chemical Biology* **8**, 1862–1868 (2013).
266. Wickham, H. *ggplot2 - Elegant graphics for data analysis*. *ggplot2* (Springer New York, 2009). doi:10.1007/978-0-387-98141-3.

# Appendix

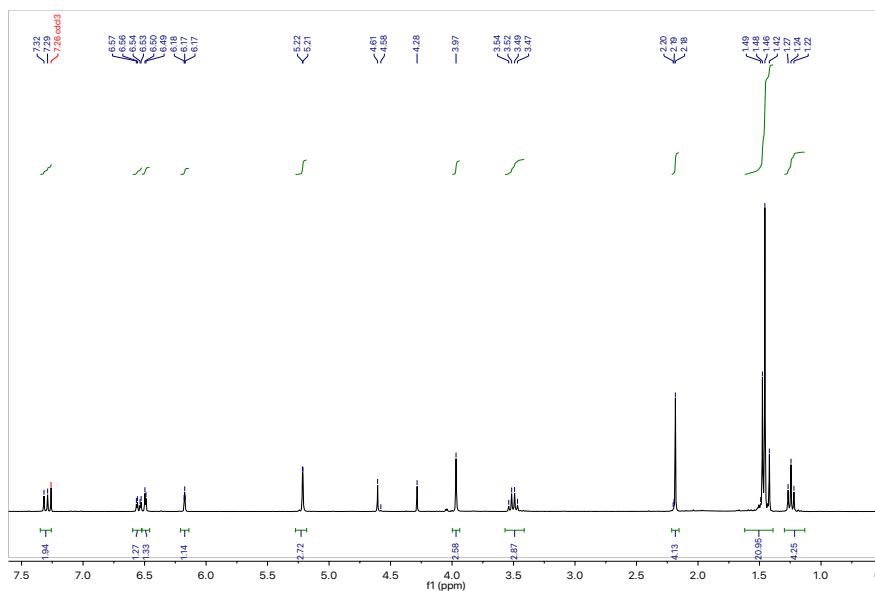
---

Raw files, R scripts and data used for quantification can be found at Mendeley data:

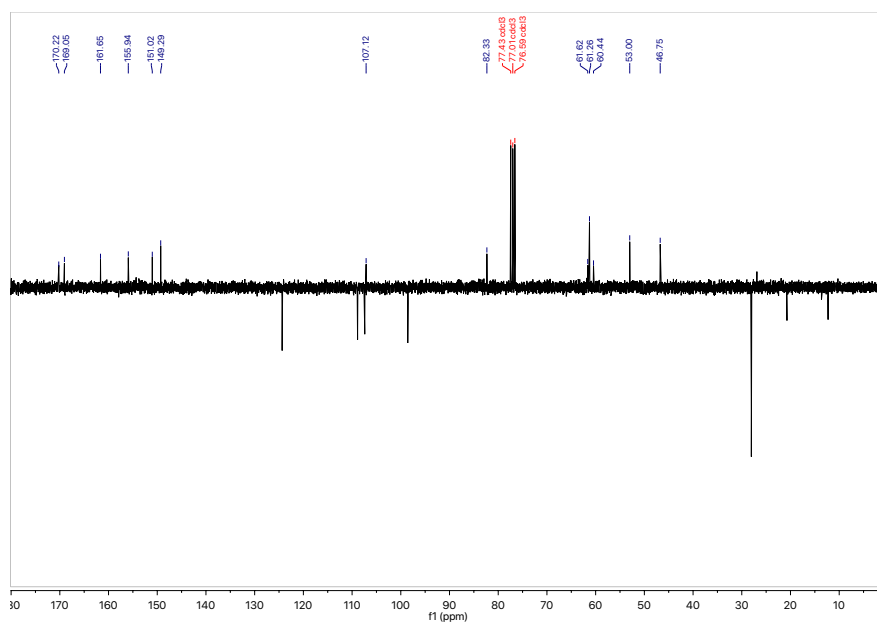
Juarez, Janathan (2022), "Supplementary data for dissertation "Development, characterization and application of lysosome-targeted multi-functional sphingosine and cholesterol probes"", Mendeley Data, V1, doi: 10.17632/7ghs9tp22k.1

## Proton and Carbon NMRs for synthesized compounds

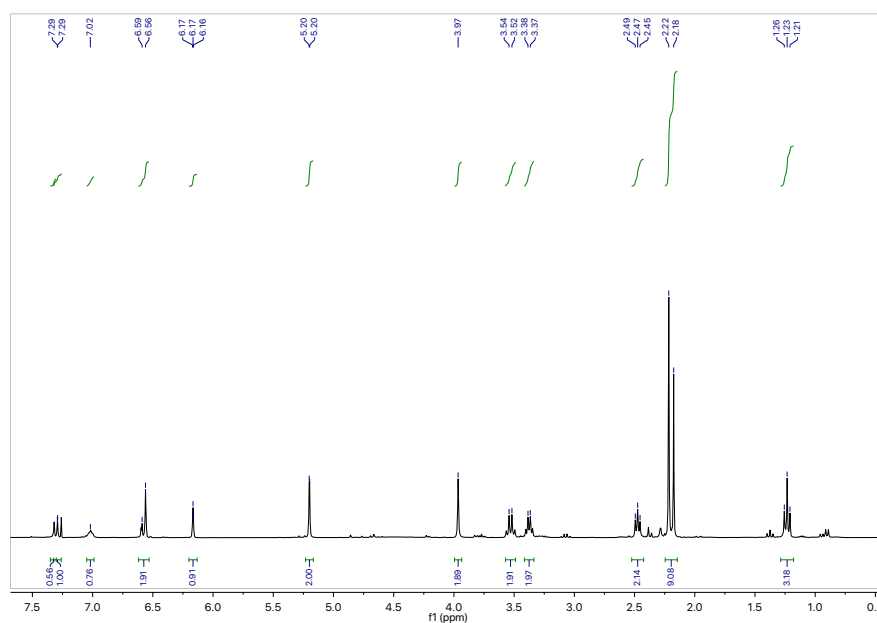
$H^1$  NMR spectra of ***Tert*-butyl-*N*-(4-(acetoxymethyl)-2-oxo-2H-chromen-7-yl)-*N*-ethylglycinate**



$^{13}\text{C}$  NMR spectra of ***Tert*-butyl-*N*-(4-(acetoxymethyl)-2-oxo-2H-chromen-7-yl)-*N*-ethylglycinate**



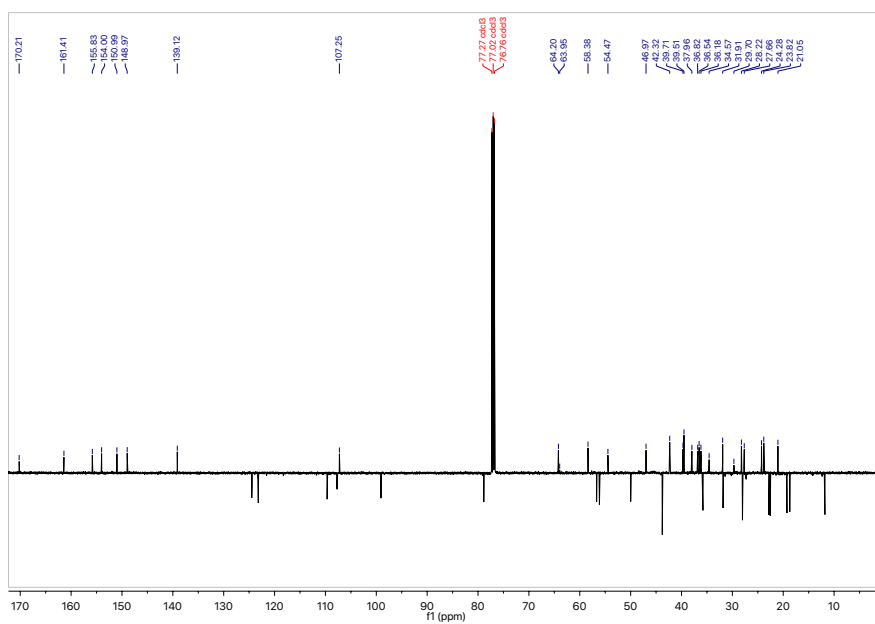
$^1\text{H}$  NMR spectra of **2-(dimethylamino)ethyl *N*-(4-(acetoxymethyl)-2-oxo-2H-chromen-7-yl)-*N*-ethylglycinate**



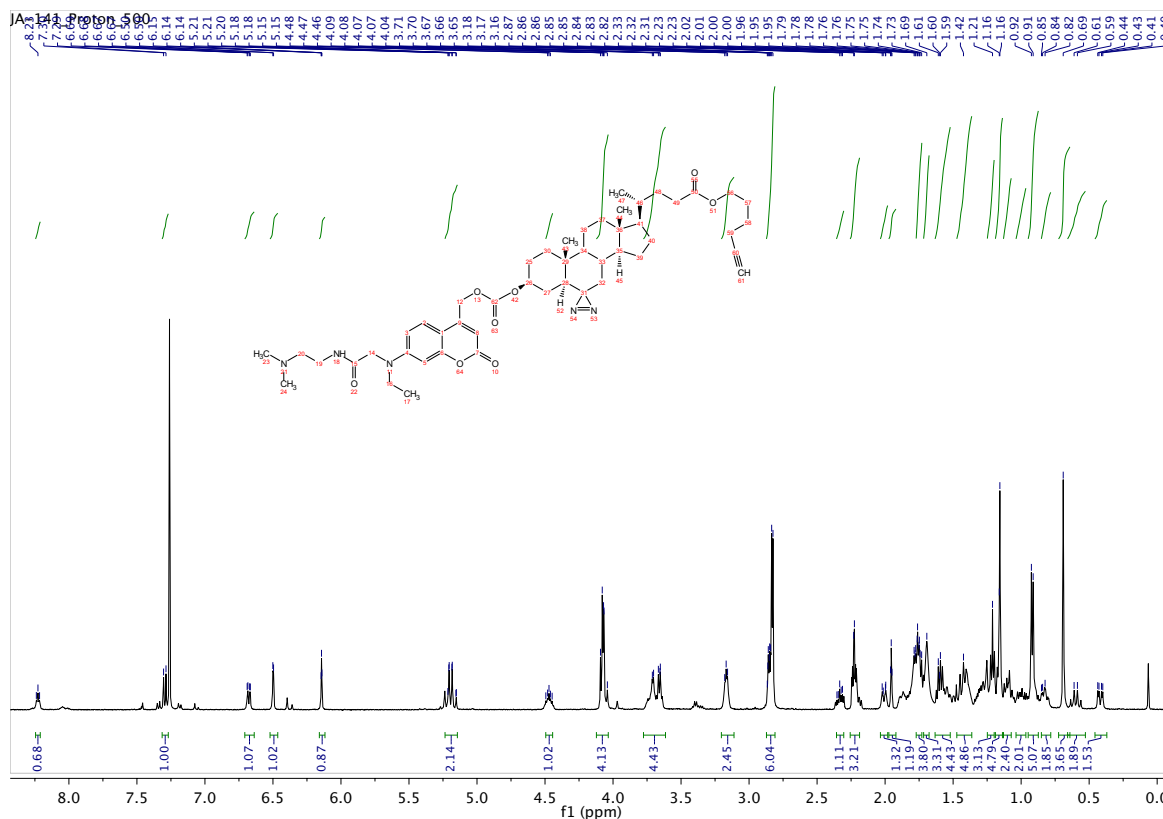




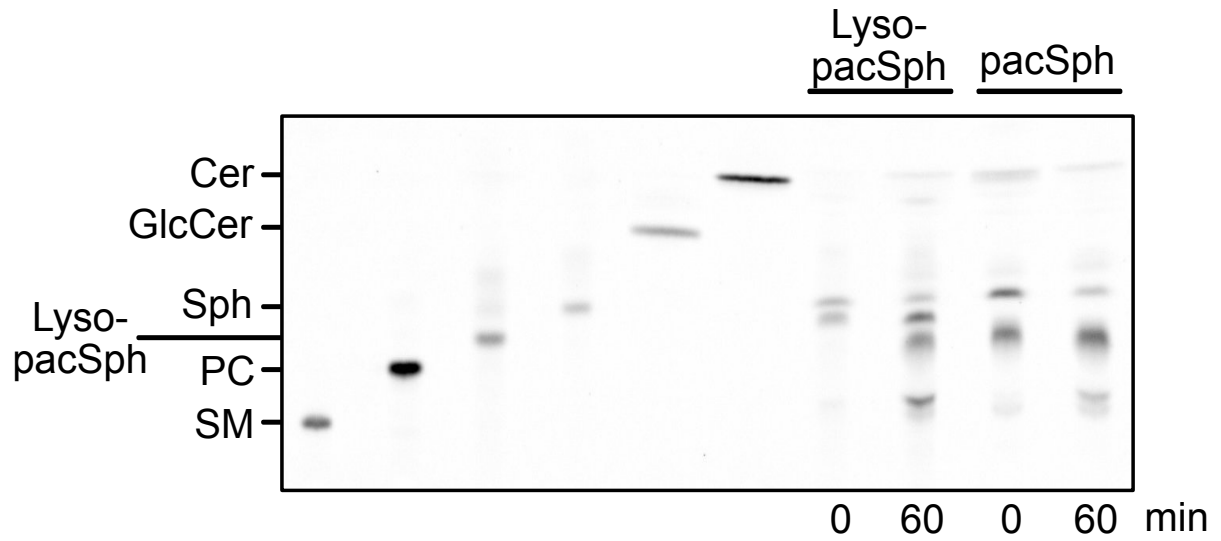
# <sup>13</sup>C NMR spectra of Lyso-Cholesterol



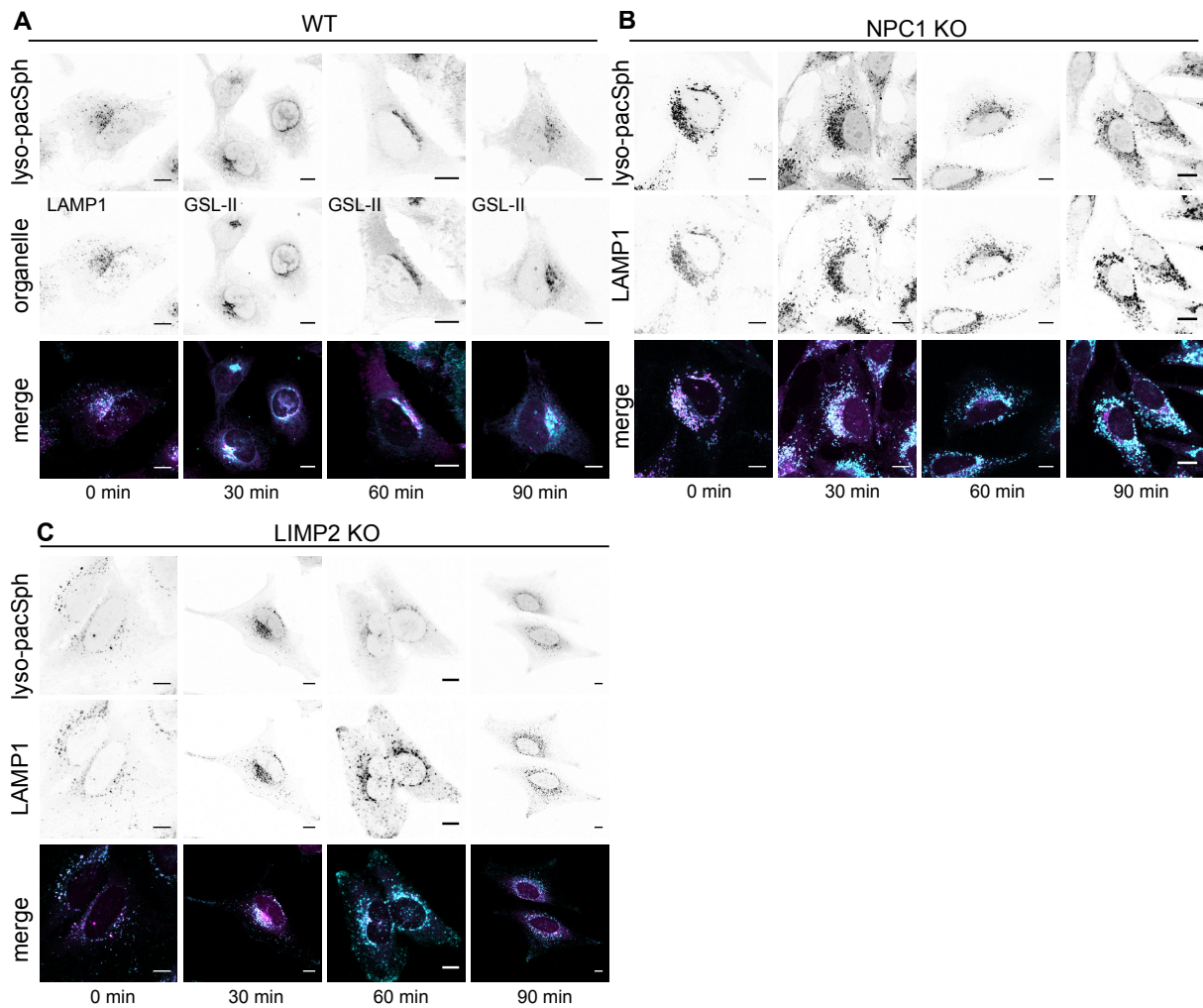
# H<sup>1</sup> NMR spectra of Lyso-pacCholesterol



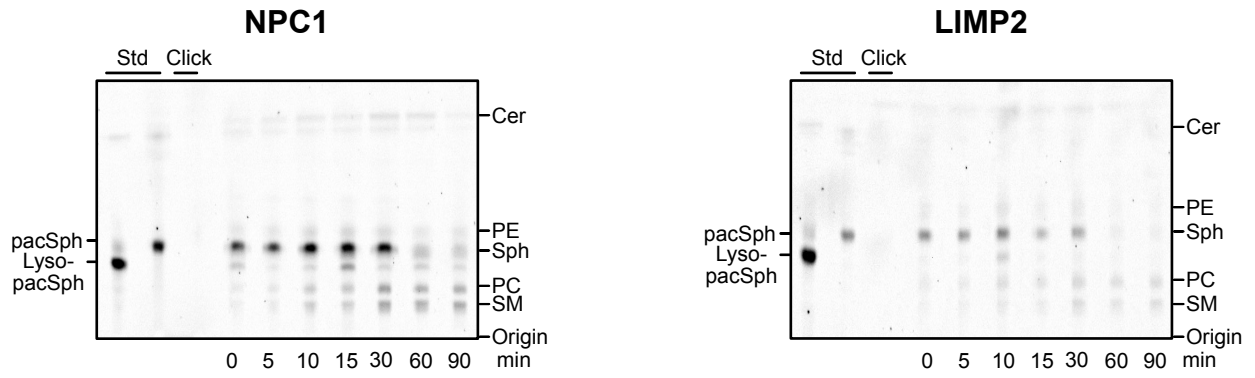
## Lipid identification by TLC



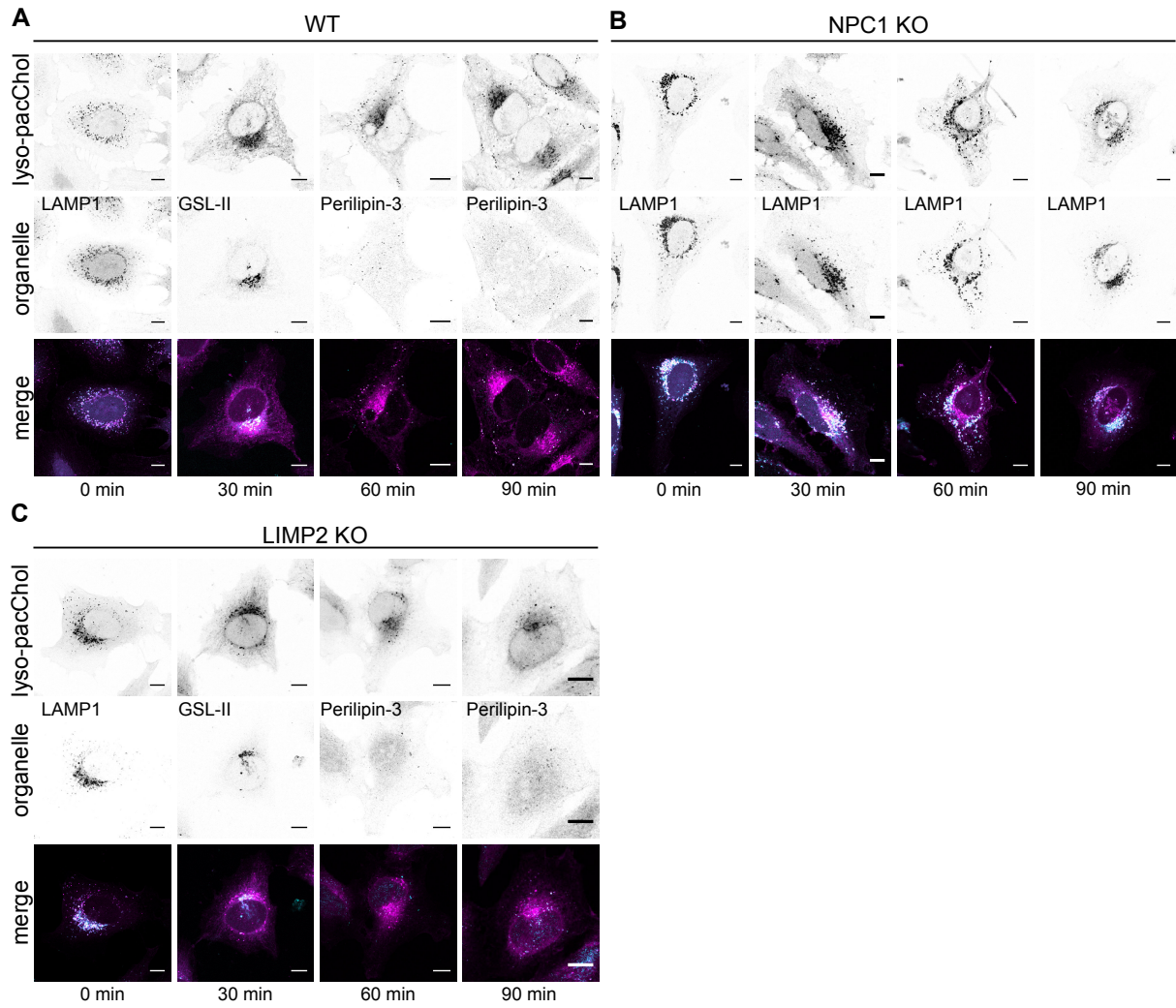
## Confocal microscopy images of organelle identification of Lyso-pacSph



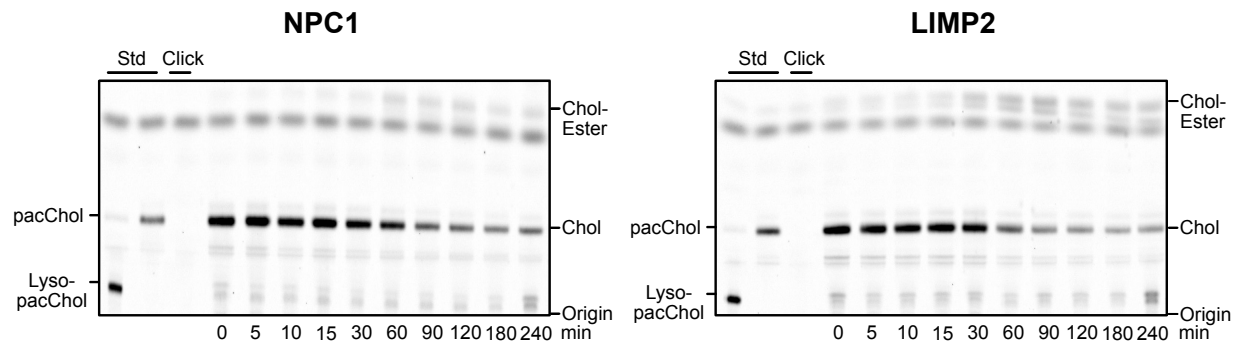
## TLC of Lyso-pacSph in NPC1 and LIMP2 $\text{-/-}$ cells



## Confocal microscopy images of organelle identification of Lyso-pacChol



## TLC of Lyso-pacChol in NPC1 and LIMP2 <sup>-/-</sup> cells



# List of abbreviations

---

Abbreviation	Full name
aCDase	Acid ceramidase
ACN	Acetonitrile
AcOH	Acetic acid
AM	Acetoxymethyl
ATP	Adenosine triphosphate
Bis-4-NPC	Bis-(4-nitrophenyl) carbonate
BODIPY	Boron-dipyrromethene
BSA	Bovine serum albumin
BTTA	2-(4-((Bis((1-( <i>tert</i> -butyl)-1 <i>H</i> -1,2,3-triazol-4-yl)methyl)amino)methyl)-1 <i>H</i> -1,2,3-triazol-1-yl)acetic acid
C1P	Ceramide-1-phosphate
CDase	Ceramidase
CE	Cholesterol ester
Cer	Ceramide
CerK	Ceramide kinase
CerS	Ceramide synthase
CERT	Ceramide transfer protein
CuACC	Cu(I) catalysed alkyne/azide cycloaddition
Cy	Cyclohexane
DAG	Diacylglycerol
DCM	Dichloromethane
DEAC	Dimethylaminocoumarin
dhCer	Dihydroceramide
dhSph	Dihydrosphingosine
DIPEA	Diisopropylethyleneamine
dKO	Double knockout
DMEM	Dulbecco's Modified Eagle Medium

DMF	Dimethylformamide
DMSO	Dimethylsulfoxide
DNA	Desoxyribonucleic acid
DTT	Dithiothreitol
EDTA	Ethylene diamine tetraacetic acid
EMBL	European Molecular Biology Laboratory
ER	Endoplasmic reticulum
ESI	Electrospray ionisation
EtOAc	Ethylacetate
EtOH	Ethanol
FA	Fatty acid
FDR	False discovery rate
GalCer	Galactosylceramide
GBA	Glucosylceramidase
GluCer	Glucosylceramide
HEPES	4-(2-hydroxyethyl)-1-piperazineethanesulfonic acid
HPLC	High performance liquid chromatography
ICBF	Isobutylchloroformate
LAMP-1	Lysosome associated membrane protein 1
LE	Late endosome
LIMP-2	Lysosome integral membrane protein 2
LY	Lysosome
Lyso-Cou	Lysosome-targeted coumarin cage
Lyso-Chol	Lysosome-targeted cholesterol
Lyso-pacChol	Lysosome-targeted pacChol
Lyso-pacSph	Lysosome-targeted pacSph
Lyso-So	Lysosome targeted sphingosine probe
Lyso-Sph	Lysosome-targeted sphingosine
MCS	Membrane contact site
MeOH	Methanol
Mito-So	Mitochondria targeted sphingosine probe
MS	Mass spectrometry

mTORC	Mechanistic target of rapamycin complex
nCDase	Neutral ceramidase
NBD	nitrobenoxadiazole
NMM	N-methylmorpholine
NMR	Nuclear magnetic resonance
NP40	Nonidet-P40
NPC	Niemann-Pick disease type C
NPC1	Niemann-Pick-Type C1 Intracellular cholesterol transporter
NPC2	Niemann-Pick-Type C2 Intracellular cholesterol transporter
pacChol	Photoactivatable and clickable cholesterol
pacFA	Photoactivatable and clickable fatty acid
pacSph	Photoactivatable and clickable sphingosine
PBS	Phosphate buffered saline
PBS-T	Phosphate-buffered saline with 0.1% Tween
PC	Phosphatidylcholine
PCC	Pearson's correlation coefficient
PCR	Polymerase chain reaction
PE	Phosphatidylethanolamine
PIC	Protease inhibitor cocktail
PKC	Protein Kinase C
PM	Plasma membrane
PMA	Phosphomolybdic acid
RNA	Ribonucleic acid
RNAi	RNA interference
ROI	Region of interest
RT	Room temperature
S1P	Sphingosine-1-phosphate
SGPL1	Sphingosine-1-phosphate lyase
SDS-PAGE	Sodium dodecyl sulfate polyacrylamide gel electrophoresis
siRNA	Small interfering ribonucleic acid
SK1	Sphingosine kinase 1
SK2	Sphingosine kinase 2

SM	Sphingomyelin
SMase	Sphingomyelinase
SMS	Sphingomyelin synthase
SOC	Super optimal broth with catabolite repression
Sph	Sphingosine
SPT	Serine palmitoyl transferase
SSD	Sterol sensing domain
TEA	Triethylamine
TFA	Trifluoroacetic acid
TFEB	Transcription factor EB
TFFA	Trifunctional fatty acid
TFS	Trifunctional sphingosine
THF	Tetrahydrofuran
TLC	Thin-layer chromatography
TMT	Tandem mass tag
TPC	Two-pore channels
TPP	Triphenylphosphine
UV	Ultraviolet
vATPase	Vacuolar H <sup>+</sup> -adenylypyrophosphatase
WT	Wild type

# Acknowledgements

---

First, I would like to thank my mentor Dr. Doris Höglinger for giving me the opportunity of pursuing a doctoral degree in her lab and trusting me with this project. I am also thankful for her patience, understanding, support and unconditionally guidance during this journey. Thank you very much Doris!

I would also like to thank all members of the Höglinger lab: Valle, Pia for all the nice discussions and help through these almost 5 years, to Judith a former lab member for help with the chemical synthesis and probe characterization. Additionally, I would also like to thank Jutta Worsch for always taking care of all of us, I will miss cookie time.

Additionally, I would like to thank members from the Nickel's lab: Roberto, Fabio, Jaime and specially to Annalena for being such a good friend in and outside the lab, I will miss a lot of stuff!

To the Mexican gang, some here, some abroad. Anayanssi, Jonathan, Benjamin (honorary mexican) Leslee, Gisela, Raul, Rodrigo and Martin. Even if we don't see each other that often all of you were of truly help in times of need and when we meet it is always such a fun time!

To Olmo and Cinthia, for being the persons who always get me. For being there always and making the last years of the PhD so fun, even if you make fun of me because I can't dance.

Y sobre todas las cosas, quiero agradecer a mis padres Jose Juarez y Tereza Altuzar por toda su paciencia y amor incondicional, por existir, por apoyarme y terapiarme en momentos buenos y malos. Por estar conmigo siempre en la distancia, no hay día que pase sin extrañarlos. Por eso, esta tesis va dedicada para ustedes.

- *alles hat ein ende nur die wurst hat zwei*